UNIVERSITÀ DEGLI STUDI DI PADOVA

DIPARTIMENTO DI INGEGNERIA INDUSTRIALE

CORSO DI LAUREA MAGISTRALE IN INGEGNERIA DEI MATERIALI

Tesi di Laurea Magistrale in Ingegneria dei Materiali

Gas flow-assisted powder deposition for 3D printing of α-TCP: printing and sintering evaluations

Relatore: Prof. Paolo Colombo
Correlatore: Prof. Jens Günster
M.Sc. Janka Wilbig

Laureando: FABIO CHINELLATO

ANNO ACCADEMICO 2017-2018

Sommario

In questa tesi, α-TCP è impiegato per stampare 3D *tablet* e *scaffold* per scopi biomedici. α-TCP è utilizzato in applicazioni ortopediche, dentistiche e maxillo-facciali grazie alla sua bioattività e alle sue caratteristiche osteoconduttive. Il concetto di base consiste nel produrre parti che corrispondono perfettamente a dimensioni e forma del difetto osseo nel paziente. Dopo il trapianto, lo *scaffold* si integra con il tessuto circostante e promuove la formazione dell'osso rilasciando ioni nutritivi e assicurando un'adeguata vascolarizzazione. Lo *scaffold* si degrada gradualmente con un tasso simile alla crescita dell'osso in modo tale da fornire un costante supporto per tutta la durata della guarigione. Tuttavia, il principale svantaggio dell'α-TCP risiede nelle scarse proprietà meccaniche. Per questo attualmente è solamente usato in forma di polvere.
Un promettente metodo per ottenere componenti ceramici porosi è il cosiddetto *binder jetting*, o più comunemente chiamato *stampa 3D*. Questa appartiene alla più ampia categoria denominata produzione additiva la quale al contrario di quella sottrattiva e formativa, consiste nel realizzare un oggetto strato dopo strato da modelli 3D computerizzati. In particolare, la stampa 3D si basa nello stampare della colla in modo selettivo sul letto di polvere incollando le particelle tra loro in maniera tale da formare la sezione dell'oggetto.

α-TCP è stato sintetizzato a partire da H_3PO_4 e $CaCO_3$ tramite reazione allo stato solido. I vari lotti prodotti risultano avere 93±2% di α-TCP e 7±2% di idrossiapatite. Dopo sinterizzazione l'unica fase presente è α-TCP. L'alta purezza della polvere è estremamente importante dal punto di vista biologico in quanto la presenza di impurezze o altre fasi può causare risposte infiammatorie o una diversa velocità di riassorbimento.

Tablet e *scaffold* sono stati stampati con due diverse granulometrie: *fine* (minore di 25 μm) e *grossa* (tra 45 e 100 μm). La polvere più grossa può essere facilmente e uniformemente depositata. La polvere fine invece permette di avere una maggiore risoluzione e densità dell'oggetto stampato. Tuttavia, questa risulta impossibile da depositare a causa della spiccata tendenza ad agglomerarsi. Per risolvere questo problema, si può stabilizzare il letto di polvere attraverso un flusso di gas. Ciò significa che una pompa da vuoto è connessa al fondo del letto di polvere così facendo la polvere è più compatta e persino la polvere fine può essere stampata. In conclusione, tre tipologie

vengono impiegate: polvere grossa stampata con e senza il flusso di gas e polvere fine stampata con gas.

Gli effetti del flusso di gas possono essere apprezzati dalla densità delle *tablet*: la porosità apparente è 15% per la polvere fine mentre per quella grossa il valore passa da 43 a 50% con e senza il flusso di gas. Un simile comportamento può essere notato negli *scaffold*: quelli stampati con polvere fine hanno una densità apparente di 765 kg/m^3 mentre quelli con polvere grossa di 617 e 540 kg/m^3. Inoltre, *scaffold* con polvere fine presentano una maggiore definizione delle celle e dei profili e la porosità finale è molto simile a quella nominale.

Le proprietà meccaniche delle *tablet* sono state misurate con il test *ball on three balls* (B3B): le *tablet* stampate con polvere grossa e senza il flusso di gas presentano il valore più alto (5.3 MPa) mentre quelle fine raggiungono solamente 2.1 MPa. Situazione intermedia invece per quelle grosse stampate con flusso di gas (3.3 MPa). Nel tentativo di migliorare questi risultati, altri programmi di sinterizzazione sono stati eseguiti per le *tablet* stampate con il flusso di gas e i valori massimi sono stati 3.4 e 3.1 MPa per le *tablet* grosse e fine. Per quanto riguarda la prova di compressione degli *scaffold*, quelli con polvere fine sono i più resistenti: 3.4 MPa. Per quelli stampati con polvere grossa con e senza flusso di gas i risultati sono stati 1.4 e 0.9 MPa.
Questo comportamento meccanico può essere spiegato dall'analisi delle micrografie: *tablet* e *scaffold* più densi presentano un maggior numero di cricche. La causa potrebbe risiedere nella trasformazione di fase tra α-TCP e α'-TCP. Nel test B3B, la componente tensionale favorisce lo sviluppo di cricche causando una veloce frattura, mentre negli *scaffold* il parametro determinante è la densità poichè parte delle cricche vengono chiuse dalla componente compressiva.

In conclusione, la stabilizzazione del letto di polvere tramite un flusso di gas ha effetti significativi sulla densità degli oggetti stampati e, in particolare, permette la stampa di particelle minori di 25 μm. α-TCP può avere impieghi promettenti nella riparazione di difetti ossei, ma la causa delle cricche deve essere ulteriormente studiata, in modo tale da poter migliorare le proprietà meccaniche.

Questo lavoro di tesi è stato interamente sviluppato presso l'istituto federale di ricerca e test di materiali (BAM) di Berlino nella divisione 5.4 che ringrazio immensamente.

Abstract

In this thesis, tricalcium phosphate (α-TCP) has been used to 3D print tablets and scaffolds for biomedical applications. α-TCP has promising applications in orthopedics, dentistry and maxillofacial surgery thanks to its bioactivity and osteoconductive properties. The main goal is to produce parts that can perfectly match the bone defect of the patient. After implantation, the scaffold is integrated in the host tissue and it promotes the formation of the new bone by releasing nutrient ions and ensuring the vascularization. Gradually, the scaffold degrades with a rate as close as possible to the bone formation in order to provide a constant support throughout the healing. However, the principal drawback of α-TCP is its poor mechanical strength. Indeed, α-TCP is currently employed only in powdery form.
A suitable method to achieve porous ceramic components is binder jetting (commonly, 3D printing) that belongs to the wide category of *additive manufacturing techniques* (AM). Unlike the subtractive and formative manufacturing technologies, in AM the object is made from 3D model data, layer upon layer. In 3D printing, a liquid bonding agent is selectively deposited to join powder material from a print-head.

α-TCP has been synthesised from H_3PO_4 and $CaCO_3$ by solid state reaction. The batches produced contain 93±2% of α-TCP and 7±2% of HA but after sintering, only α-tricalcium phosphate was detected. High purity is extremely important from a biological point of view since other compounds may cause an inflammatory response or have a slower degradation rate.

Tablets and scaffolds have been 3D printed with two particle sizes: *fine* (lower than 25 μm) and *coarse* (between 45 and 100 μm). Big particles are more flowable therefore a uniform deposition is easily achievable. On the other hand, fine powder allows to obtain higher accuracy and denser parts. However, the fine powder cannot be deposited homogeneously due to the high interparticles force that causes the formation of agglomerations. A solution to this problem is to stabilize the powder bed through a gas flow. A vacuum pump is used to suck air from the bottom of the bed so that the powder is more compact and even the particles lower than 25 μm can be printed. In conclusion, three typologies are printed: coarse powder with and without the use of gas flow and fine powder with gas flow.

The effects of the gas flow can be appreciated from the density of the tablets: the apparent porosity reaches 15% for the fine tablets whereas 43 and 50% for the coarse ones printed with and without gas flow respectively. A similar trend can be noted in the scaffolds where the fine ones have a bulk density of 765 kg/m^3 while the coarse scaffolds printed with and without gas flow reach 617 kg/m^3 and 540 kg/m^3. Moreover, the fine scaffolds show a higher definition of the struts, cells and sides and the final porosity better matches the nominal one.

The mechanical strength of the tablets has been evaluated with the ball on three balls test (B3B): the coarse tablets printed without gas flow have the highest value (5.3 MPa) while the fine ones reach only 2.1 MPa. The coarse tablets printed with gas show an intermediate situation (3.3 MPa). To improve these results, other sintering programs have been tried for the tablets printed with gas flow and the maximum strength achieved has been 3.4 MPa and 3.1 MPa for the coarse and fine tablets. On the other hand, compressive tests have been carried out on the scaffolds and the fine ones have the greatest value (3.4 MPa). The strength of the coarse scaffolds is 1.4 and 0.9 MPa for those printed with and without gas flow respectively.

The reason of the mechanical behaviour can be understood from the micrographs: the denser the part, the higher the quantity of cracks. Their origin may be the phase transformation between α-TCP and α'-TCP. In the B3B test, the tensile component promotes the elongation of the cracks causing an easy fracture whereas in the scaffold, the main critical parameter is the density of the part since the compressive force closes part of the cracks.

In conclusion, the stabilization of the powder bed through a gas-flow has significant effects on the density of the printed parts and in particular, even particles lower than 25 μm can be successfully printed. α-TCP is a promising material to repair bone defects but the reason of the cracks formation must be further studied in order to increase the mechanical properties.

This work has been entirely developed at the federal institute for materials research and testing (BAM) in Berlin in the division 5.4 that I thank sincerely.

Contents

Glossary

3DP 3D printing.

A-W Apatite-wollastonite.

AM Additive manufacturing.

B3B Ball on three balls test.

CaP Calcium phosphate.

CM Conventional manufacturing.

DCP Dicalcium phosphate or brushite, $CaHPO_4{\cdot}2\,H_2O$.

EBM Electron beam melting.

FDM Fused deposition modelling.

HA Hydroxyapatite, $Ca_{10}(PO_4)_6(OH)_2$.

OCP Octacalcium phosphate, $Ca_8H_2(PO_4)_6{\cdot}\,5\,H_2O$.

RP Rapid prototyping.

SLA Stereolitography.

SLM Selective laser melting.

SLS Selective laser sintering.

TCP Tricalcium phosphate, $Ca_3(PO_4)_2$.

TTCP Tetracalcium phosphate, $Ca_4(PO_4)_2O$.

Chapter 1

Additive Manufacturing

In this chapter, an overview of the main features of additive manufacturing (hereinafter AM) will be presented. After a brief introduction (section 1.1), section 1.2 deals with the most important typologies of AM and section 1.3 covers the principal properties of AM with advantages and drawbacks. Afterwards, section 1.4 focuses on the biomedical field and to conclude, some considerations about the market and the future trends are discussed in section 1.5 and 1.6 respectively.

1.1 Introduction

AM has constantly gained popularity from its origin in the early 1980s when Charles Hull pioneered the first model of AM describing a vat polymerization method known as stereolithography [1]. Since then, thanks to its promising and unique features, AM has been considered as *the third industrial revolution* [2]. Indeed, after the first revolution in Britain in the late 18th century and the second one in America in the early 20th century, in some fields AM has entirely changed the way of designing, building and assembling parts. Not only has it modified the processing steps but also it had and is still having great influences on the supply chain, logistic, environmental and regulatory issues. Furthermore, AM has been compared to such *disruptive technologies* as digital books and music downloads where the customer can order and buy the product online. Therefore, the companies can serve small and niche market segments and work with very little or no unsold goods inventory.

The meaning of the term AM refers to the technique where the material is manipulated so that successive pieces of it combine to create the desire object. More specifically, the ISO/ASTM 17296 standard defines AM as *'the process of joining materials to make objects from three-dimensional (3D) model data, usually layer by layer as opposed to subtractive and formative manufacturing methodologies'* [3].

Originally, this manufacturing industry was used to produce functional prototypes and

visualization models and thus it has been named *rapid prototyping*, RP. In contrast to the name additive manufacturing, RP creates parts from 3-D data layer-by-layer but the final part is still fabricated by conventional manufacturing techniques (CM). RP reduces cost and time (from days to hours [2]) to test and evaluate the future product. On the other hand, AM exploits the same process concept but the end-use part is built directly using layer-by-layer methods.

Generally, the main steps to build an object are the generation of a 3D CAD file that is converted to STL file (STereo-Lithography format) to be printed. For instance, the CAD file can be derived from medical images such as computed tomography scans (CT), magnetic resonance imaging (MRI) or capture geometry internally (CGI). Once the CAD file is ready, virtual tests can be run in order to evaluate the efficiency of the object in order to print only when all the features fit the requirements. This procedure avoids redesigning the part after being produced as it happens during the conventional manufacturing methods (saving time and money). The pre-printing process takes into account many parameters such as the slicing and the orientation of the part, the building direction, the needs for supports, the layer thickness and the presence of hollow structures.

The common procedure for 3D powder based printing is based on the spreading of a layer of material (mainly powder or polymer) through a roller or a blade. The print head selectively jets material/binder or fuses the material forming the first cross-section of the 3D file. Afterwards, the building platform is lowered and new material is spread and selectively glued/deposited/fused. These steps occur until the whole part is printed and then is removed and cleaned. After printing, a curing process or post-processes might be necessary depending on the material and the application.

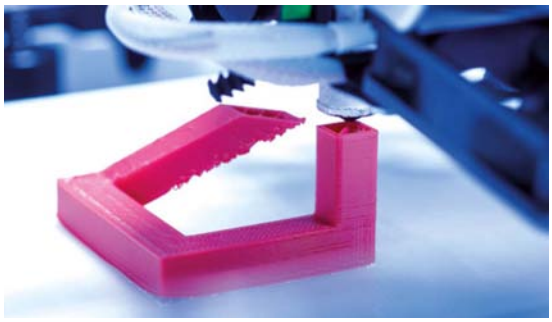

(a) Layer-by-layer AM process.

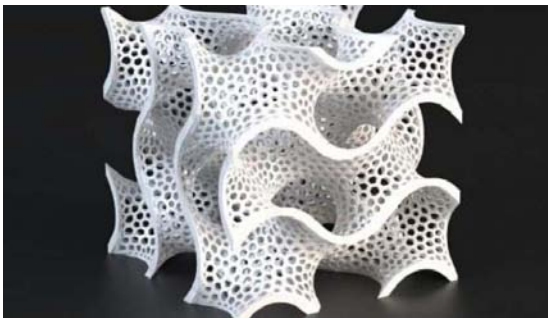

(b) Complex and lightweight objects are feasible with AM.

Figure 1.1: AM is a promising technology based on the production of parts layer upon layer in order to achieve properties almost unachievable through traditional methods.

www.ey.com/Publication/vwLUAssets/ey-global-3d-printing-report-2016-full-report/FILE/ey-global-3d--printing-report-2016-full-report.pdf

statics3.seeedstudio.com/seeed/img/2017-06/U627KpemEthxG3ZuxKQOM21U.jpeg

1.2 AM classification

The ISO/ASTM 17296 standard establishes also two categories of AM process and seven types of techniques.
The two categories are [3]:

1. **the single-step process**: the shape of the object and the material properties are achieved simultaneously in a single operation;

2. **the multi-step process**: the shape of the part is produced in two or more stages and the consolidation occurs during secondary operations. Most of the ceramic parts are obtained by indirect process where a binder is used to glue the powder and then, removed by heat treatment (debinding) and lastly the object is sintered to obtain the final mechanical properties.

Seven types of AM [3, 4]:

1. **Material jetting**: droplets of build material are selectively deposited onto the build tray (see fig. 1.2). Another name used for material jetting is ink-jet and two types can be distinguished: continuous and drop-on-demand (DoD) depending on features of the droplets stream. For instance, in the latter the signal is sent to the nozzle only when the droplet is required reducing the waste of material used.

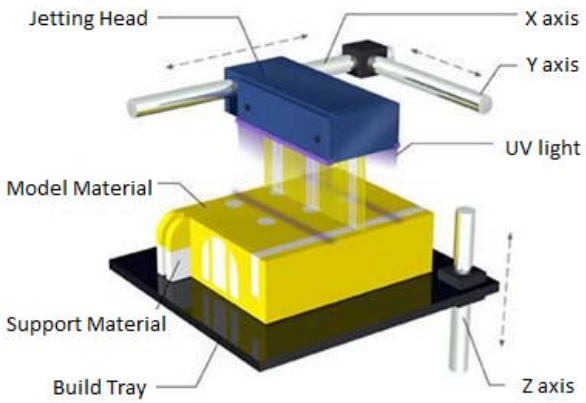

Figure 1.2: Material jetting.
seb199.me.vt.edu/dreams/material-jetting

2. **Material extrusion**: the material is selectively dispensed through a nozzle or orifice (see fig. 1.3). The extruded material exits the nozzle in a semi-solid state and remains in that shape until it is fully solidified. The solidification can be achieved by thermal processing or by chemical change using a curing agent. One of the first technique was the *fused deposition modelling* (FDM) commercialized by Stratasys in

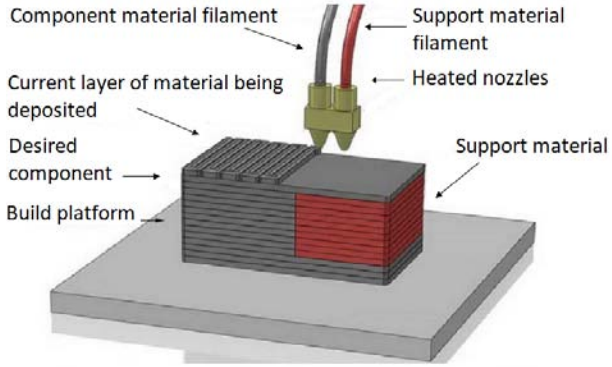

Figure 1.3: Material extrusion.
www.3dprintersonlinestore.com/important-things-to-know-about-dual-extrusion-in-3d-printers

1992 and theoretically any materials that flows when hot and solidifies when cooled can be used.

3. **Directed energy deposition**: focused thermal energy is used to fuse materials by melting as they are being deposited (see fig. 1.4). Also called *beam deposition technology*, the printing head consists of a nozzle that feeds powder particles to the focal point of the laser/electron beam. Thus, the powder melts and solidifies on a substrate.
   This method is particularly used for circular and elliptical shapes since the platform can rotate while the nozzle is fixed.

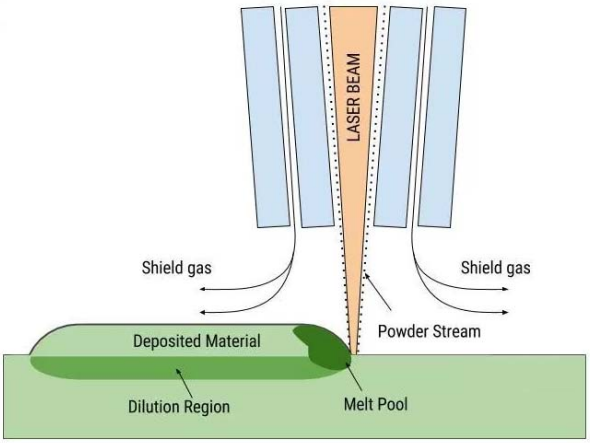

Figure 1.4: Directed energy deposition.
www.tripodmaker.com/2017/04/04/types-of-3d-printing

4. **Sheet lamination**: sheets of material are bonded to form an object by ultrasonic welding and then machined. Energy is transferred to the work piece through a roughened sonotrode that causes a localized heating of the interlaminar metal along with the application of a compressive force (see fig. 1.5). This results in a

metallurgical bonding without melting. Nowadays, this method is mainly used for carbon reinforced sheets.

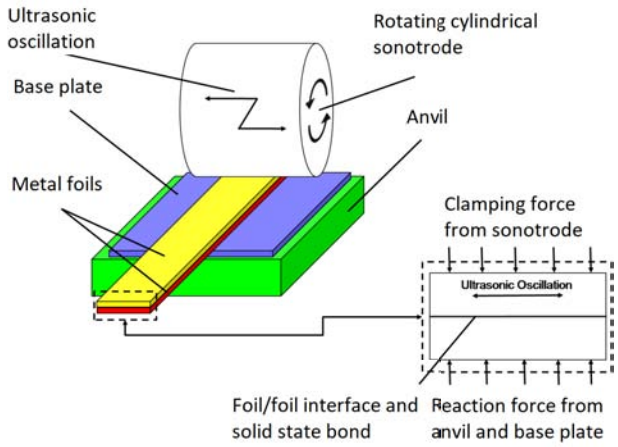

Figure 1.5: Sheet lamination.
3dprinting.com/what-is-3d-printing

5. **Binder jetting**: a liquid bonding agent is selectively deposited to join powder materials (see fig. 1.6). The principle consists of a nozzle that moves across the layer and sprays jets of glue to bind the powder at specific points. As each layer is finished, the piston moves down and another layer of powder is deposited, rolled and glued. The finished objects is embedded in unglued powder which is then blown away.

   Although 3D printing (3DP) has become a popular term for the general idea of AM, technically, it refers to the binder jetting method that opposed to material jetting, the binder is printed onto the base powder. Some of the most well-known companies are 3D Systems, Pro-Metal and Voxeljet. This technology will be discussed in detail in the following chapters.

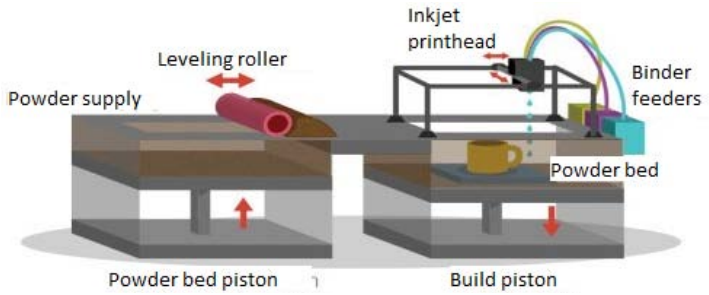

Figure 1.6: Binder jetting.
www.threeding.com/blog/%E2%80%8Bbinder-jetting-3d-printing-technology

6. **Powder bed fusion**: thermal energy selectively fuses areas of the powder bed containing the powder material (see fig. 1.7). Usually a laser source fuses material

and bonds to layers below. *Selective laser sintering* (SLS) is used for polymers such as nylon, polycarbonate, polystyrene, polypropylene and polycaprolactone. For metals, there are various methods such as *selective laser melting* (SLM) and *electron beam melting* (EBM) that differ in scan speed, atmosphere required, resolution and accuracy. Many technologies are available in the market: single or double-step, full or partial melting and solid state sintering.

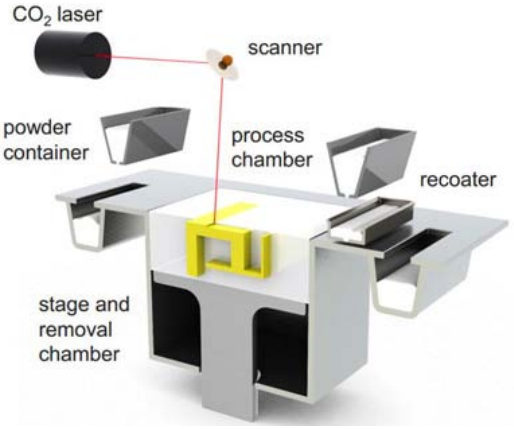

Figure 1.7: Powder bed fusion.
www.aniwaa.com/3d-printing-technologies-and-the-3d-printing-process

7. **Vat photopolymerization**: a liquid photopolymer in a vat is selectively cured by light-activated polymerization (see fig. 1.8). This method was the first RP system. Stereolithography (SLA) consists in solidifying the SL resin 'point by point' by the UV laser. The laser should penetrate the resin by the set layer thickness and avoid over or under exposure. With this technique parts with good surface finish and high accuracy can be achieved. However, some disadvantages may be linked to the trapped volumes, the cost of the large vat of resin and the brittleness of the printed parts compared to other methods.

1.3 AM overview

1.3.1 Advantages

AM is mostly used in applications that require low production volumes, small part size and complex design. However, to select the manufacturing method, there are many factors to consider: material, mechanical properties, volume required, complexity, accuracy, surface finish and cost.
Generally, the choice to adopt the AM compared to the CM lies on several benefits:

- Design freedoms: geometric complex parts can be produced at little or no extra

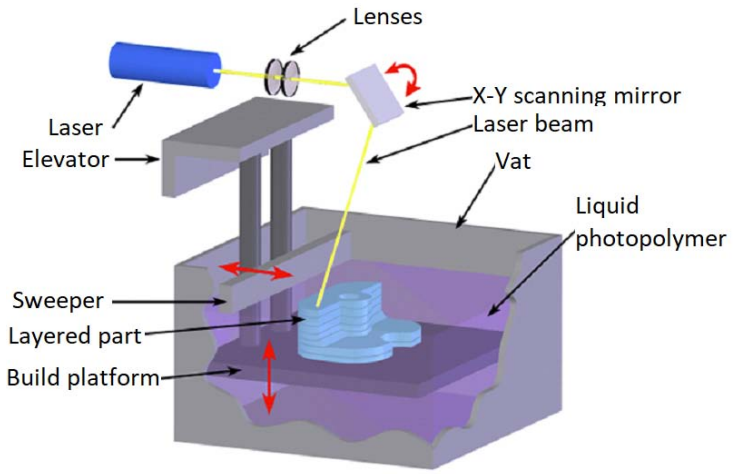

Figure 1.8: Vat photopolymerization.
www.tripodmaker.com/2016/02/22/3dprinting-technologies-overview

time or cost due to the absence of dedicated tooling. However, the design software used for CM struggles to represent efficiently the level of detail required for the AM technologies. Current software has been traditionally employed for CM processes that rarely produce complex structures such as lattices and complicated geometries.

- Material complexity: the material properties can be easily tailored, for example obtaining heterogeneous objects or using multi-materials from different print-heads.

- Hierarchical complexity: features can be designed with shape complexity across multiple size scales.

- Customization and personalization: each part can be different and tailored to individual users. The change in geometry, shape or size result in no extra money due to the absence of costs relating to tooling and changeover.

- Part consolidation: moving or functional parts can be manufactured in the same object during the process without further assembly. Moreover, more parts can efficiently be packed to print in the same build volume. Therefore, time and costs are reduced.

- Design optimization: to reduce the material used and thus the weight of the part without loosing performance, the part can be improved by optimizing its size, shape and topology. This results in the analysis of the most efficient size of the structural members, shape of the boundaries and material distribution. Therefore, the best trade-off between design and mechanical properties can be achieved after a series of iterations before printing.

- Potential environmental benefits: this is due to lighter materials (thus, less waste material is produced) and due to the conversion from a centralized to a distributed supply chain (thus, reduction in CO_2 emission).

- Ability to easily share designs and outsource manufacturing. Anyone could design everyday product at home or in the office and share it in a community website where it can be easily downloaded [2].

1.3.2 Limits

However, AM has still some limits that must be taken into consideration:

- Less availability of build materials: the use of non-standard materials produces an extra cost (material properties and price). However, during the last years due to the spread of the AM technolgies more and more materials are available with decreasing costs.

- A slow material deposition speed increases the indirect costs (time dependent).

- Generally, dimensional accuracy and surface finish are poor. Other limiting factors are the residual stresses, the anisotropy, the shrinkage and the minimum feature size achievable.

- Lacking process repeatability, often unacceptable degrees of variation of product characteristics.

- High costs at medium and high volumes: AM is not affected by the *economy of scale* thus for high volumes conventional manufacturing (i.e. injection moulding) is more reasonable. Indeed, in AM the unit cost, that is the total cost-quantity ratio, does not depend on the quantity produced. For instance, 3-D printing is cost effective with injection moulding when the volume of production is between 50 and 1000 units [5]. In the future, this range might be wider due to the increasing diffusion of 3D printers and the cost reduction [2].

- More than often supports are required to stabilize parts of the object (especially overhangs) during printing. As a result, material wastage and post-processing are needed reducing the overall efficiency.

- Lacking regulation, legal framework and unclear product liability situation. The availability of CAD design software may affect the intellectual property security. The risk of forgery and counterfeiting must be taken into account by the governments [2].

To summarize, compared to processes such as injection moulding or cutting-based machinery, AM efficiently manufactures complex geometries. The absence of dedicated tooling means that the AM methods are able to produce objects with a higher degree of complexity and functionality. Therefore, the end-use products have better performance over their useful live and this may allow the producer to charge higher prices for products generated with AM. On one hand, the fact that there is not dedicated tooling means the elimination of the tooling cost (no expensive molds or punches) and on the other hand, it is possible to manufacture individual units tailoring for a particular application. Personalized or customized products can be easily made and warehousing and logistics are no longer required since spare or replacement parts can be produced only when required. Moreover, AM enables to achieve lighter and strong part by means of lattice structures or efficient design topologies. Lastly, in comparison with multi-axis cutting machines, less waste material is produced. The reduction amounts to 40% even though the waste material can be used again [2].

1.3.3 Part quality

Regarding the quality of the parts manufactured by AM, each method has its unique features that affect the final properties of the product.
Concerning ceramics materials, not all the AM technologies enable high-quality parts [3]. It is well-known that the strength of a ceramic object depends on the largest flaw. A elemental volume can be thought as the volume where a flaw is present and all the volumes constitute a chain where the weakest link is the elemental volume that contains the critical flaw. Therefore, the mechanical properties of a ceramic part are strongly influenced by defects indeed even ceramic parts made with the same composition and treatment might show different values.
To take into account this phenomenon, an useful parameter is the Weibull modulus m. It describes the flaw size distribution and is a measure for the evaluation of the variability of the production process. When m is higher than 20, the material can be considered to have unique strength, while for ceramics m is usually between 5 and 20. This means that it is only possible to know how likely failure is at a given stress. Generally, the most critical flaws are cracks formed during the production process. The causes for the formation of cracks might be several. Normally, if the ceramic part is produced by single-step process, cracks can form due to thermal shock introduced by the laser beam heating. Instead, during multi-step processes, cracks form during the furnace treatment so the heating and cooling steps must be carefully selected to avoid too large temperature gradient.
Due to the nature of the AM process, pores can be considered the second largest flaws. In some applications (i.e. scaffolds, thermal insulation, energy absorption) pores can be an important and desired feature thus a trade-off between porosity and mechanical

strength must be found depending on the needs. Otherwise, the porosity can be minimized controlling the parameters during the printing, selecting a heat treatment that promotes a liquid-phase sintering or with extra densification steps (infiltration).
To conclude, if the ceramic parts is produced without cracks or large pores the mechanical properties are similar to those achieved by conventional methods. For instance, sheet lamination process allows to obtain parts with a density about 97 % even though the surface finish is very poor. Vat photopolymerization is one of the most exploited method for the production of functional ceramic parts since objects almost crack- and pore-free can be manufactured.

1.4 AM in the biomedical field

Nowadays, AM has many applications in the aerospace and automotive field, in the artistic, architectural and in the medical sector. From an American survey, the annual growth rate has increased by 26.2 % from 1991 to 2014 and more than 23,000 personal 3D printers were sold in 2011 compared to around 6,000 in 2010 [6]. These data prove the significant spread and impact of AM in the industrial market. The AM technologies in the medical field emerged in the last decade. Currently, the impact in medicine is still small: in 2014, the AM sector was a $700 million industry and only 1.6 % was linked to medical applications. However, by 2024 the AM industry may reach $8.9 billion with the 21 % projected to be invested on the medical field [7].

1.4.1 Advantages of AM in Medicine

Some of the previously cited benefits of AM have remarkable effects in the medical sector. First, the possibility to produce customized medical products or equipment has a positive impact on the success of the treatment and the surgery/recovery time. More interesting, other functionalities can be added to the implants such as drug or growth factors release personalized for each patient.
Second, due to the increase in the cost efficiency, for small quantity AM is increasingly becoming competitive since the realization of complex geometries and the recurring modifications are easier and faster compared to the traditional manufacturing [1]. Besides that, since 3D printing enables to achieve near-net-shape products the overall production process is quicker.
Lastly, as the materials cost is decreasing, even non-engineers people in medical field can design their products and contribute to the development of new concepts. An innovative reconsideration would be to make the surgeon the designer [8]. Surgeons, who often have new ideas that can be helpful to improve existing devices, could be involved in the

development and realization process thanks to the practicality of the 3D printing in order to create custom-built products. Consideration completely unfeasible with the traditional manufacturing where the gap between designers and those who really use the product is considerable.
To summarize, as the volume production in the medical field is rather small but with a high added-value values due to the complexity and high customization, AM seems to fulfill really well these requirements.

1.4.2 Limits of AM in Medicine

Although AM has been considered as the new industrial revolution [2] to exploit all its potential features we might still wait a dozen of years. Huge improvements have been achieved but there is still the need to invest a lot of money and time in this research to make many promising applications feasible (such as tissue fabrication). Moreover, a concern refers to safety and security. The more ease of printing objects might cause the diffusion of illegal items (even criminal) or counterfeit substandard medical devices and consequently there should be a more systematic control of the sources available. Another issue is how to apply all the copyrights, patents, trademark law for the use of 3-D printing as well as the procedure to obtain securing approval from regulators. In fact, there is a shortage of regulatory considerations regarding AM. Especially in medicine, the FDA (Food and Drug Administration) approval can slow down the distribution of medical equipment on a large scale. Furthermore, state legal requirements or manufacturing regulations can impede the production and dispensing of medications obtained by 3D printing [1].

1.4.3 AM applications in Medicine

The first applications of AM in the medical field date back to the early 2000s with dental implants and customized prostheses [9, 10]. So far, many improvements have been done indeed many published reviews deal with recent achievements in printing bones, ears, exoskeletons, windpipes, a jaw bone, eyeglasses, cell culture, stem cells, blood vessels, vascular networks and drug delivery devices [7, 11]. Here, some main fields have been covered.

1. **Bioprinting tissue and organs.** This idea (still at research level) arises from the fact that many cases of organs failure or dysfunctions are difficult to treat and often the only solution is to replace them by organs transplant. However, if we consider the situation in US, the availability of compatible organs is very worrying: in 2009, only 18% of 154,324 patients received the replacement whereas 8,863 died

while on the waiting list [1]. Indeed, the pursuit of a person with the same organ is very tough and expensive. To overcome these problems, bioprinting can have a promising role: after some cells have been isolated from the organ of the patient, they proliferate onto scaffolds in laboratory until the final transplantation (see fig. 1.9). This process is similar to the traditional tissue engineering, but the AM technologies allow higher control of the cell placement, speed, resolution, cell concentration, drop volume and diameter of the printed cells [10]. Taking the cells form the same patient results in the reduction in tissue rejection and in the need to take lifelong immunosuppressants. Nevertheless, we are still far from being able to 'fabricate' organs such as kidney, heart or liver since the culture of thick organs requires an accurate vascular network that has not been achieved yet. Inkjet-based technologies might be the most suitable for this area. In this way, bio-ink or droplets of living cells are deposited onto a substrate to reproduce human tissues or organs. Another possibility is to use multiple printheads to jet different types of cells mimicking the heterocellular structure of tissues.

The main challenge of printing engineered tissues with a thickness higher than 150-200 μm is that these do not allow the diffusion of oxygen, nutrients and growth factors between host and transplanted tissue [1]. Therefore, to print organs such as kidney, liver or heart there is the need for a better vascularization by means of precise multicellular structures and vascular systems.

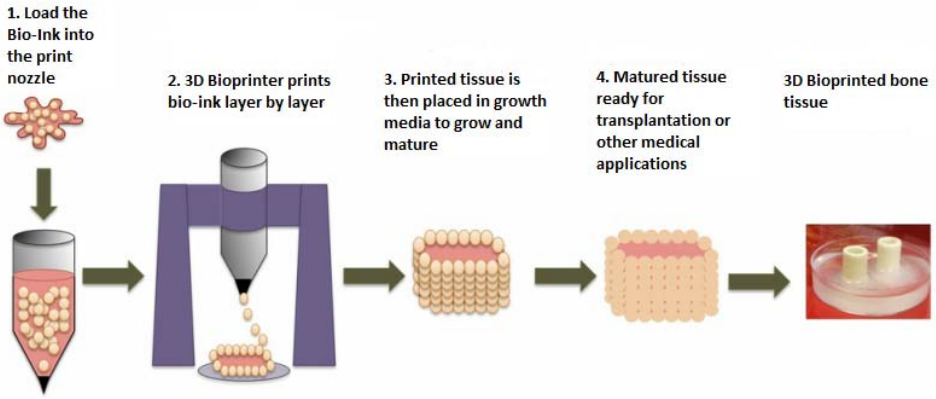

Figure 1.9: Basic tissue engineering procedure.
3dbioprinting.weebly.com/how-it-works.html

2. **Anatomical models for surgical preparation.** 3D printing has already been used as an ideal tool to achieve medical models to study, as surgery simulation and to rehearse transplantations since these 3D models give a more realistic view compared to a 2D scans from MRI or computer tomography (CT) (see fig. 1.10).

3. **Drug delivery.** Also this field has been positively affected by AM since many

Figure 1.10: Anatomical model made by 3D printing.
www.doctusproject.com/2016/09/22/3d-printing-future-medicine

drugs can be 3D printed with accurate control of droplet size, repeatability, dose and drug release profiles. Moreover, AM allows to obtain personalized dosage tablets, drugs for patients with very specific requirements or one multi-dose form for multiple chronic people. The drug release can be modulated creating porous matrix, barriers between the active ingredients or by functional geometries (see fig. 1.11 [12]). Ideally, the pharmacists could print and dispense the customized medication via an automated 3D printing system and if necessary the dose can be easily modified.
One of the most interesting direction is to print complex drug-release profiles so that, active and inactive ingredients can be organized in such a way the release can be controlled or facilitated due to the geometrical structure.
For instance, in 2016 the Aprecia Pharmaceuticals was the first company to obtain a FDA approval for a 3DP medicine for epilepsy.

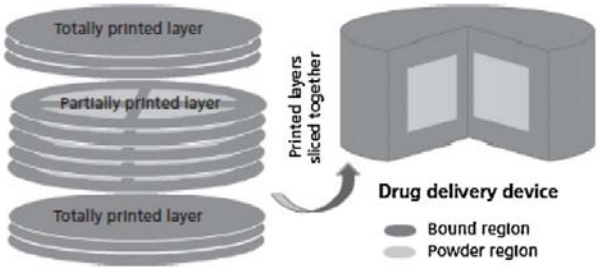

Figure 1.11: Schematic structure of fast dissolving drug delivery device.

4. **Implants and prostheses.** Implants and prostheses can be successfully made or designed by 3D printing after the conversion of X-rays, MRI or CT scan into .stl files necessary for the printer. The main advantage is that the implant can be designed according to the specific patient's needs (size, shape, fit) and therefore problems such as aseptic loosening, improper load distribution and discomfort can be prevented. The complex and customized shapes of the implants can fit really well with the

peculiarities of AM. With CV methods, sometimes surgeons have to perform bone graft surgeries or use scalpels or drills to modify implants by shaving the part to obtain the right shape. As a result, this process is time and cost-consuming as well as painful for the patient. Many research institutes have already printed titanium mandibular prosthesis, skull, orthopedic, maxillofacial, spinal and dental implants [9, 13, 14]. Everyday products such as hearing aids (see fig. 1.12a) and dental braces (see fig. 1.12b) have already been manufactured by AM. Indeed, 99 % of the hearing aids are customized and manufactured by 3D printing [1]. The following step may be to obtain implants with the incorporation of live cells.

(a) Hearing aids (with support structures).

(b) Invisalign dental braces by stereolithography.

Figure 1.12: 3D printed customized items.
www.3dprintingera.com/3d-printed-hearing-aid-for-the-perfect-fit
www.amosdudley.com/weblog/Ortho

1.5 Market overview

Market researches state that in 2012 AM reached up to €2 billion but more interesting, while the first billion was achieved in 20 years, the second one was attained only five years later (3D printing: facts & forecasts, Siemens). Till now, the layer-by-layer technology has mainly been adopted for rapid prototyping in different fields (aerospace, automotive, tool production, medical and dental sector) and the RP market is expected to grow from \$1.5 billion in 2012 up to \$5 billion by 2020. However, the most remarkable increase might be the manufacturing towards mass production through AM technologies. If this increase happens, the production process could be 50% cheaper and 400% faster from 10 cm^3/h in 2013 to 80 cm^3/h in 2023. Overall, the AM market growth might rise up to €7.7 billion in 2023 showing almost an eightfold expansion compared to 2010 (see fig. 1.13). After a worldwide survey of 900 companies the EY's Global 3D printing Report 2016 pointed out the following facts:

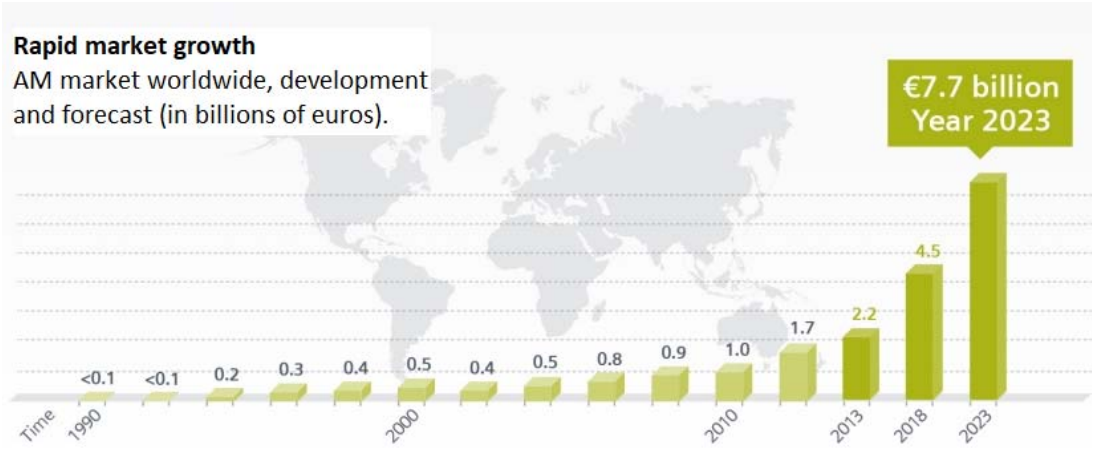

Figure 1.13: AM global market growth.

- 24% of the companies considers AM as a strategic or important topic for the business.

- 24% of the companies have already gained relevant experience with AM and 12% is considering to adopt this technology. Fig. 1.14 shows the different proportions for the surveyed countries: the major country involved in the AM technology is Germany.

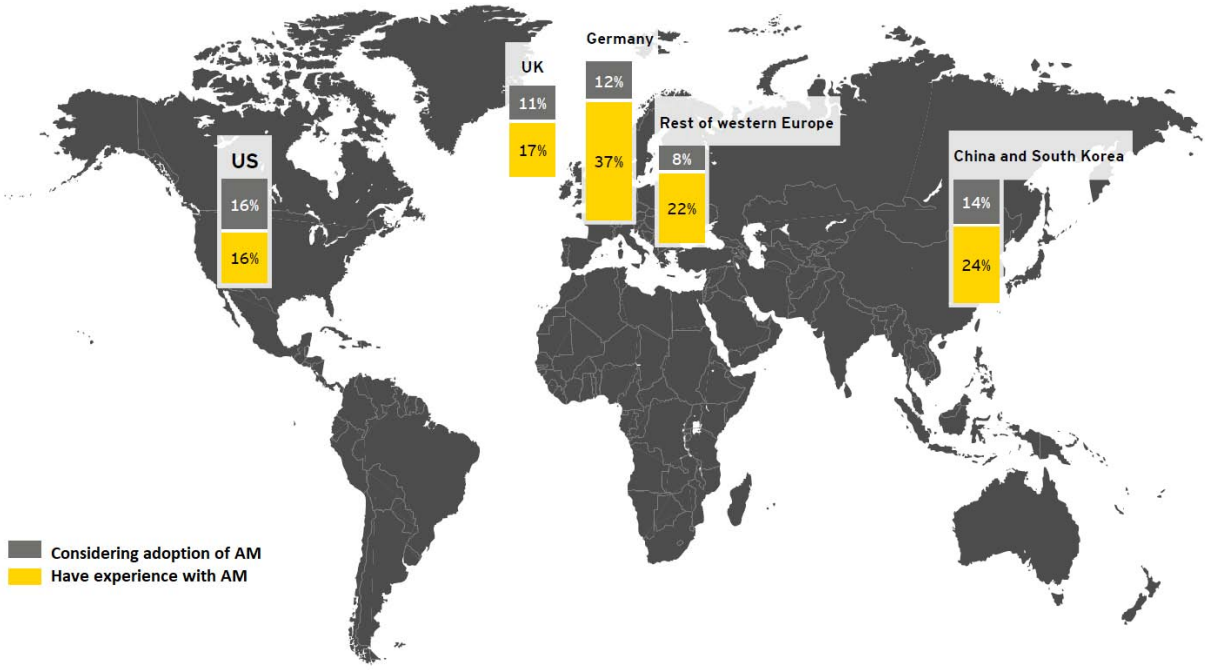

Figure 1.14: Current and intended acceptance of AM among countries.

- Around one third of the plastics, automotive and aerospace, pharmaceutical and medical companies that use AM apply it for printing their own end components or

products. Especially in the aerospace and automotive industries the main advantage is the light weight of the objects.
For instance, GE produces functionally integrated fuel nozzle for its best-selling product, the LEAP engine, saving up to $ 1.6m per aircraft per year in fuel reduction. The A350 XWB aircraft flies with more than 1.000 3D printed parts and it achieves 25% fuel savings compared to competitors. Lastly, BMW manufactured more than 500 water pump wheels for its racing car by 3D printing.

- 2% of the total revenue of companies with AM experience is generated with AM products.

- In the companies surveyed AM will be used: 19% as additional production technology, 15% part of hybrid technology and 12% as a replacement for traditional methods.

- The projections of the production of end objects with AM for 2021 are showed in fig. 1.15. The majority of Chinese and South Korean companies expects a great rise in the adoption of the AM technology.

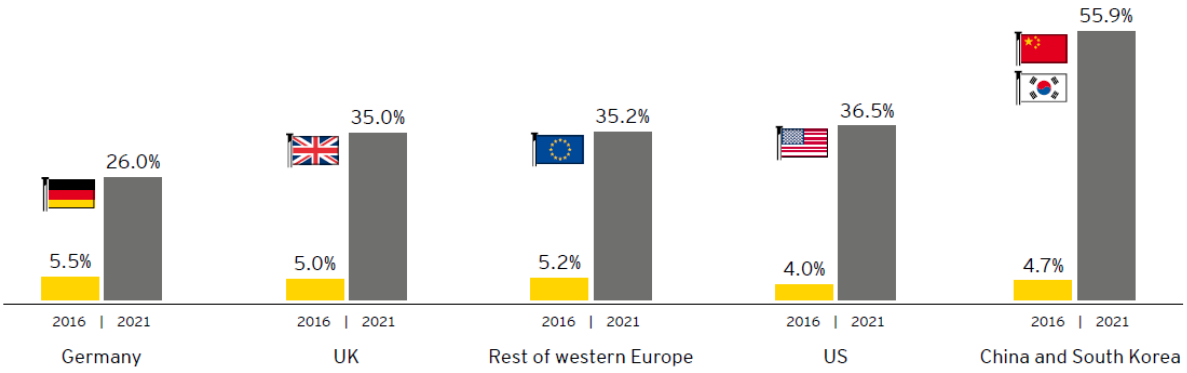

Figure 1.15: Forecast of the production of end-products with AM by 2021.

- Regarding the materials used, the main raw material belongs to polymers (53%), followed by metals (44%) and ceramic (10%). The selection of metals seems to be really promising for the production of precious metals such as titanium, tool steel and aluminum alloys and for a potential serial production using AM.

Also data from Statista shows AM market might grow significantly. Fig. 1.16 depicts the global projected increase by 2018: between 2010 and 2013 the market doubled, but the market in 2018 might be four times higher compared to 2013. Again, the market is considered to shift from RP to mass production by 2030 with the spread of different applications.

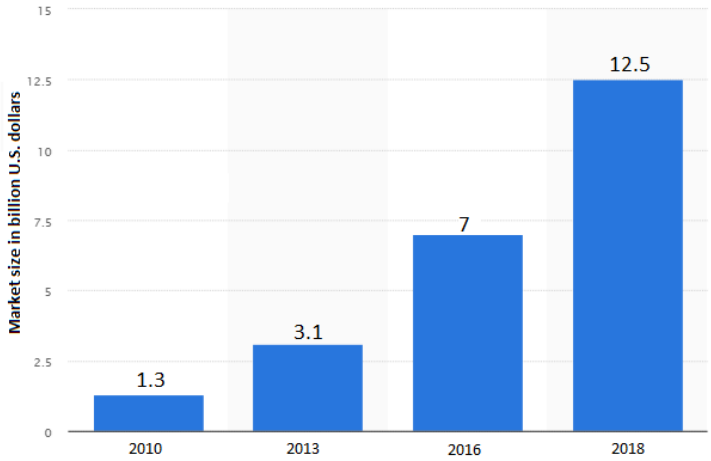

Figure 1.16: Projected global AM market size from 2010 to 2018.
www.statista.com/statistics/284863/additive-manufacturing-projected-global-market-size

1.6 Future trends

The future direction is to better exploit the main properties of AM focusing on the production of unique configurations in small volumes. The idea of printing parts quickly and cost-effectively allows firms to adopt a as-ordered basis concept without the risk of carrying an unsold finished goods inventory. Additionally, costumers could be able to purchase design online and then build products at home.
However, to fully consider AM as a competitive manufacturing method, some issues must be overcome. Regarding the material cost, currently it is 10 to 100 times higher than that traditionally used for injection moulding [2]. Material choice, color and surface finishes are more limited than the traditional manufacturing. Furthermore, the precision of the printing should be improved by around 10 times before it can compete with the other processes [2]. Other questions that must be further investigated deal with layers bonding, viscosity, dimensional stability, resistance to heat and moisture and color stability. Probably, if the price for the 3D printers decreases, there might be a wide diffusion of machines for home and industry applications. Thus, material cost could decrease due to the expansion of the higher market penetration.
Regarding the biomedical field, as previously mentioned in section 1.4.3, a future application might be the realization of organs by 3D printing (bioprinting) reducing the need for human organs and animal testing. Until now, many researches have been able to print a knee meniscus, a heart valve, a bio-resorbable tracheal splint, a spinal disk and other types of cartilage and bone [7,11]. But none organ has been successfully created yet. Following this path, it could be possible to generate a patient's tissue strip to evaluate what medication will be most proper and finally if stem cells are taken from a baby, he/she could have *a tool kit* for life in case the fabrication of an organ or tissue is required [7].

However, when this gets feasible, it may not be a common practice because not everyone could afford to pay for the own organ on demand. Anyway, many challenges must still be resolved and this can rise many ethical questions. The concept of the creation of organs is still far from the popular knowledge and might encounter many opponents. From an ethical point of view, someone could wonder until what point we can 'create' living organs and how safe the transplant will be in a long term perspective.
Moreover, there is the need to have a better control of the widespread of the AM technology providing standards and certification that can regulate and assure the quality of the process as well as the online data. The possible achievement of a printed human organ would be as difficult as the fact to convince people that this would be reality and not a futuristic vision of engineers.
Another important role of AM is its development in the pharmaceutical field providing new ways of drug manufacturing and distribution with savings in time and money. A patient could buy a single tablet that contains many active ingredients in order to reduce the medication burden making the administration less annoying. In addition, pharmaceutical companies could email the exact required amount of drug compound to the pharmacy and then the latter can print it autonomously.
Lastly, another future application might be the possibility of print in situ [15]. This means that implants or organs might be fabricate in the human body during the operations reducing the time of the whole process. The doctor might use a handheld 3D printer to repair directly tissue and internal organs through the deposition of cells, growth factors or bio-scaffolds. This can be considered still unrealistic but a human skin has already been treated by in situ bioprinting. In this case the skills and competencies of the surgeon would be completely mixed with a more engineering approach totally changing the preparation of these figures.

1.7 Final remarks

So far, in order to better understand the following chapters, an overview of this relatively new world of additive manufacturing has been given. The basic idea of the layer-by-layer process has been presented in section 1.1 and the two categories (*single-step processs* and *multi-step process*) as well as the seven types of methods (*material jetting, material extrusion, directed energy deposition, sheet lamination, binder jetting, powder bed fusion and vat photopolymerization*) have been considered (1.2). However, there are many other ways of printing parts that are not classified in the standard as more than often, they are customized methods for research purposes.
AM advantages and disadvantages are reported in section 1.3: when the part size is relatively small, the design is complex and the volume required is low, AM is a competitive

if not unique method to achieve these features. Nonetheless, accuracy, surface finish, mechanical properties are very variable among the different methods and often not enough for many applications (for instance, load bearing purposes).
An interesting field of AM is the biomedical one which will be the main topic of this thesis. Even though this sector has a small percentage in the AM market, the projections are positive and upward. Several applications with pros and cons (*bioprinting tissue and organs, anatomical models for surgical preparation, drug delivery and implants and prostheses*) are discussed in section 1.4.
Furthermore, to have a realistic and economic view of AM, a brief summary of a couple of market analyses are considered (1.5). Overall, the market size is expected to grow significantly reaching €7.7 billion in 2023 worldwide and the most promising direction might be the mass production through AM. The major leader in the AM sector is Europe (especially Germany and UK) followed by US and China. However, over the next years the latter countries might have the highest proportion in end-use products made with AM.
To conclude, some reflections about future trends are taken into account in section 1.6. Over the next decades, bioprinting organs, new drug profiles releases and printing in situ might not be as imaginary as now we think. Nevertheless, many challenges still remain unsolved but scientific community seems to be optimistic.

Chapter 2

Bioceramics

In this chapter a brief explanation about bioceramics is reported. First, a quick overview of the wider class of biomaterials is presented (section 2.1). Afterwards, section 2.2 introduces the category of bioceramics including a deeper discussion of bioceramic scaffolds (section 2.2.1), calcium phosphate (CaPs) and in particular about the properties and bioactivity of tricalcium phosphate, hereinafter TCP (section 2.2.2). Lastly, a further comment regarding the AM technologies for ceramic materials is outlined in section 2.3.

2.1 Introduction to biomaterials

Biomaterials belong to a particular class of materials intended to interact with biological systems and to perform with an appropriate host response in a specific application. So far, there are many materials used for different medical applications [16]:

- Titanium and Ti Alloys, stainless steel, polyethylene, cobalt-chromium alloys, hydroxyapatite, teflon, alumina and calcium phosphate are employed in skeletal system applications (such as joint replacements, fracture fixations, bony defect repair, dental implants);
- Teflon, polyurethane, stainless steel, carbon silicone rubber are used for cardiovascular systems such as blood vessel prostheses, heart valves or catheters;
- Polyurethane, silicone-collagen composite, silicon rubber are used to reproduce organs such as artificial heart, skin repair templates and artificial kidney;
- Platinum electrodes, poly(methyl methacrylate), silicon rubber, hydrogel, collagen and silicon-acrylate are used for senses such as cochlear replacements, intraocular and contact lenses and corneal bandage.

The biomaterials field is very wide and articulated indeed it involves the collaboration of researchers from many academic backgrounds. Indeed, the path for the implementation

of a medical device from the idea to the patient requires many steps as follows: *(1)* identification of a need, *(2)* device design, *(3)* material synthesis and testing, *(4)* fabrication, *(5)* sterilization and packaging, *(6)* device testing, *(7)* regulatory, *(8)* clinical use and *(9)* explant analysis. Obviously, the specialization in a sector is necessary to obtain greater results but at the same time an understanding of the overall mechanism is requested. Often, this field can be categorized in *hard tissue replacement biomaterials* or *soft tissue replacement biomaterials*. The first ones are linked to metals and ceramics involving orthopedic and dental applications while the latter deals mostly with polymers especially for cardiovascular and plastic surgery.
Depending on the use, biomaterials can have very different characteristics but to be considered *bio*material there are some essential features:

- bio-compatibility: the materials must not irritate the surrounding tissue, cause inflammatory response and cancer, trigger allergic or immunologic reactions;
- sterilizability: the material must undergo sterilization before being used (dry heating, ethylene oxide, steam autoclaving or radiation)

Clearly, adequate mechanical properties (strength, stiffness and fatigue properties) are also required.

2.2 Bioceramics

Ceramics employed in the biomedical field are called *bio*ceramics. They are used to repair, rebuild and replace diseased or damaged parts of the body and they can be distinguished between bioinert (such as alumina and zirconia), resorbable (such as tricalcium phosphate), bioactive (hydroxyapatite HA, bioactive glass, glass ceramics) and porous for bone tissue ingrowth (HA-coated metals). Most of the applications consist of replacements for knees, hips, teeth, tendons and repair for periodontal disease, maxillofacial reconstruction, stabilization of the jaw bone, spinal fusion and bone repair after tumor surgery. Many other uses can be found in the literature but only a few have achieved human clinical application since the regulatory is really strict and the trade-off between biocompatibility and mechanical properties is a tough goal.
For instance, bioceramics are requested to repair bone damage among the elderly that suffer from osteoporosis. As fig. 2.1 shows, the bone mass decreases with age especially for women after menopause (due to the lower level of estrogen). This results in a more marked bone vulnerability and likely fracture because the rate between bone formation (thanks to osteoblasts) and bone resorption (due to osteoclasts) reduces gradually. Thus, the aim is to replace the old and deteriorating bone with bioceramics with specific and demanding properties because the device operates under harsh conditions i.e. corrosive

saline solutions at 37 °C with variable, multiaxial, cyclical mechanical load. An essential

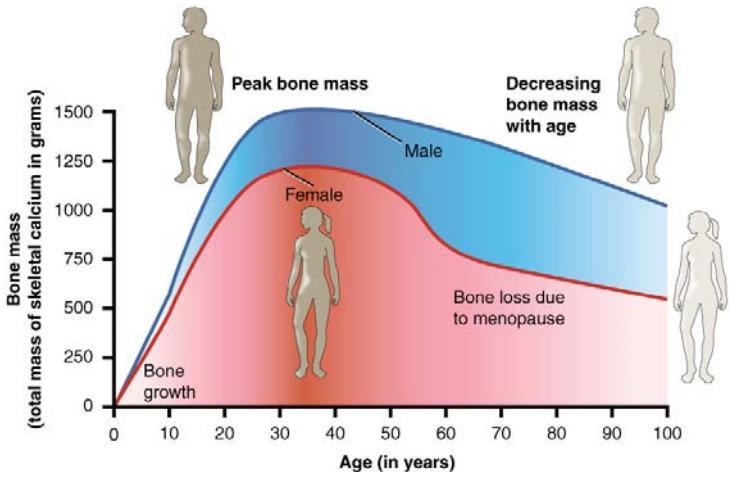

Figure 2.1: Decrease in bone mass with age. This phenomenon is more evident on women due to menopause.

opentextbc.ca/anatomyandphysiology/chapter/6-6-exercise-nutrition-hormones-and-bone-tissue

issue is the type of interface formed between the bioceramic and the tissue and as a result, the success of the surgery strictly depends on it. Four categories of responses have been distinguished [17]:

1. A *toxic* material causes the death of the surrounding tissue;
2. An *inert* biomaterial results in the formation of fibrous tissue;
3. An *active* biomaterial triggers an interfacial bond;
4. A *bioresorbable* material dissolves while the tissue grows replacing it.

Therefore, depending on these categories, the bioreactivity and the interface between bioceramic and tissue can be completely different. Fig. 2.2 depicts the relationship between the bioreactivity of the four categories and the bond at the implant interface over implantation time. An important effect is the thickness of the interface formed because most of the failures of the surgeries occur exactly in this area.
In nearly inert materials, a weak bond between implant and tissue results in a relative movement and loosening that eventually leads to a degeneration of the implant and the surrounding tissue. To increase the interfacial area and therefore the surface available to biologically or chemically bond to the implant, microporous bioceramics have been developed (also as a coating on metal implants to reduce stress shielding). In this way the new tissue can grow into pores on the surface or throughout the device. Unlike the simpler *morphological* fixation, these porous implants allow a *biological* fixation able to withstand more complex stress states. The interconnectivity and the size of the pores are

really important for the tissue regeneration: in isolated pores and with a diameter lower than 100 μm vascularization does not occur [17]. Further comments about the porosity will be discussed in section 2.2.1.

Regarding bioresorbable materials, their response is quicker and faster due to the dissolution of the material that allows the bone to recover all its functionalities by a continual turnover of cell populations. To ensure temporary performance the interface formed is very thin or nonexistent. The main challenge is to find out the best trade off between resorption rate and preservation of strength and stability of the interface. Tricalcium phosphate (TCP) is one of the most appropriate materials for the resorption and replacement of hard tissues if the mechanical requirements are not high due to its poor sinter activity [17]. Porous and resorbable ceramics used to fill bone defects are employed as cement or as *scaffolds*, that are porous templates for 3D tissue growth. More details about bioceramic scaffolds are covered in section 2.2.1.

Lastly, bioactive materials have a intermediate behavior between resorbable and inert materials. They elicit a specific biological response at the interface of the material, which results in the formation of a bond between the tissues and the material [18]. Examples are 45S5 bioglass, A-W bioactive glass and dense synthetic HA. It is important to remind that the attachment to the tissue is strongly affected by the type of material and very small variations in compositions have big consequences in terms of bioactivity.

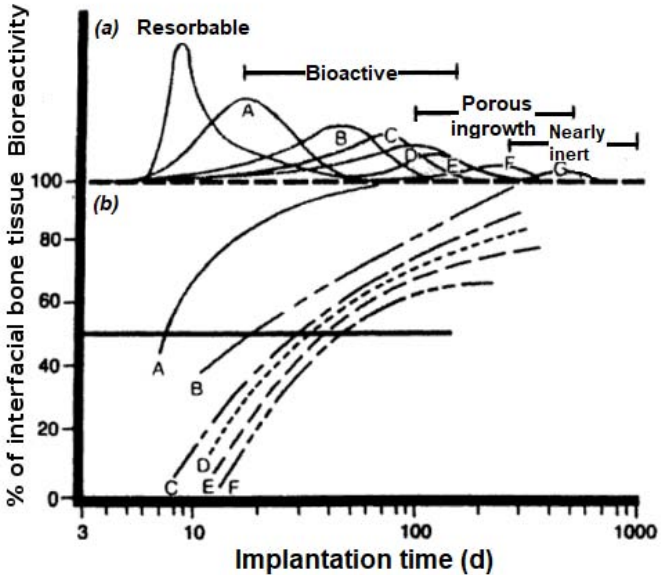

Figure 2.2: *(a)*: comparison of the bioreactivity over implantation time of resorbable bioceramics, bioactive (A is 45S5 bioactive glass B is KGS glass-ceramic), porous growth (C is S53P4, D is A/W glass ceramic, E is dense synthetic HA) and nearly inert impants (F is KGX glass-ceramic, G is Al_2O_3); *(b)* correlation between implantation time and formation of bone bonding at the interface.

Encyclopedic Handbook of Biomaterials and Bioengineering, Part B: Applications, Volume 2. Donal L. Wise, Taylor and Fracis, U.S.A,1995.

2.2.1 Bioceramic scaffolds

As explained in the previous section, one of the most promising applications for bioceramics is through the fabrication of scaffolds to substitute damaged tissues and to promote tissue healing. This field belongs to *tissue engineering* and is defined as *the interdisciplinary field that applies the principles of engineering and life science toward the development of biological substitutes that restore, maintain or improve the tissue formation* [19]. This relatively new study emerged as an alternative to tissue or organ transplantation that is a worrying topic because of the shortage of compatible donors [1]. For instance, in US every year there are around 6.3 million fractures that require expensive treatments. In 2005 more than 500000 bone graft procuderes have been carried out costing about $2.5 and 90% of them were autografts or allografts [20]. Like scaffolds, these are used for bone replacement but some disadvantages must be outlined [21].
An autograft is part of the bone obtained from another site in the same subject and it shows good response for bone repair and substitution. However, this causes additional expense and trauma for the patient and the availability is limited.
Conversely, an allograft (the bone is obtained from another subject) has a high cost and its supply is restricted and viral transmissions and infections are likely. Thus, printed scaffolds have promising application in this field.
In a nutshell, a scaffold is a synthetic framework that acts as a guiding 3D structure for both hard- and soft-tissue regeneration (see fig. 2.3 [22]). On one hand, this template has to withstand a specific load depending on the application, while the interconnected pores allow cell migration, adhesion and growth. Consequently, it is clear that there is an inverse relationship between mechanical response and porosity and this is the reason why the desired properties are difficult to achieve.
Some bioceramics such as alumina and HA form permanent scaffolds whereas

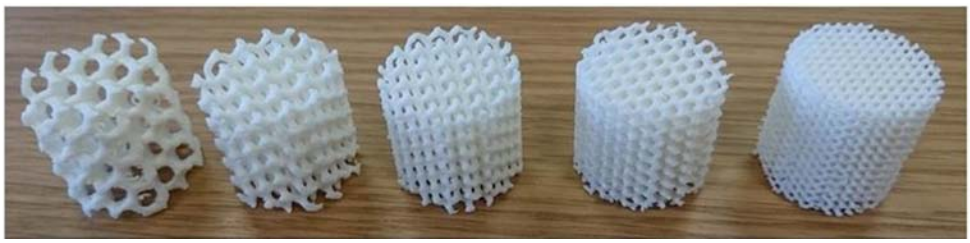

Figure 2.3: Different degrees of porosity in printed bioceramic scaffolds.

bioresorbable materials such as bioactive glasses or TCP degrade gradually. Therefore, it is important to assure that the breakdown products do not cause any adverse reaction and can be readily metabolized by the body. Moreover, the ions released (generally Ca, Si and Na) might be exploited for therapeutic effect such as promotion of angiogenesis and antibacterial properties [23].

In more details, the development of biodegradable scaffolds presents more challenges compared to the permanent ones: first, it is important to evaluate the loss in mechanical properties due to the degradation. Indeed, the strength and stability of the interface between scaffold and host tissue should be maintained steady throughout the resorption and the degradation rate should be compatible with the tissue regeneration. Another linked and difficult issue is to understand the most suitable resorption rate since it strongly depends on the gender, age and site of implantation.
Regarding the dissolution of the bioceramic scaffolds, there are two main mechanisms: *(1)* direct dissolution and release of ionic products that results in a increase in the local concentration of soluble species that interact directly with local cells or influence cell behavior by their effect on the local pH and *(2)* indirectly through the surface interaction with protein adsorption, growth factor and cell attachment [24].
To sum up, the most important design criteria to be considered are [24]:

- Geometry: the scaffold must match the complex shape of the anatomical defect to ensure a proper healing;

- Bioactivity: the scaffold should stimulate a rapid tissue attachment to the implant surface without the formation of a scar/fibrous tissue. Moreover, micromotion at the interface and inflammatory response should not occur. To avoid that, thanks to AM, the scaffold can perfectly match the bone defects and if it is not possible due to geometrical limitations, cements are used to anchor the scaffold to the bone;

- Biocompatibility: the scaffolds should support the normal cellular activity without toxic effects to the host tissue. Ceramics are very effective since they provide an environment where osteoblasts can adhere and proliferate. Conversely, biometals such as titanium alloys have been found to affect the release of inflammatory factors due to the loss of metal particles [20].

- Biodegradability: different materials have to be chosen depending on the degradation rate or to have a permanent device;

- Porosity: A high surface-to-volume ratio ensures the best interaction with the body and pores size along with interconnectivity are extremely critical to allow cell proliferation, tissue in-growth, vascularization and nutrient transport. A human bone has a a pore size between 10 and 100 μm in the cortical part whereas in the trabecular one it varies between 200 and 400 μm [21]. Besides, the porosity varies between 5 and 30% in the cortical bone and 30-90% in the cancellous part (see fig. 2.4). Thus, an ideal scaffold should have a similar porosity with a pores diameter range between 10 and 500 μm: the smallest pores (lower than 50 μm) promote protein adhesion, cell migration and osteointegration while macroporosity

(greater than 300 μm) is required for bone formation and ingrowth as well as capillaries formation [25]. Besides, the interconnectivity of the pores is essential to allow a continuous nutrient transport avoiding local increase of the pH due to ions accumulation;

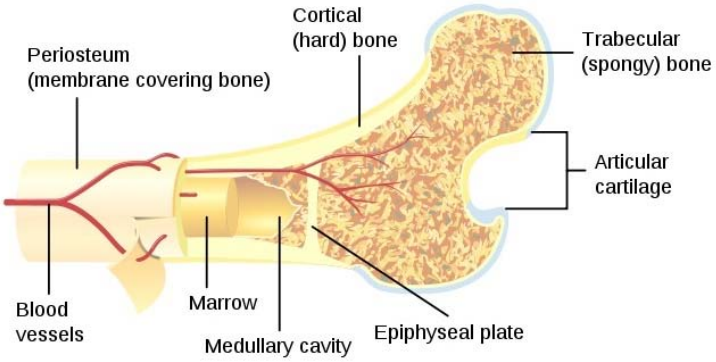

Figure 2.4: Structure of bone: the cortical part is denser than the trabecular one with different degrees of porosity.
biologydictionary.net/compact-bone/

- Mechanical compliance: they are established by the material and the porosity. The scaffold has to withstand implantation handling and support the stresses that the new tissue will ultimately bear. Thus, a balance between bioresorbability (promoted in weak lattice structures), osteoconductivity (promoted in porous structures) and mechanical properties has to be taken into account. Furthermore, the *stress shielding* must always be considered: if any kind of implant shows a too higher stiffness compared to the site where it has been located, the bone density will decrease due to a lower loading state (the device will support most of the load). As a result, the bone becomes weaker;

- Commercialization potential: a feasible industrial method of production should be adopted in order to fulfill repeatability and sterilization requirements. Currently, for the repair of small bone defects only porous scaffolds made of HA, biphasic CaP and bioactive glasses have clinical use in humans (FDA approved).

Lastly, the method of fabrication strictly depends on parameters such as pore size and distribution, interconnectivity, overall porosity, strut thickness and orientation. Also the volume of production affects the method chosen. So far, many techniques have been proposed: foaming methods, sol-gel foaming, *in situ* polymerization of organic monomer, sponge replication and layer-by-layer deposition [24]. All of them have advantages and disadvantages and for the aim of this thesis only the latter will be take into consideration. Generally, three AM techniques (discussed in section 1.2) have been employed to produce ceramic scaffolds [24]:

- SLA: it allows to obtain complex internal features but only feasible with ceramic/photopolymer blends;
- SLS: high accuracy can be achieved with good mechanical strength but high temperatures are required. The geometry must be carefully designed to avoid trapped powder;
- Binder jetting (3DP): relative fast process without toxic components and the mechanical properties can be tailored easily. Also with this technique powder might be trapped. This method will be deeply discussed in the next chapter.

2.2.2 Calcium phosphate and TCP

Calcium phosphates (CaPs) have been used in the biomedical field for more than 30 years especially for orthopedic and dental implants, maxillofacial surgery and scaffolds for bone growth [17]. Their excellent properties include their similar structure and chemical composition to the mineral phase of bone. Indeed, the human bone consists for about 70 wt.% of calcium phosphate mineral [26]. Moreover, CaPs are osteoconductive, that is the ability to provide a biocompatible interface with the bone and therefore avoiding the formation of scar tissue. Some outcomes from the literature about the bioactivity of CaP and in particular TCP will be extensively considered in section 2.2.3.
There are different phases of calcium phosphate and their stability depends on the temperature and water content [27]. For instance, at 37 °C in contact with aqueous media such as the body fluid, the pH determines the CaP structure: at pH lower than 4.2 the stable phase is $CaHPO_4 \cdot H_2O$ (dicalcium phosphate or brushite, DCP) while at pH higher than 4.2 the stable phase is $Ca_{10}(PO_4)_6(OH)_2$, (HA) [17].
Generally, the sintering process of the powder is carried out between 1000 and 1500 °C and HA may form at the expense of tetracalcium phosphate (TTCP) and tricalcium phosphate (TCP) if the partial pressure of H_2O [17] is relatively high. Thus, the parameters throughout the production must be controlled carefully.
TCP, that is the main topic of this thesis, is a calcium orthophosphate (CaP). The phases achieved after a treatment can be predicted by the phase diagrams but more than often the resulting phases are dictated by kinetic rather than thermodynamic considerations. TCP has a Ca/P molar ratio of 1,5 and three polymorphs exist [28]:

- β-TCP is stable up to 1125 °C;
- α-TCP is stable between 1125 and 1430 °C;
- α'-TCP is stable above around 1430 °C and it reverts immediately during cooling therefore it has not practical interest.

It is worthy to remark that the β α transformation is reconstructive [29], that is, *involves a major reorganization of the crystal structure, in which many bonds have to be broken* [30]. This means that the system requires a certain amount of energy to transform to one phase to another. Therefore the α phase can be retained at room temperature with a specific cooling rate. More details about it will be discussed in section 3.1 that deals with the synthesis of TCP.

To fully understand the different phases of TCP, it is essential to analyze the phase diagram of the binary system P_2O_5-CaO (see fig. 2.5 [31]) keeping in mind that often kinetic considerations prevail over thermodynamics in practical experiments.

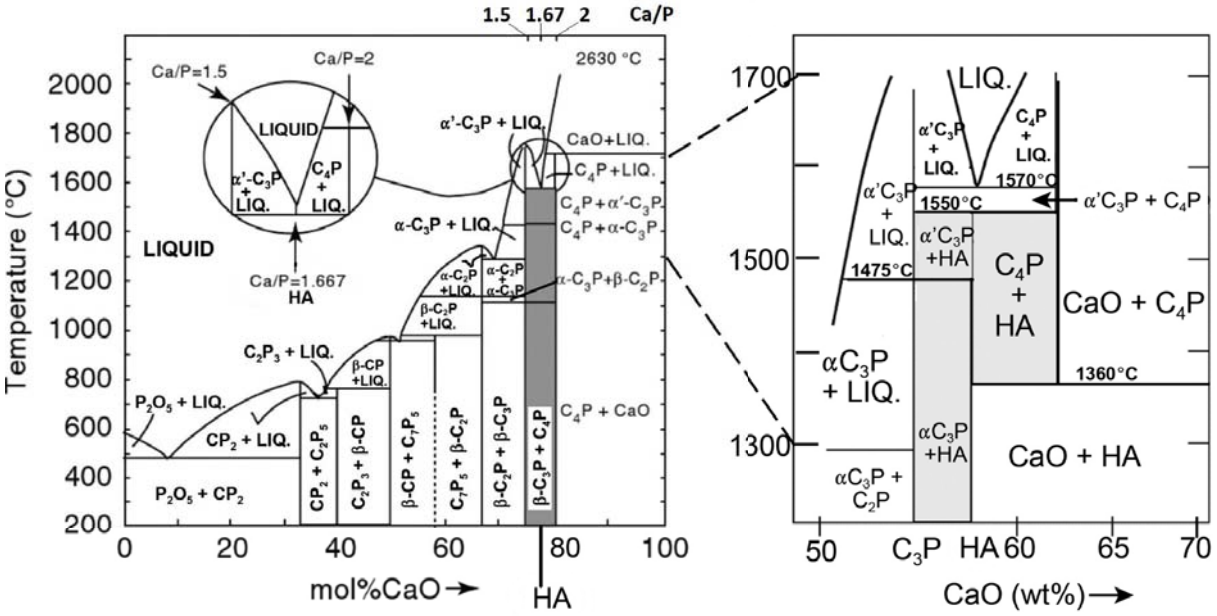

Figure 2.5: P_2O_5-CaO binary system. TCP and HA lie on the line of Ca/P molar ratio of 1.5-1.67 (upper X-axis). Legend: C_2P is dicalcium phoshpate, C_3P is tricalcium phosphate, C_4P is tetracalcium phosphate and HA is hydroxyapatite.

For the aim of this thesis only the range around Ca/P=1.5-1.67 will be taken into account since it corresponds to the presence of TCP and HA. Pure TCP lies in the vertical line at 55 wt.% of CaO, deviation from the exact ratio Ca/P=1.5 results in the formation of secondary solid or liquid phases. Apart from the above mentioned phases (β, α, α'), pure TCP melts at around 1750 °C. It is noteworthy that for the composition of HA, there is an eutectic point at 1570 °C.

A ratio slightly lower than 1.5 causes the formation of secondary phases along with TCP: starting from T lower than 1125 °C, the stable phases are β-TCP and β-DCP (or C_2P); for a small range of temperature (around 20 °C), β-TCP turns into α-TCP coexisting with β-DCP and then also the latter transforms into α-DCP. At T a bit lower than 1300 °C, the stable phases are still α-TCP but with the formation of a liquid phase.

Lastly, at T higher than 1475 °C, the α to α' TCP occurs in presence of liquid phase.
On the other hand, small deviation of 1.5 Ca/P ratio on the right of the phase diagram results in the formation of HA. Up to 1550 °C the usual transformations of TCP occur with HA as secondary phase. Then at higher T, HA turns into TTCP (or C_4P) with α'-TCP and lastly at T higher than 1570 °C TTCP melts.
The main structural data of the three different phases are showed in table 2.1 [32]. Despite their same composition, their behavior in terms of mechanical and biological properties and clinical applications varies significantly. For the aim of this thesis, it is noteworthy that the main feature to consider is the density difference between the three polymorphs of TCP. Especially during the cooling step of the sintering, parts may deform or crack due to the volume variation.

Table 2.1: Structural data of $Ca_3(PO_4)_2$ polymorphs. *a, b, c,* α, β, γ are the cell parameters, Z the number of formula units per cell, V the cell volume and D_{th} the theoretical density.

Property	β-$Ca_3(PO_4)_2$	α-$Ca_3(PO_4)_2$	α'-$Ca_3(PO_4)_2$
Simmetry	Rhombohedral	Monoclinic	Hexagonal
a (nm)	1.04352	1.2859	0.53507
b (nm)	1.04352	2.7354	0.53507
c (nm)	3.74029	1.5222	0.7684
α (°)	90	90	90
β (°)	90	126.35	90
γ (°)	120	90	120
Z	21	24	1
V(nm^3)	3.5272	4.31	0.19052
D_{th} (g/cm^3)	3.066	2.866	2.702

One of the main limitations of CaP scaffolds is their low mechanical properties (mainly brittleness and low fatigue strength) that narrow down the possible applications for only no-major load-bearing parts. This is correlated to the fact that during sintering, CaP scaffolds do not present viscous flow resulting in a low densification of the object.
An interesting method to increase the stability and the mechanical properties of scaffolds obtained by binder jetting is presented and followed throughout this thesis in section 3.2.1 where a gas flow sucks the powder through the build bed resulting in denser printed parts.
Regarding the applications, both α- and β-TCP are employed in many clinical practices in dentistry, maxillo-facial surgery and orthopedics for bone repair and remodelling. β-TCP is often used as a mono- or biphasic bioceramic and as dense and macro-porous blocks while α-TCP as a powder component and it may have promising applications as a scaffold. For instance, the german company *Biovision* provides pure-phase α-TCP granules (Biobase) for bone replacement or augmentation for temporary filling

pathological, traumatic and postoperative bone defects (see fig. 2.6 for a bone defect repaired with α-TCP granules).
Also another company, *Cambioceramics*, supplies α-TCP in form of cement powder for bone graft substitutes and dental applications. β-TCP can be employed for the same purposes but also for resorbable fixations mixed with hydroxyapatite.

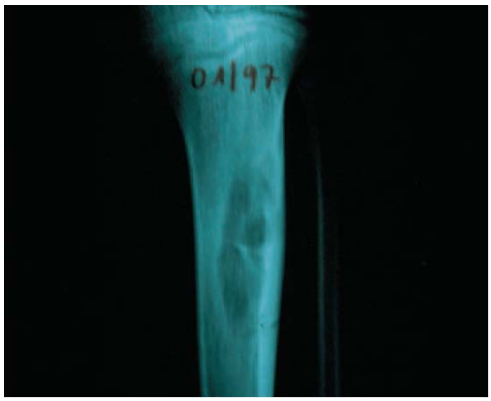

(a) Dysplasia in a human tibia.

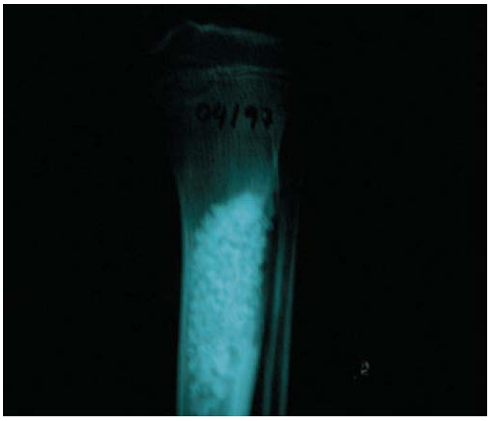

(b) Debridement of the fibrosis, filling the defect with Biobase.

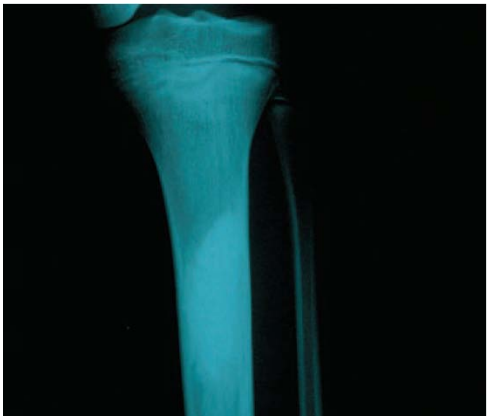

(c) After 13 months: bony growth and start of the resorbtion.

Figure 2.6: α-TCP used as bone replacement for bone defect.
www.biovision.de/DE/knochenersatz/biobase.html

About the biological activity, the degradation of α-TCP is faster compared to the low temperature phase due to the 'looser' structure. As result, that may promotes its wider use in biodegradable applications [32].
Specifically, the analysis of the Ca and P ions dissolved in a physiological pH (7.2-7.4) outlines the different dissolution rates of the main CaP: α-TCP dissolves faster than β-TCP and HA (see table 2.2 [21,32]). The latter seems to be the most stable compound

among CaP and the product of the degradation of α-TCP. This is the reason why HA is not the most suitable material for biodegradable scaffolds due to the extremely low resorption rate [33]. Furthermore, it has been reported that HA has the potential to be easily adsorbed by bacteria and epithelial cells due to its high surface energy and may be easily infected and encapsulated [34]. However, it is important to consider that empirically other CaPs may form from the dissolution of α-TCP due to deviations from the thermodynamic expectations.
Lastly, the solubility of α-TCP increases if the pH of the solution decreases and there are many other factors that influence the dissolution rate: the contact surface between α-TCP and the medium, the saturation of the mixing liquid, the use of degradation inhibitors or surface modification.
Having said that, it is clear that a complete analysis from the material properties to the bioactivity requires a great effort from several fields of the scientific community.

Table 2.2: Solubility of α-, β-TCP and HA. Ca/P is the molar ratio and K_{ps} is the solubility product constant.

Ca/P	Compound	-logK_{ps}		Solubility (mg/L)	
		25 °C	37 °C	25 °C	37 °C
1.5	α-$Ca_3(PO_4)_2$	25.5	28.5	0.97	0.24
1.5	β-$Ca_3(PO_4)_2$	28.9	29.6	0.20	0.15
1.67	$Ca_{10}(PO_4)_6(OH)_2$	116.8	117.2	0.00010	0.000096

2.2.3 TCP bioactivity

This thesis will not cover the biological response of TCP (in particular of α-TCP) but some outcomes from the literature will be presented in order to demonstrate the promising applications of α-TCP as a material for bone replacement. Not so many scientific papers are available in the literature and most of them deal with in vitro tests since in vivo test in animals required a considerable number of experimental subjects and they are rather time consuming. Nevertheless, the in vivo results agree with the in vitro data on comparative degradation of CaP biomaterials. Indeed, factors affecting the in vivo tests influence also the in vivo activity.
Having said that, the common idea is that α-TCP is more resorbable than its low temperature phase β-TCP in a simulated body fluid at physiological pH. This is clear from fig. 2.7 where the isotherms of solubility show the log[Ca] and log[P] versus the pH [32]. The solubility of α-TCP is higher than β-TCP and HAp (the precipitates of HA) at physiological pH. Furthermore, it is important to note that the biodegradation depends on the exact composition of the material, particle size, porosity (macro and micro porosity), surface area and cristallinity.

Lastly, α-$Ca_3(PO_4)_2$ has shown non toxic, antigenically inactive, non carcinogenic response and with a good biological compatibility and osteoconductivity in living tissues. Next, some articles from the literature are introduced to prove it but first, some essential considerations about the interaction between cells and TCP are taken into account.
The bioactivity of a material is the property to form a direct, adherent and strong bonding with the bone tissue. For CaP compounds this is related to the ability to develop carbonate HA on the surface when exposed to the simulated body fluid or in vivo conditions. It is worthy to note that the partial transformation of CaPs such as TCP to HA is possible only in an environment with Ca ions since the ratio Ca/P of Ha is higher than TCP (1.67 against 1.5 respectively). This layer of HA is considered to be a cell-mediated dissolution and precipitation process. Cellular activity promotes partial degradation of the CaP biomaterials and liberation of Ca and P ions onto the environment. Besides, other ions such as Mg or CO_3 from the biological fluid become integrated in the HA layer and all of this may trigger a mineralization of the extra cellular matrix leading to bone formation. Therefore, TCP is a osteoconductive biomaterial: this means that allows attachment, proliferation, migration and phenotypic expression of bone cells resulting in new bone formation. On the other hand, CaP materials are not considered osteoinductive, that is the property to form bone when implanted in nonbony sites, even though there are some reports that deals with this possibility [21].
Lastly, it is important to remember that during osteogenic culture in vitro the stem cells

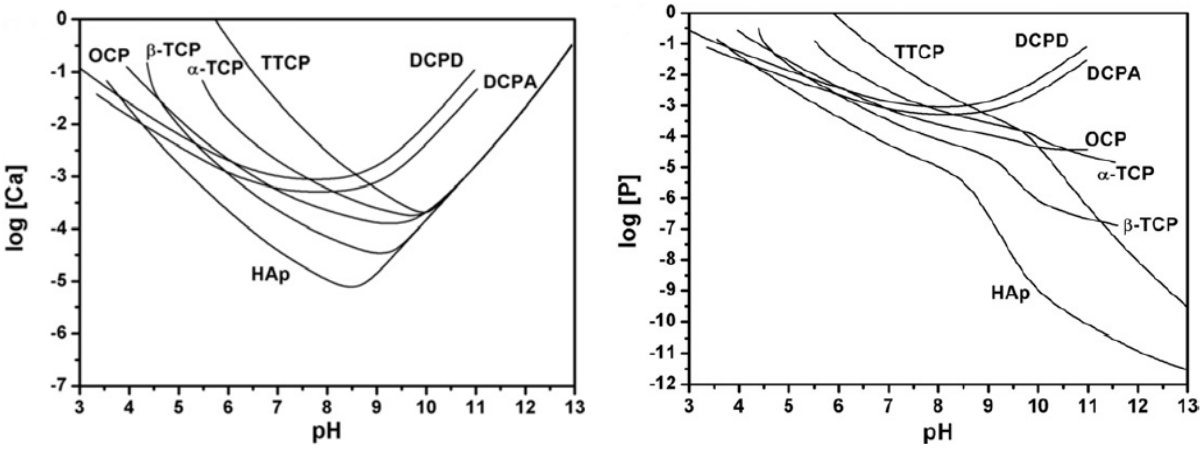

Figure 2.7: Solubility phase diagram for CaP materials at 37 °C: solubility isotherms showing log[Ca] *(above)* and log[P] *(below)* over the pH of solution in equilibrium with various salts. OCP: octacalcium phosphate, TTCP: tetracalcium phosphate, DCPD: dicalcium phosphate dehydrate, HAp: hydroxyapatite, DCPA: dicalcium phosphate anhydrous.

go through three different stages: cell proliferation, differentiation and mineralization of the extracellular matrix. Once the cells adhere to the implant, they start to proliferate

forming colonies and growing until different layers form. This can be analyzed by the transcription and protein expression of alkaline phoshatase (ALP) indeed during the early differentiation, this value increases significantly. After that, when the mineralization of the extracellular matrix starts, the ALP level decreases. Then, other markers are used to determine the beginning of the deposition of HA and often Alizarin Red is used to stain the formation of calcified nodule formation. In this way, thanks to these markers it is easy to control the bioactivity of TCP when in contact to stem cells in a culture medium [35]. Some main outcomes about TCP from the literature are now reported.

Martinez *et al.* [36] carried out in vitro cell tests of pure α-TCP and Si-doped α-TCP. Focusing on the pure phase, the authors analysed both static and dynamic in vitro test since the latter better mimics the biological conditions due to the continuous exchange of the immersion medium with a peristaltic pump (ensuring a constant circulation of physiological fluid). After two weeks of soaking in the SBF medium, pure α-TCP showed a positive growth of carbonate HA on the surface confirmed by XRD analysis: the surface layer reached 20 and 31 μm in static and dynamic in vitro test respectively. Static and dynamic in vitro test shown great difference due to the different driving force the ions are subjected to. In static SBF, the ions released from the surface (Ca^{2+} and ${HPO_4}^{2-}$) cannot easily diffuse and therefore there is a high concentration of these ions near the surface that results in the threshold of nucleation of HA. After the nucleation, the ratio between ions consumed from the solution and release from the surface is lower than one since the ions can only disperse by ion concentration gradient. In dynamic conditions instead, ions are driven by the different gradient of concentration and also by the stress gradient-driven ion transportation. This is called convective dispersion. In this way, the exchange of ion is easier and the concentration of ion near the surface is similar to that one in the fluid. The growth of HA on the surface is promoted as long as the exchange of ions occurs and the layer formed slows down the diffusion. The authors concluded that α-TCP can be an effective substrate promoter of bone tissue regeneration suitable for bioengineering. This was proved by showing a positive adhesion, proliferation and osteogenic differentiation of adult mesenchymal stem cell isolated from a bone marrow of three male human volunteers.

Seebach *et al.* [37] compared six bone-graft substitutes to investigate cell seeding efficiency, metabolism and growth behaviour of human mesenchymal stem cells (MSC). These different materials are: β-TCP (two types), α-TCP, silicate-substitute HA, bovine HA ceramics and human cancellous autograft. Geometrical and structural features (pore size, porosity, interconnectivity) of the scaffolds strictly influence the biological activity thus their properties are reported in table 2.3. Overall, the human cancellous autograft showed the best results even though all the materials had good bioogical properties. In particular, α-TCP revealed the second highest metabolic activity (see fig. 2.8), higher that

Table 2.3: Material properties of the different powder used for the scaffolds.

	Porosity (%)	Pore size (μm)	Chemical composition
Chronos	60	100-500	β-TCP
Vitoss	88-92	1-1000	β-TCP
Actifuse ABX	80	200-500	Silicate-substitute HA
Biobase	56-63	5-1000	α-TCP
Cerabone	50	100-1000	Bovine HA ceramics
Tutoplast	60-80	100-500	Human cancellous allograft

β-TCP. The results were obtained from the MTT assay, a typical measurement to check the cell viability and proliferation by the reduction of the yellow tetrazolium MTT by metabolically active cells. After 2, 6 and 10 days the metabolism decreased but it was still active after 10 days. From SEM analysis, cells were found on the surface and also within macropores. Fig. 2.9 depicts the α-TCP before and after 2 days of seeding. The formation of cells is clearly visible from the picture (see fig. 2.9b). The authors affirmed that the higher activity of α-TCP compared to β-TCP is due to its lower density and higher free energy of formation. Furthermore, the sterical constitution of the reactive groups of the two TCP affect the superficial charge. β-TCP is less negative charged than α-TCP and this may cause a different (and better) cell adhesion.

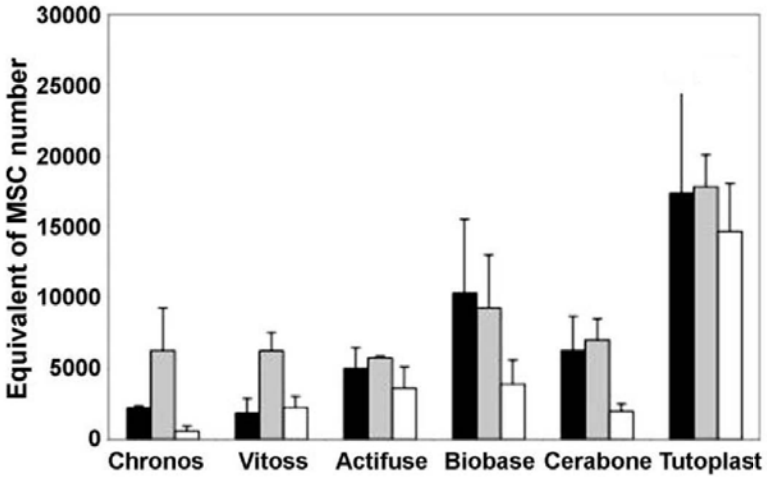

Figure 2.8: Metabolic activity of MSC attached to different scaffolds after 2, 6 and 10 days (black, grey and white bar respectively). Results obtained from MTT assay normalised to the number of cells in the scaffolds. The names of the scaffolds refer to Table 2.3.

Ehara *et al.* [38] examined the proliferation and function of osteoblast-like cells when exposed to α-TCP and TTCP using a preosteoblastic cell culture system. The pH of the differentiation medium was 7.41 and after the addition of 1 and 10 μM of α-TCP

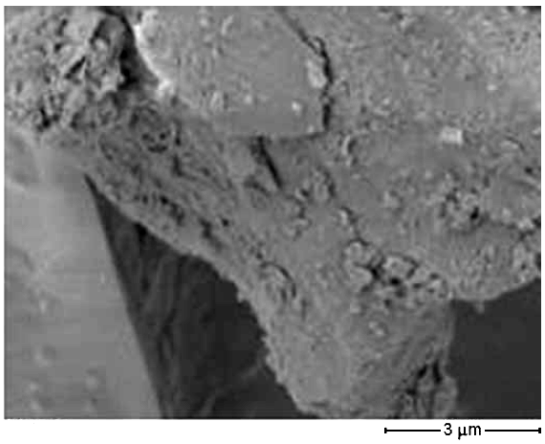

(a) Before cell seeding.

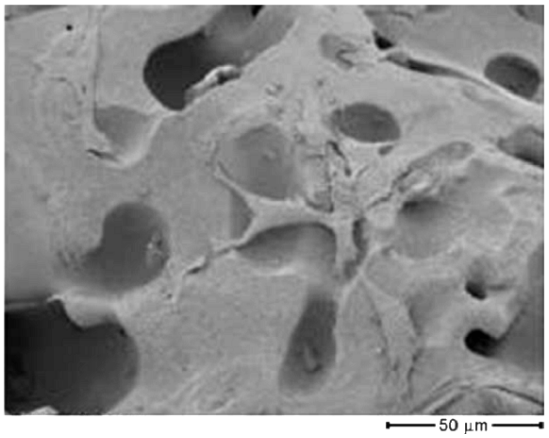

(b) After 2 days of MSC seeding on the scaffold.

Figure 2.9: Scanning electron microscopy of the surface of the α-TCP scaffold.

became 7.8 and 7.92 respectively. To evaluate the osteoblast differentiation, the alkaline phosphatase (ALP) was measured since an increase in this marker in a population of bone cells reflects a shift to a more differentiation state. α-TCP showed a grater activity for the culture after 3 days compared to the control and TTCP culture even though at day 7 there was a significant reduction. Moreover, to determine the presence of calcium phosphate deposit (that is, mineralized tissue in the culture) the plates were stained with Alizalin red S after 4, 7, 10 and 14 days. The results are show in fig. 2.10: the mineralization increased over time and when looking at the photographs after 14 days, it is clear that the well with α-TCP revealed a higher calcified tissue formation compared to TTCP and the control group. The two materials used enhanced the formation of calcified tissue since they act as suppliers of original material for bone formation (Ca and P). Indeed, the increase in Ca promotes calcium entry and an increase in intra cellular calcium storage. Besides, the increase in pH can release calcium from the intra cellular pool in osteoblasts and also it may be positive for calcium deposit.

Mayr-Wohlfart *et al.* [39] studied in vitro culture system to investigate the growth behaviour of human osteoblast-like cells in 3D scaffolds of α-TCP, a neutralized glass-ceramic, bioglass and a solvent dehydrated bone. All the scaffolds had a macroporosity between 200 and 2000 μm with interconnected pores. The authors confirmed that in all the scaffolds cells could cover the surface (despite a heterogeneous layer) and infiltrate the pores (see fig. 2.11) . The cells cultivated for 5 days were analyzed and the ratio APL activity - DNA content was measured; this parameter was nine times higher in α-TCP compared to the lowest activity (neutralized glass-ceramic) even though in the latter the cells proliferated faster. To conclude, this work proved that scaffolds made of α-TCP can promote in vitro growth and differentiation of human osteoblast-like

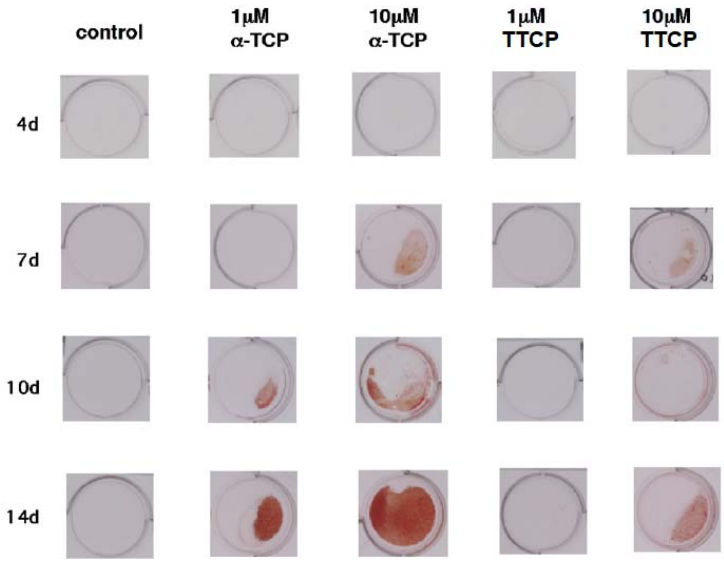

Figure 2.10: Photograhs of the wells stained with Alizalin Red S for identification of the calcium phosphate deposit in MC3T3-E1 culture in presence or absence of α-TCP or TTCP after 4-14 days .

cells in accordance with the previous studies.

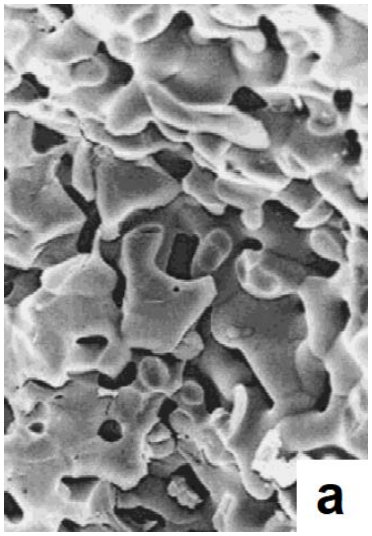

(a) Morphology of the scaffolds (magnification x200).

(b) Morphology of the scaffolds after 5 day colonization (magnification x2000).

Figure 2.11: α-TCP scaffolds after fracture preparation.

Igawa *et al.* [40] fabricated a tailor-made bone implant of α-TCP by ink-jet printing and HA as a control cut from a porous HA block (see fig. 2.12). They created two bone defects in the skull of seven Beagle dogs: α-TCP implant was allocated on one side and on the other side HA was implanted. To match the shape and size of the defects CT

analyses were carried out. CT images before and post implantation showed a remarkable effect of the TCP implant. Fig. 2.13 shows the skull pre and post surgery immediately and after 4 and 24 weeks. For α-TCP the holes in the implant became narrowed and the bone could bond better and faster to the implant. Moreover, a more significant invasion of bone tissue and bone marrow was observed in the cylindrical holes of α-TCP. In conclusion, the authors established that 3D ink-jet printing is an effective method to fabricate customized implants from CT data and the accuracy affects the regeneration of the bone since the HA implant was cut manually therefore it did not fit as well as the TCP one. This, along with the good osteoconductive properties of α-TCP, makes this material a safe and successful bone replacement.

Figure 2.12: Implant design model fabricated using CAD and the tailor-made bone implant after ink-jet printing.

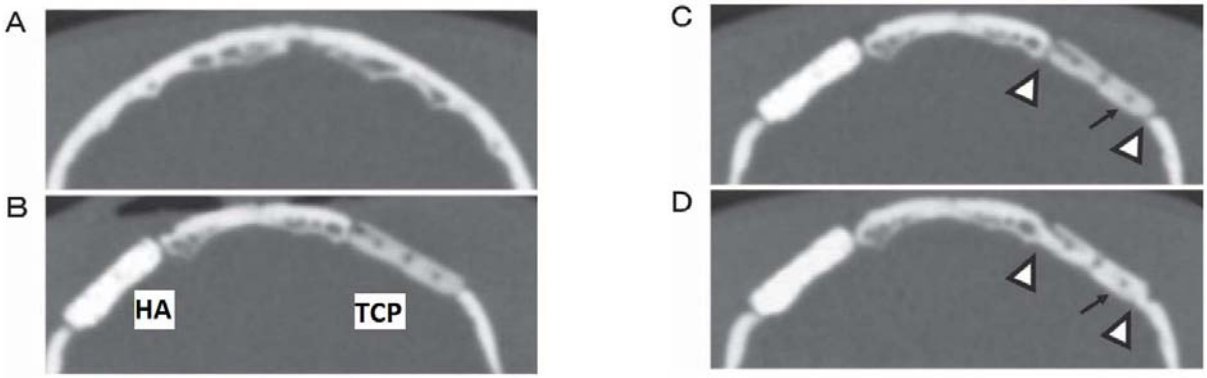

(a) **(b)**

Figure 2.13: Ct images of a Beagle's skull at pre-implantation (A), immediate post-implantation (B), 4 weeks (C) and 24 weeks after implantation (D). The arrows show the decrease in diameter of the holes in the implant and the triangles the bridges formed between the skull and the implant.

De Aza *et al.* [25] evaluated the bioactivity of α-TCP doped with Si in four critical size defects in rabbit tibias. The addition of Si is meant to further promote osteogenic differentiation of human mesenchymal stem cells and to decrease the beta to alpha transformation. They produced scaffolds with a porosity of 80% by the impregnation of a polyurethane sponge with the ceramic slurry. After 15, 30 and 60 days from the implantation the implants along with the surrounding tissue were removed and analysed. First of all, all the animals survived after 60 days and no evidence of inflammatory

response was reported. After 60 days the scaffolds were almost totally reabsorbed and new bone started to grow while in the control group no spontaneous defect closure was noted. From SEM investigations, the implants were well integrated into the host tissue and the formation of a rough surface denoted their degradation. To sum up, the high inter-connectivity of the scaffolds fulfilled the nutrient transportation and the cell tissue ingrowth requirements. Si-αTCP promoted bone formation and a higher degradation rate and this is compatible with the bone deposition rate because the formation of the fibrous tissue was limited. Therefore, the TCP scaffolds were able to transform into a bone-like structure when exposed to the natural environment.

Wiltfang *et al.* [41] carried out a study filling bone defects in the tibia head of minipigs with α- and β-TCP granules. Overall, the degradation and resorption of the implants did not show significant differences and both could be classified as bone-rebuilding materials. After 86 weeks from the implantation the ceramic remained in the defect was around 5 and 3 for α- and β-TCP respectively. In contrast, the control animals resulted in an incomplete reossification with rarefication of the bone in the defect after 16 weeks. The slight faster degradation of β-$Ca_3(PO_4)_2$ can be caused by the different morphology of the granules used. β-TCP had spherical shape, a mean diameter of 1-2 mm, a porosity of 45-50% with interconnected pores and the phase was confirmed to be 99% pure β-TCP. On the other hand, the α-TCP granules were bigger (3.2-5mm), with a porosity of 40% with closed pores and the phase was not confirmed so other phases could exist. Thus, all these different features could have delayed or affected the degradation. Bigger granules mean a lower surface/volume ratio and therefore a lower interaction with the tissue; similar consideration for the lower porosity and the closed pores that strongly reduces the ions diffusion through the material; lastly, the presence of secondary phases may change the biological response with the surrounding environment. In conclusion, considering the final results of the two TCP almost similar although these differences that may 'disadvantage' α-TCP, this can be confirmed to be a promising material for bone replacement.

Yamada *et al.* [34] compared the bioactivity of porous blocks of α- and β-TCP allocated in slits made in the cranial bone of rabbits. These blocks were implanted in a titanium chamber and to obtain comparable results, compaction, porosity (around 50%) and volume were equal. The specimens were evaluated after 2, 4 and 8 weeks and overall α-TCP showed promising outcomes. After 2 weeks both TCP demonstrated almost absent degradation but from week 4 in α-TCP some inner cavities were noticed close to the host bone. After 8 weeks, while for β-TCP the difference was not so significant compared to the previous four weeks (see fig. 2.14a), in α-TCP the cavities reached about one third of the height of the block (see fig. 2.14b). Therefore, this results in a large amount of new bone formation that invaded the α-TCP with remarkable degradation. This seemed to be aligned with bone formation while the newly formed bone that surrounded α-TCP

became incorporated into the bone remodelling cycle with the residual particles.

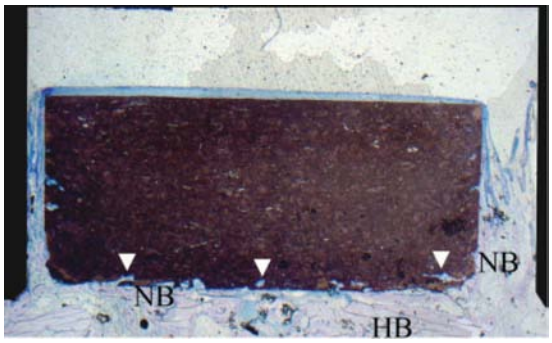

(a) β-TCP group (dark color) implanted in a Ti chamber.

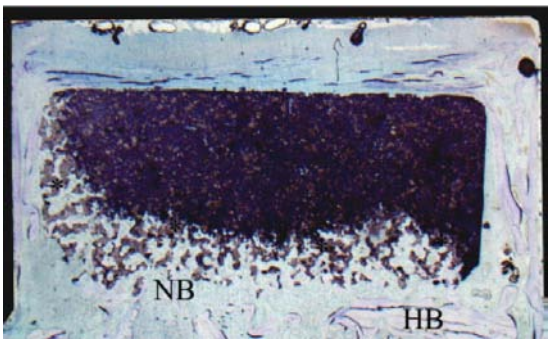

(b) α-TCP group (dark color) implanted in a Ti chamber.

Figure 2.14: TCP group after 8 weeks of implantation. α-TCP group has a higher degradation rate since more new bone formed inside the chamber in contact with the host bone (HB). Triangles are the concavities in the block of the newly formed bone (NB). Magnification x5.

Liu *et al.* [35] examined the effect of α-TCP on the osteogenic differentiation of rat bone marrow stem cells. The MTT assay revealed that 10-20 μg/ml of TCP in the culture medium had good biocompatibility with the cells without affecting their proliferation. Moreover, when incubated with cells in a osteogenic culture medium the values indicating an increase in the osteogenic activity. The ALP marker proved a strong osteogenic inductive effect of α-TCP in the early stage of the stem cells differentiation. Besides, after 21 days, the effects of α-TCP on the formation of mineralized nodules compared to the control group was clearly noticeable (see fig. 2.15): the red area (by Alizarin red staining) was significantly higher in the TCP group as a result of its greater osteogenic activity.

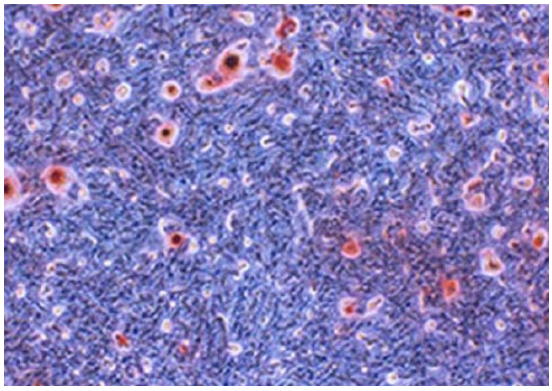

(a)

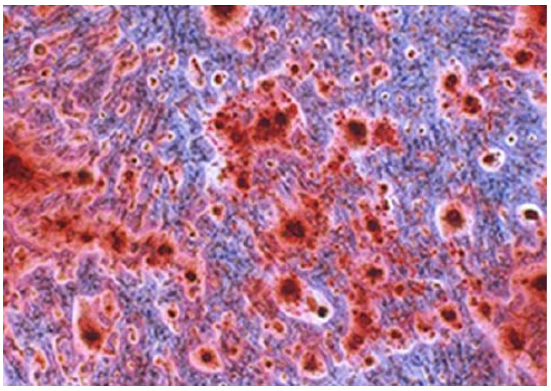

(b)

Figure 2.15: Effect of α-TCP on the mineralization nudule formation. Control group *(a)* and experimetal group (*(b)*.

2.3 AM of bioceramics

In this section, a deeper discussion about AM of bioceramics will be covered as the field of biomaterials and AM have been introduced separately at the beginning of this chapter and in chapter 1 respectively.
As already mentioned, in the AM technologies, the geometrical and material design can be successfully customized according to the own requirements also for ceramic based components. Indeed, with CM methods, ceramics are difficult to manufacture and to optimize due to their brittleness, hardness and the need for high temperatures [42]. Instead, near-net-shaped 3D ceramic based parts are feasible with AM. This means that there is no need for post hard machining (diamonds tools are usually required) that is time consuming and expensive (the cost increase may reach up to 80%) [43,44]. Moreover, design optimization and prototyping can be carried out more easily and quickly reducing the overall fabrication time and cost.
Currently, the main challenges are the dimensional accuracy and the surface finish due to defects coming from the layer upon layer method itself. Indeed, a typical imperfection is called *staircase effect* due to the slicing of a contoured surface (see fig. 2.16).
Furthermore, the accuracy of the part is influenced by the material properties (for

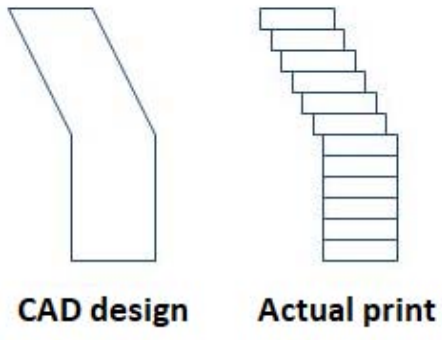

Figure 2.16: Staircase effect: the profile of the printed part does not match perfectly the CAD file due to the slicing. Indeed, with AM processes the parts are made of layers with vertical edges.

3dprinterchat.com/wp-content/uploads/2016/06/Staircase-effect.jpg

instance, fine powder produces a smoother surface but the flowability is lower), ink parameters (such as viscosity and solid content) and extrusion factors (such as jetting rate, nozzle travel speed, distance between the nozzle and the layers). To improve the texture of the part the layer thickness or secondary operations (grinding or polishing) can be adopted but this results in an increase in production time and costs as well as the risk to damage the part.
Another consideration regards the printers available in the market: most of the AM techniques have been commercialized for the production of polymers and metals parts.

Therefore, the current research focuses on the fabrication of ceramic parts by adapting the already existing machines.
So far, AM technologies have mostly been exploited to obtain porous structures: this is not because they can perfectly control the percentage of porosity but because these processes themselves result in a certain amount of residual porosity that is tolerated or even desired (for instance, when the aim is to mimic the human bone structure). Generally, a bimodal porosity can be distinguished: the designed porosity (0.5-2 mm) and the microporosity due to the incomplete densification. This is due to the use of high particle size (30-100μm) in order to have a good flowability during the deposition. Pores smaller than 500μm cannot be printed due to the limited resolution and the difficulty in removing the excess powder. Therefore, on one hand, this overall high level of porosity enhances the bio-properties but on the other hand it limits the mechanical properties (in scaffolds made of calcium phosphate the compressive strength varies around 20 MPa [42]).
A final consideration has to be pointed out. Without a doubt, AM technologies for metals are more mature and the main difference concerns the material feedstock [42]. The success of metals in this field regards on their high weldability that allows to obtain dense parts (up to 99%). The welding can be triggered by either a laser or electron beam while the sintering for ceramics is possible only with the former due to their low electron conductivity. Moreover, a deeper expertise about the handling of metal powder and the metal-laser interaction exists. However, the main challenge for the ceramic AM sector seems to be the match between a specific AM method with the selection of a proper feedstock that allows to obtain dense ceramic parts with optimal features. With regard to the material availability, nowadays this is not a problem anymore since a wide and high quality range of ceramic powder in the appropriate size can be easily found [42].

2.4 Final remarks

In this chapter, an overview of bioceramics with a deep discussion about α-TCP has been reported. In section 2.1 the wider category of biomaterials has been introduced showing that there are many different materials used in this field. However, all of them are connected to the term *biocompatibility*: they are not toxic or injurious and do not cause immunological rejection with living tissues. Bioceramics have been covered in section 2.2. This important class of materials can improve significantly the well-being of the patients since medical devices can be made ad hoc fulfilling all the requirements. Bioceramics can repair, rebuild and replace damaged parts of the body reducing the pain for the patient. A typical case is the treatment of osteoporosis with bioceramic powder to replace and promote the remineralization of the bone. Particularly interesting are the bioresorbable ceramics that degrade gradually providing essential ions for the new

ossification that occurs at the same time. In this way, at the end, there is no evidence of the surgery done since the material only promotes a natural healing. For this aim, scaffolds are often used (section 2.2.1): these 3D porous templates allow tissue ingrowth thanks to the different degree of porosity and biocompatible properties. In future, scaffolds may completely substitute the use of autografts and allografts that have many limiting factors. Nonetheless, the design of a scaffolds must consider several parameters such as bioactivity, shape, porosity and interconnectivity, mechanical requirements and commercialization issues.

Tricalcium phosphate is a promising candidate for bone replacement (section 2.2.2) whose features have been widely investigated including the phase diagram P_2O_5-CaO, structural data, degradation and applications. Currently, the main drawback of α-TCP is its low strength that limits its use only for no load-bearing practices. Moreover, various outcomes from the literature have been pointed out in section 2.2.3 in order to show the osteoconductive properties of α-TCP.

Lastly, a further comment about AM in bioceramics has been covered to understand problems and advantages of this technology for biomedical applications.

Chapter 3

Methods

In this chapter, the main procedures and methods used will be covered. Section 3.1 deals with the TCP synthesis starting from $CaCO_3$ and H_3PO_4. Afterwards (section 3.2), a deep analysis of the parameters affecting the 3D printing is reported to understand how each factor is connected to the properties of the final part. To increase the stability of the powder bed, a new and promising method called *powder-bed stabilization through a gas flow* is also presented and its effects will be broadly evaluated in the following chapters. Lastly, some basic concepts about the sintering process (section 3.3) and the mechanical test used (ball on three balls test, section 3.4) are pointed out in order to have a whole overview for the next chapter.

3.1 TCP synthesis

In the market, many different degrees of β-TCP can be found whereas there are fewer suppliers of α-TCP throughout the world but even so, specifications and chemical characteristics are difficult to obtain.
In the literature, several procedures have been developed to achieve α-TCP by thermal transformation of a precursor with molar ratio Ca/P close to 1.5. Some processes include [32]: thermal decomposition of calcium-deficient HA at temperature higher than 1150 °C, thermal transformation of amorphous calcium phosphate at temperature around 1130 °C or phase transformation starting from β-TCP at temperature higher than 1130 °C. Besides, a variety of solid-state reactions to get α-TCP are available.
Next, some issues to take into account during the synthesis of α-TCP are reported.
An important factor that significantly affects the transition temperature is the ionic substitution in TCP. Ions such as Mg, Sr and Zn that partially substitute Ca increase the thermal stability of β-TCP by increasing the β to α transition temperature. This is a method used to sinter β-TCP without phase transformation and achieving a higher final density. On the other hand, SiO_4 promotes the α-phase when it replaces PO_4 to some

degree. Moreover, SiO_4 seems to promote the osteogenesis during the tissue regeneration but no clear confirmations have been found yet [45].
One of the main problems to obtain one single phase is linked to thermodynamic considerations: during cooling from the α-phase, there might be a partial re-transformation to β-TCP or a formation of other phases such as HA. Theoretically this should be unfeasible (unless a very slow cooling rate is used) since the β α transformation is reconstructive so a significant energy is necessary for the transition. However, the presence of β-TCP after cooling from the α-phase can be caused by: *(1)* the transformation β to α has not finished due to a temperature not high enough or a short dwelling time, *(2)* the equilibrium temperature has been reached but because of the presence of impurities (Mg, Sr or Zn) the transition temperature is higher, *(3)* a slow cooling rate has promoted a partial reversion [32].
Furthermore, generations of second phases after cooling can be due to a deviation from the theoretical Ca/P molar ratio 1.50 in the starting material or due to even small degree of humidity in the laboratory during the synthesis.

3.1.1 Synthesis procedure

To produce α-TCP, calcium carbonate ($CaCO_3$) and phosphoric acid (H_3PO_4, 85%) have been used. Compared to the other traditional methods, the main benefits are the fast reaction rate, the fine particle size achievable and the minimum impurity [46].
The steps followed are:

- H_3PO_4 (88.02 ml) is poured into a porcelain dish containing $CaCO_3$ powder (193.63 g);
- The powder is dried (100 °C for a couples of hours);
- The powder is milled until a fine and uniform powder is achieved;
- First heat treatment, constant heating rate of 600 °C/h (see fig. 3.1):
  1. 400 °C for 1 hour
  2. 800 °C for 1 hour
  3. 1000 °C for 1 hour and air quenching;
     These three steps are thought considering the reactions listed next.
- The powder is milled again;
- Second heat treatment:

1. 1600 °C for 2 hours and air quenching.

- The powder is milled and sieved.

Pt-Ir and Pt-Rh crucibles are used for the first and second treatment respectively. Seven batches have been produced obtaining around 1 Kg of powder.

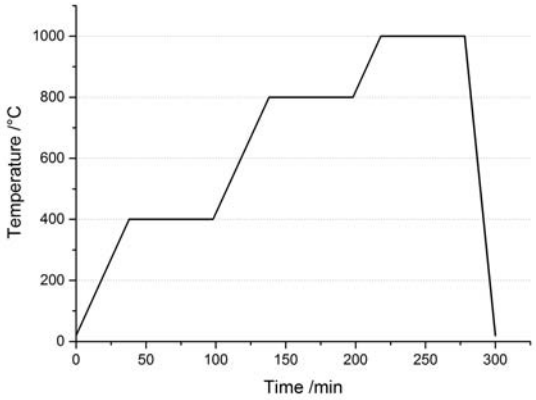

Figure 3.1: First treatment to obtain nearly one phase β-TCP.

The most likely reactions occurring during the first treatment consist in the formation of a precursor between $CaCO_3$ and H_3PO_4 namely octacalcium phosphate (OCP), with the chemical formula of $Ca_8H_2(PO_4)_6 \cdot 5\,H_2O$ ([46,47]). Compared to the traditional method, instead of non-stoichiometric HA, the less acidic systems (pH around 5.5-6.5) and the formation of CO_2 during the process promote the formation of OCP that is calcinated at 1000 °C for 1 hour.
Another aspect regards the particle size of $CaCO_3$. The powder used has a particle size of 14 μm and that allows a more uniform and fast reaction with H_3PO_4 since finer particles have a larger surface area and therefore more reacting surface. Indeed, as the particle size decreases, the amount of β-TCP increases at the expense of DCP and monetite ($CaHPO_4$) [47].
The reactions suggested by [46, 47] are listed below:

$$8\,CaCO_3 + 6\,H_3PO_4 \xrightarrow{RT} Ca_8H_2(PO_4)_6 \cdot 5\,H_2O + 8\,CO_2 + 3\,H_2O \quad (1)$$

$$Ca_8H_2(PO_4)_6 \cdot 5\,H_2O \xrightarrow{200} Ca_8H_2(PO_4)_6 + 5\,H_2O \quad (2)$$

$$Ca_8H_2(PO_4)_6 \xrightarrow{400} \gamma\text{-}Ca_2P_2O_7 \quad (3)$$

$$\gamma\text{-}Ca_2P_2O_7 \xrightarrow{800} \beta\text{-}Ca_2P_2O_7 \quad (4)$$

$$CaCO_3 \xrightarrow{850} CaO + CO_2 \quad (5)$$

$$\beta\text{-}Ca_2P_2O_7 + CaO \xrightarrow{1000} \beta\text{-}Ca_3(PO_4)_2 \quad (6)$$

By combining the previuos formulas starting from OCP, the overall reaction is:

$$Ca_8H_2(PO_4)_6 \cdot 5\,H_2O + CaCO_3 \xrightarrow{1000} 3\,\beta\text{-}Ca_3(PO_4)_2 + CO_2 + 6\,H_2O \qquad 7$$

It is important to note that the reaction 3 must have other products to maintain the ratio between Ca and P. Further comments will be presented in section 4.1.2 comparing the XRD results of the final product.
Afterwards, the second treatment results in the transformation to the α-phase,

$$\beta\text{-}Ca_3(PO_4)_2 \xrightarrow{1600} \alpha\text{-}Ca_3(PO_4)_2 \qquad 8$$

Even though the transformation phase occurs at around 1150 °C, to obtain a sintered cake to be milled the temperature chosen was 1600 °C.
Lastly, the α-TCP powder has been ground with a ball miller and then sieved to achieve two different particles sizes whose specifications have been obtained by laser diffraction method (see also fig. 3.2):

- lower than 25 μm: d_{50}=8.63 μm, d_{90}=24.00 μm, d_{97}=88.88 μm;
- between 45 and 100 μm: d_{50}=49.14 μm, d_{90}=102.80 μm, d_{97}=127.21 μm;

For simplicity, from now on, the powder with particle size lower than 25 μm will be called *fine* powder while that one between 45 and 100 μm *coarse* powder. It is noteworthy that both powder present a trimodal distribution indeed the gaussian curve can be thought as the combination of three other curves; this may increase the compaction during the printing process.

3.2 3D printing

In this section, more details about the printing process and the printer will be covered.
The printer used is a commercial 3D printer (RX-1, ExOne, USA) and the basics of binder jetting have already mentioned in section 1.2. In more details, the powder bed consists of two compartments called feed and build bed (7 x 5 x 2.5 cm) (see fig. 3.3): at the beginning the feed bed is lowered so that all the powder can be accommodated while the build bed is in the upper position. Once the powder is spread homogeneously through a roller, the first layer can be printed: the print-head (that moves along the Y axis, see fig. 3.4), scans the area on the build bed and jets binder creating the first cross section (the binder used is ethylene glycol monomethyl ether). Generally, for a layer more passes are required depending on how many jets are currently working. Once the first layer is printed, the powder bed moves along the X axis under the heater to make the binder dry

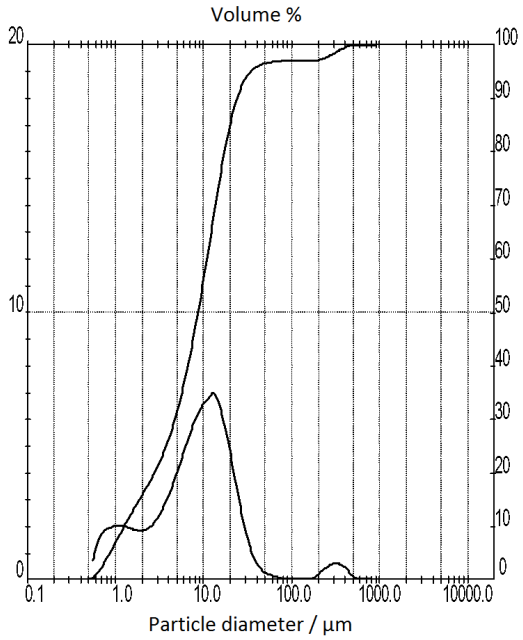

(a) Particle size distribution of the fine powder.

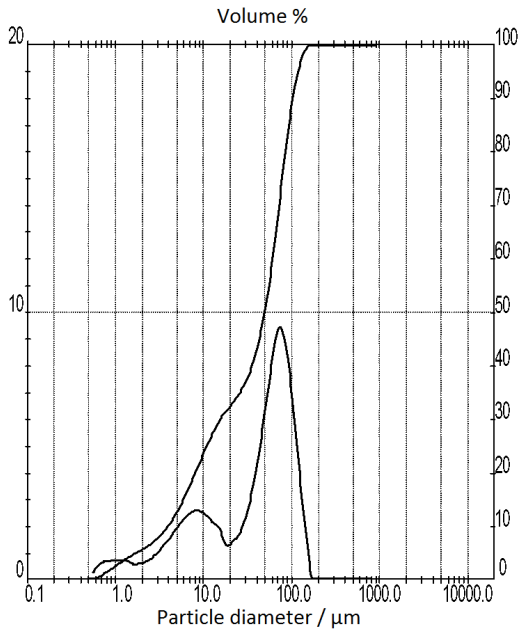

(b) Particle size distribution of the coarse powder.

Figure 3.2: Particle size analysis by laser diffraction.

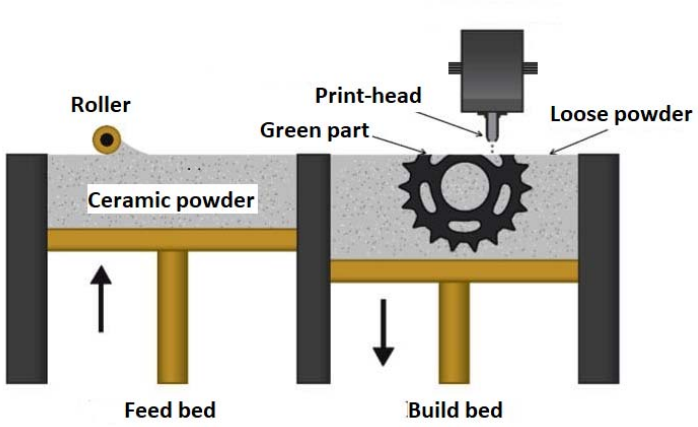

Figure 3.3: Powder bed of the 3D printer.

www.fabbaloo.com/blog/2017/11/10/how-to-compare-the-various-metal-3d-printing-processes

and afterwards a new layer is spread. This means that the feed bed is lifted and the build bed is lowered so that the powder can be spread from the feed to the build bed through the roller. These steps occur until all the part is printed. Moreover, after a certain number of layer an automatic cleaning of the print-head occurs in order to prevent the jets from clogging.

Lastly, it is important to make other two general considerations: firstly, the function of

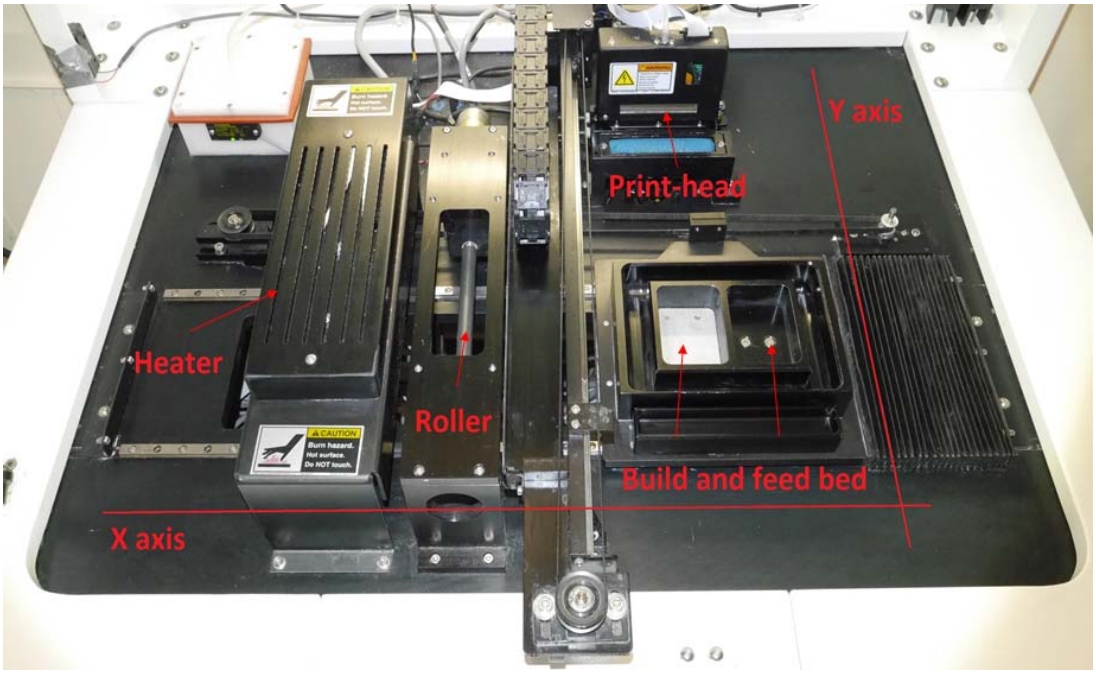

Figure 3.4: 3D printer setup.

the binder is only to glue the particles together and it must not react with the powder. Then, during the sintering, it will burn out. Secondly, one of the advantages of the powder bed deposition is that the powder that is not printed acts as a support for the part thus, theoretically, distortion should be minimized and support structures (for instance, for overhangs) should not be required.

Before every printing it is really important to check if all the jets are working since some of them might be clogged and even after some cleaning cycles they are still blocked. To do so, a pattern is printed onto a paper sheet in order to evaluate which jets is not working and therefore disabling the missing jets, the remaining will work also for them avoiding to lose the quality of the part (however the printing time increases significantly). Picture 3.5 depicts the print-head used: Fujifilms SE 128AA. Some of its features are: 128 nozzles available, nozzles diameter = 35 μm, drop mass = 30-100 pL, drop velocity = 10 m/s, binder viscosity = 8-20 cP and vapor pressure lower than 50 mbar. It is interesting to see the extreme low amount of binder that can be jetted and the high speed the binder exits from the nozzle with.

To print, two files are necessary: the process file and stl.file. The first contains information about the material and the printing. Indeed, here can be found settings such as the layer thickness, the binder density, the powder packing rate, the saturation, the drying time, the spread speed, the build to layer thickness ratio and the cleaning parameters. Instead, details about the shape and the dimension of the part are found in the stl.file.

As mentioned before, there are several parameters that affect the final part:

- **particle size**: the features of the powder are essential for good printed parts.

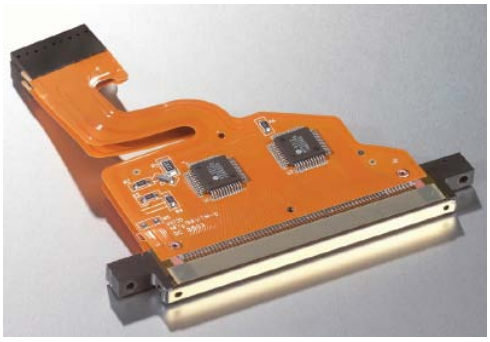

Figure 3.5: Printhead used for the binder jetting (Fujifilm SE 128 AA).
www.fujifilmusa.com

Generally, coarse particles have a higher flowability compared to fine powder that shows a higher interparticle attraction due to the larger specific surface area. On the other hand, finer particle might allow a better resolution and more accurate details. Even the geometrical shape has an influence in the process since spherical particles present a better deposition than irregular ones. Moreover, a larger particle size distribution enables to obtain good results with a wider range of parameter possible since the flowability is higher but the precision and the density decrease [48].
Regarding the sintering process, generally ceramics have a poor sinter activity since they do not show glassy phases that help the densification. To solve this problem, additives can be used to promote liquid formation or change the transition temperature. Another way is to use fine particles since the densification is strictly inversely dependent on the diameter of the particle.

- **layer thickness, *LT***: it is the thickness of each layer. Generally, the minimum limit matches the largest particle size so it is reasonable to take into account d_{90}. The layer thickness is probably one of the main parameter that determines the quality of the part and the final mechanical properties. Usually, as the thickness decreases, the processing time and mechanical properties rise. However, not always the change of the parameters results in a linear dependence. The unit is expressed in μm.

- **Hausner ratio, *HR***: the HR is the main parameter that gives information about the flowability of the powder. It is defined as follows:

$$HR = \frac{\rho_{\text{tap}}}{\rho_{\text{bulk}}} \tag{3.1}$$

where ρ_{tap} is the density of the tapped density after a certain amount of tapping cycles (500-600) and ρ_{bulk} is the untapped density. The closer HR to one, the more flowable the powder. Usually, finer particles are less flowable due to the higher

surface energy and therefore the high attractive interparticle force that impedes an easy and regular deposition.

- **powder packing rate, *PR***: this parameter defines how packed the particles tend to accommodate spontaneously. It is expressed as follows:

$$PR = \frac{\rho_{\text{bulk}}}{\rho_{\text{th}}} \tag{3.2}$$

where ρ_{bulk} is the density of the untapped powder and ρ_{th} is the theoretical density. Obviously, a higher PR means denser parts.

- **powder bed density**: it is the density of the powder in the build bed after a certain number of depositions. After the printing parameters have been chosen, 50 or 100 layers of powder are deposited and after that, the mass is measured to calculate the density of the powder bed (the volumes is that one of the build bed). This value is linked to the flowability and capacity of compaction of the powder during the printing.

- **spread speed**: this value (expressed in mm/s) refers to the speed of the bed during the spread of a new layer (the roller rotates only). Two values can be chosen: the *build speed* and the *feed speed*. The former is the speed of the bed when the roller spreads the powder on the build bed whereas the latter is the speed of the bed when the roller collects powder from the feed bed. This parameter can be selected separately because the effects of the roller in the two beds is different: in the feed bed the roller is gathering powder while in the build bed the powder is released. This seems a banal note but especially with fine powder these two speeds have a great consequence on the uniformity of the layer. For instance, if the feed speed is 10 mm/s and the build speed is 5 mm/s, when a new layer has to be deposited, the powder bed moves under the roller with a speed of 10 mm/s while the roller is collecting powder from the feed bed and then at 5 mm/s when the roller spreads the powder on the build bed.

- **feed to layer thickness ratio, *FLT ratio***: this ratio defines how much the feed bed raises compared to the layer thickness. For instance, with a LT of 100 μm and a ratio of 2, for each layer the feed bed is lifted of 200 μm. Depending on the properties of the powder, it might happen that with a low ratio the powder is not spread uniformly throughout the bed.

- **binder**: proper rheological properties of the binder are essential for a good printing. The viscosity greatly influences the definition of the details of the part: a high viscosity tends to make the jet difficult and the glue might not penetrate enough

into the powder. On the other hand, a low viscosity causes a poor definition that results in geometrical deviations.

- **drop volume**: it is the measurement of the volume of each drop of binder that is released from a nozzle on the print head.

- **saturation percentage, *S***: this parameter depends on the drop volume, packing efficiency and the binder viscosity. It is defined as [48]:

$$S = \frac{V_{\mathrm{b}}}{(1 - \rho_{\mathrm{bed}}/100\%) \times a \times b \times LT} \tag{3.3}$$

  where V_{b} is the volume of an individual binder droplet ejected by the print head expressed in pL, ρ_{bed} is the density of the powder bed after a certain amount of depositions, a x b is the lateral pixel area for one droplet on the substrate expressed in μm^2 and LT the layer thickness. a x b x LT is the volume that can be considered as the three dimensional analogous of a pixel, called voxel. Thus, S refers to the amount of binder used to glue a certain quantity of powder and it can be thought as the ratio between the volume of binder spread out in a voxel and the free volume not filled with powder in the same voxel. Therefore, a higher saturation results in a stronger part but if it is too high the binder will bleed into the surrounding powder whereas a value too low makes the part too weak due to the poor bonding of the layers [49].

- **drying time**: after the jetting of a layer the binder has to dry. A proper dwelling time must be chosen in order to stabilize the just printed layer (to avoid little movements of the printed part during the spreading). A typical drying time is 60 seconds.

3.2.1 Powder-bed stabilization through a gas flow

As mentioned in the previous section, the unglued powder acts as a support for the part against gravitation. Despite that, during the spread the part can undergo a lateral displacement due to the roller and this results in a poor stability of the part (see fig. 3.6, [50]). To overcome this problem, support structures are required for the fixation of the desired geometry within the powder bed. However, this causes an increase in processing time and wasted material. Another drawback is that the removal of the support structures is time consuming and a very delicate operation since the green part can be easily damaged. Besides, this step cannot be easily automatised. Lastly, the support structures might introduce internal stresses or deformations to the part thus a careful analysis of the design must be done.

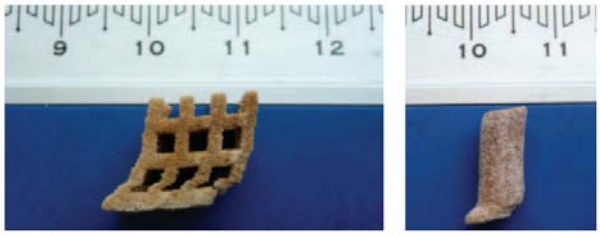

Figure 3.6: Deformation along the spreading direction of scaffolds 3D printed without support.

Another approach that will be followed in this thesis is to stabilize the powder bed through a gas flow so in this case the supports are unnecessary. This method is patented by BAM ([51]). The setup used is depicted in fig. 3.7 [50]: the build bed is formed of a porous sinter-steel filter (mean porosity 10 μm), a felt filter, its support and the platform in which the vacuum connector is attached. In this way the powder on the bed is sucked downward

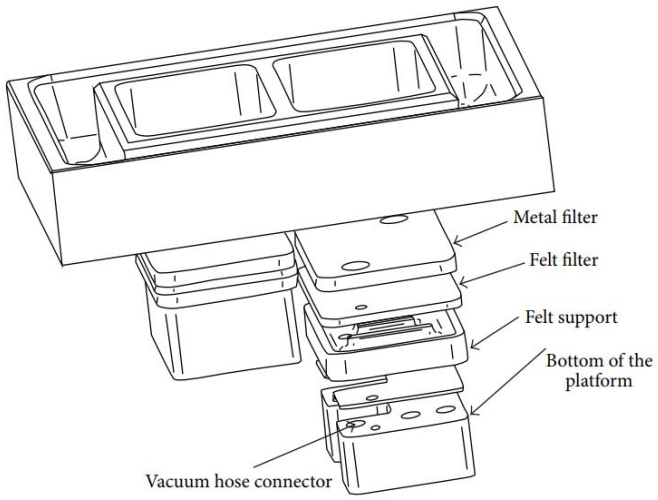

Figure 3.7: Assembly drawing of the vacuum 3D printer setup.

due to the gradient pressure generated by the vacuum pump (see fig. 3.8) . Beside the above-mentioned advantage of the no need for support structures, (past experiments have confirmed the feasibility to print successfully scaffolds without supports [50]), this method improves the flowability of the powder and its compaction. Indeed, the flowability mainly depends on two terms: the attractive interparticle force and the gravitational force (linked to the particle weight). Thus, it is useful to define a new ratio called *bond number,* ***BN***:

$$BN = \frac{F_{\mathrm{a}}}{m_{\mathrm{g}}} \tag{3.4}$$

where $\mathrm{F_a}$ is the attractive interparticle force and m_{g} the particle mass. The lower BN, the more flowable the powder and therefore the powder can pack well. A high interparticle force, typical of very fine powder, makes the deposition really difficult because the particles

tend to agglomerate and are not spread uniformly (in other words, the interparticles force is higher than the gravitational one). To conclude, by using a vacuum pump, the denominator of the BN increases since the pressure acts in the same direction of m_g; as a result, even smaller particles, which would be impossible to deal with otherwise can be printed.
The pump used is a high-performance rotary vane pump (Pfeiffer Vacuum, Duo 10 M): pumping speed: 10 m^3/h, powder (50 hz): 0.45 kW and ultimate pressure: $6{\cdot}10^{-3}$ hPa.

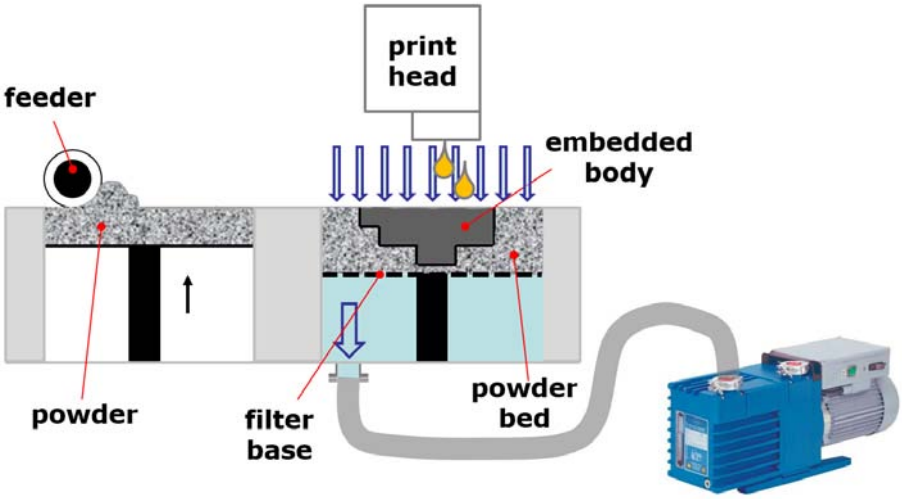

Figure 3.8: Stabilization of the build bed through a gas-flow (DE 10 2012 109 262.1 / WO 2014/049159 A1).

3.2.2 Stl files: tablets and scaffolds

In order to evaluate the material properties and the printing features, tablets of α-TCP have been printed. The STL file used is shown in fig. 3.9: the diameter measures 15 mm and the height 3 mm. With gas-flow the parts have been printed without support structure.
Moreover, more complex shapes have been printed in order to study both printing capability and sintering behaviour. The part chosen is a cube with designed porosity that simulates a scaffold as shown in fig. 3.10 and 3.11.

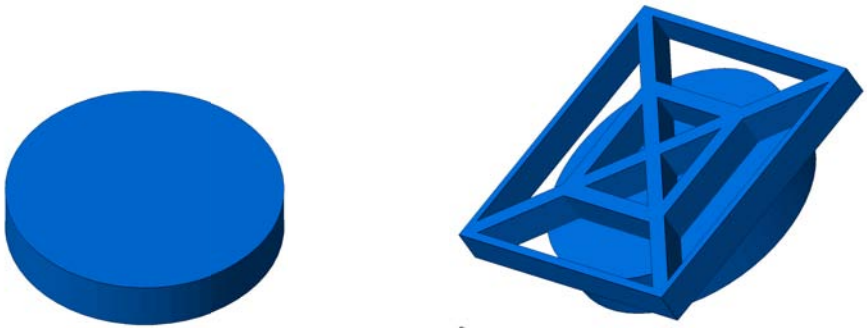

(a) Tablet printed without support.

(b) Tablet printed with support.

Figure 3.9: STL files used for printing tablets of α-TCP powder. Diameter of 15 mm and height of 3 mm.

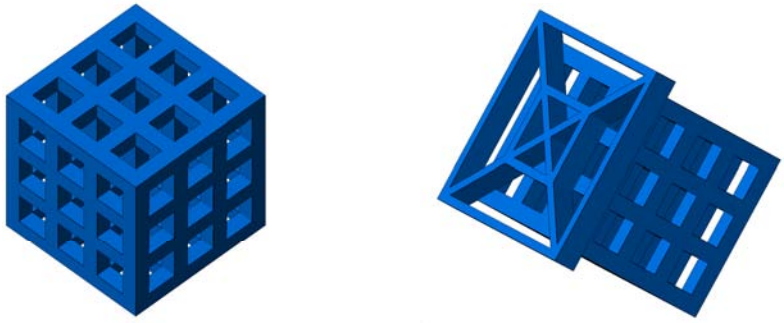

(a) Cube printed without support.

(b) cube printed with support.

Figure 3.10: STL files used for printing cubes of α-TCP powder.

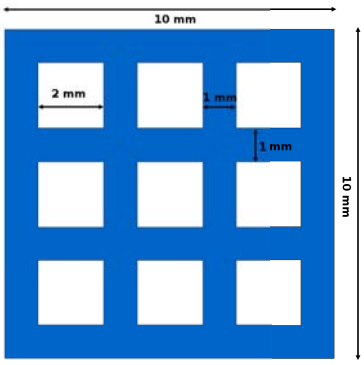

Figure 3.11: Geometrical features of the printed cube.

3.3 Sintering process

After printing the parts are kept overnight in the oven at 100 °C to make the binder dry and afterwards they are ready to be sintered. The sintering process is extremely important for the final properties: cracks, distortions, residual stresses and compaction are strongly affected by the temperature reached, the dwelling time and the heating-cooling rate. The

sintering program is shown in fig. 3.12 and the analysis will be focused on dwelling time and the cooling rate. The first step at 450 °C for 2 hours is meant to burnout the binder.

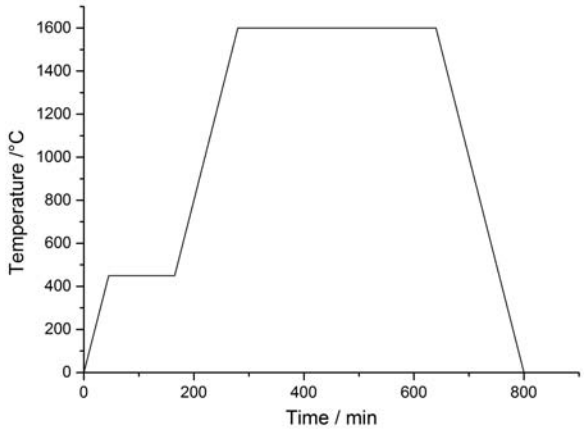

Figure 3.12: Sintering program for α-TCP. This work will focus especially on the cooling rate since cracks and distortions are likely to form in this step.

Gaseous products are eliminated and the dwelling time ensures a safe decomposition without the formation of cracks or fractures. Then, the sintering process occurs at 1600 °C for 6 hours. This high temperature and long time allow the particles to join together. Such a high temperature has been chosen since from previous studies the parts sintered at lower temperatures do not have enough stability due to the poor compaction.

It is important to remind some essential facts about sintering.
The driving force of the process is the reduction of the interfacial energy of the particles reducing the surface area associated with pores. A curved surface will always tend to be flat. More specifically, if we consider the particles as spheres, a curved surface presents a pressure difference between the inside and outside given by [52]:

$$\Delta P = \frac{2\gamma}{r} \tag{3.5}$$

where ΔP is the pressure difference, γ the surface free energy and r the radius of curvature of the sphere. r is positive when the center of radius is inside the material and negative when it is outside. Therefore, a negative pressure exists in concave surfaces. The result of this pressure difference is a decrease in free energy (ΔG) on the two sides of the boundary that causes the convergence to the center of curvature. This can be written as [52]:

$$\Delta G = \frac{2\gamma V}{r} \tag{3.6}$$

where V is the molar volume.

The reduction in free energy can be also thought as a decrease from a solid-gas surface (A_{sg}) of high energy (γ_{sg}) to a solid-solid surface area (A_{ss}) of low energy (γ_{ss}) [53]:

$$dG = dA_{ss}\gamma_{ss} + dA_{sg}\gamma_{sg} \tag{3.7}$$

where $dA_{sg}<0$ and $dA_{ss}>0$.
Small particles have a different behavior compared to the coarse ones because they have a large surface-to-volume ratio and a smaller radius of curvature. This promotes the formation of necks between particles and therefore the overall sintering rate increases. The necking mechanism is shown in fig. 3.13 [52]: the two centers of the particles must move toward one another and material will move toward the joint forming the neck. This results in a densification process decreasing the total porosity. The transport of matter

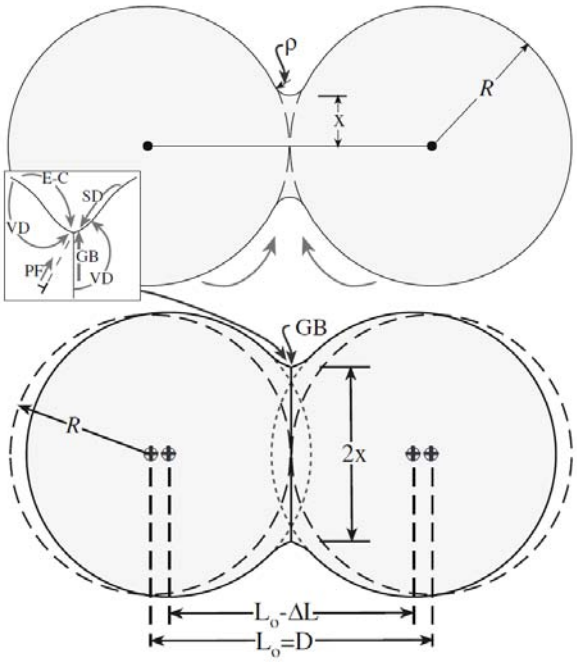

Figure 3.13: Necking formation and sintering. GB is the grain boundary, R the particle radius, L_0 the initial center distance, D is the diameter (considering identical spherical particles), x is half of the neck width and ρ is the neck radius.

toward the neck can occur via different ways:

- SD: surface diffusion: diffusion of atoms along the surface of the particle;
- VD: volume diffusion (via surface and grain boundaries);
- E-C: evaporation-condensation (via surface): evaporation of atoms that condense on a different surface;
- GB: grain boundaries diffusion: diffusion of atoms along the GBs;

- PF: plastic flow (via dislocations): dislocation movement causes flow matter.

Only the last two mechanisms along with the volume diffusion via GBs cause a densification of the part since the atoms move from the bulk to the surface of the pores reducing in this way the porosity. On the contrary, the other mechanisms only produce a re-arrangement of matter without reducing the pores size. The previous example has been made with two particles, but if the necking process is extended to more particles in a three dimensional perspective, pores might form among the necks of the particles. After the formation of the neck, the grains might grow depending on the sintering parameters. However, not all the grains survive: for energetical reasons a grain in contact with six other GBs has flat boundaries (angle of 120 °) an it is in a equilibrium state (see fig. 3.14 [52]). A grain among less than six GBs will shrink (the GBs concave inward) and might disappear during sintering. On the other hand, larger grains have more than six GBs (the GBs concave outward) and will grow. This growth is connected to the reduction of the grain-boundary energy and the energy decrease between fine and large grains.
Generally, the sintering process of powder is divided into three stages [53]:

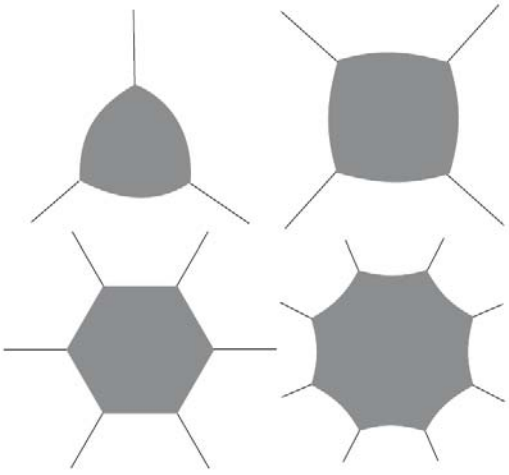

Figure 3.14: Angles and grains. Considering 2D grains, the equilibrium condition is when the grain is surrounded by other six GBs. Otherwise, the grain will shrink or grow depending if there are fewer or more than six GBs.

1. First stage: consolidation via superficial diffusion (low activation energy required) and formation and growth of the necks between particles: at the end of this step the compact may reach up to ∼65% of the theoretical density;

2. Intermediate stage: the shrinkage of the pores is the main densification mechanism: pores remain open and constitute a continuous phase until the end when they become isolated and the relative density reaches ∼90%. Due to the higher temperature, mechanisms like volume or boundaries diffusion are activated;

3. In the final stage the closed pores may disappear resulting in a nearly fully dense ceramic. If the amount of closed pores is very low, grain may grow remarkably since in the previous stages pores inhibited grain growth by pinning the grain boundaries. Therefore, grain growth occurs mainly during tha final stage of sintering.

3.4 Mechanical test: ball on three balls test

In order to give a brief explanation about one of the mechanical tests will be adopted, the main concept of the ball on three balls test have been outlined.
The ball on three balls test (B3B) is an important method to evaluate the mechanical strength of brittle materials. This is a biaxial tensile strength test therefore it provides a more severe and realistic failure scenario compared to the compressive test. The choice of this method stands on the fact that it has some advantages compared to the traditional procedures. For instance, ring on ring test or ball on ring test have the drawback that the specimen has to have parallel and smooth surfaces. Moreover, small geometric inaccuracies may strongly affect the results. On the other hand, in B3B test the edges, extremely difficult to prepare, have no influence on the results and the sample surfaces do not need to be perfectly parallel and smooth due to a very well defined load transfer. Therefore, even as-sintered specimens can be directly tested without any particular preparation [54, 55].
The setup is shown in fig. 3.15 [56]: the sample is centrally positioned on the loading ball which is placed on a stamp. Three supporting balls hold the sample fixed. Generally, all the balls have the same diameter. To carry out the test a preload is applied so that the balls can freely move and the sample is kept fixed between the loading ball and the other 3 balls. The stress state is depicted in fig. 3.16 [54, 57]: the maximum tensile stress is in

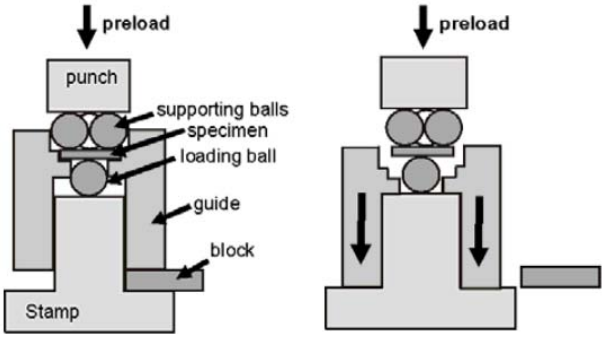

Figure 3.15: Setup used for the ball on three balls test. Preload step (*left*), removal of the block to lower the guide (*right*), the sample is ready to be tested.

the centre of the sample on the opposite side of the loading ball and it can be described as:

$$\sigma_{\max} = f \cdot \frac{F}{t^2} \tag{3.8}$$

where F is the maximum fracture load, t the thickness of the sample and f is a dimensionless factor that depends on the geometry of the specimen, the Poisson's ratio of the material and the radius of the supporting balls R_a. As it can be seen, the maximum stress is dependent on the applied force and indirectly proportional to the square of the disc thickness; thus, the diameter is one of the most relevant parameter for the determination of the strength.

The stress state has a threefold symmetry due to the three supporting balls (see fig. 3.16a) and that it may depend on a large number of geometrical and material parameters making the analytical approximation difficult. Generally, the fracture initiates in the tensile surface plane underneath the loading ball and the disc should break in three pieces according to the stress state.

To further understand how the stresses develop in the disc during the test, with reference

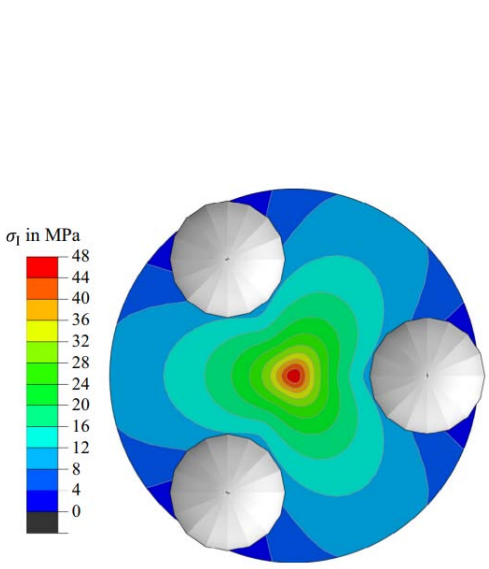

(a) Example of a stress field at the tensile side of the disc for a typical loading situation.

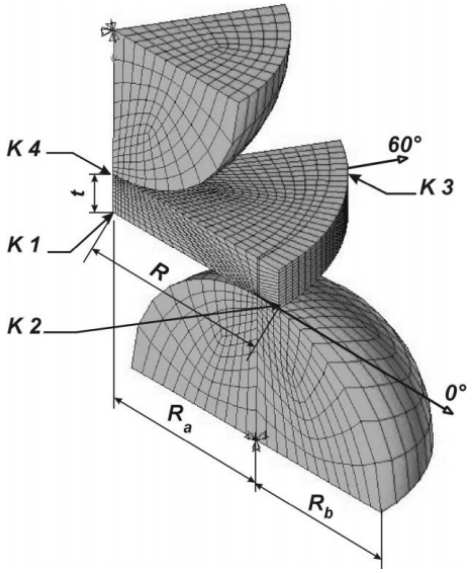

(b) FE-model of the ball on three balls test assembly: the midpoint of the support balls is fixed and the midpoint of the centred loading ball is only allowed to move vertically.

Figure 3.16: Biaxial strength state of the ball on three balls test for brittle materials.

to fig. 3.16b, fig. 3.17 shows the trend of the normalized radial, σ_{rr}, tangential, $\sigma_{\varphi\varphi}$, and axial, σ_{zz}, stresses in the 0°, 60° direction and along the axis of the disc [54]. In the 0° direction, σ_{rr} and $\sigma_{\varphi\varphi}$ are almost similar and tend to an asymmetrical biaxial stress state at the midpoint. The axial stress instead is around zero since the surface is free. In the contact area, between the support ball and the disc, there are compressive stresses as high as the maximum tensile strength. The smaller the balls, the higher these values which may be greater than $\sigma_{\max}$ therefore small ball are to be avoided for the scope of this

test. In the 60° direction, the tangential stress component is higher than the radial stress except at the centre where they tend to be equal. σ_{zz} is almost zero in the 60° direction. Lastly, along the vertical axis of the disc, the tangential and radial stress are the same. It is interesting to point out that the absolute value of the compressive stress underneath the loading ball is several times higher than the amplitude of the tensile stresses in the centre of the tensile surface.

Having said that, it is clear that compared to the compressive test, the stress state is more complex and dangerous. The tensile component has a great effect on the sample especially if there are some cracks that can grow very easily causing a fast break.

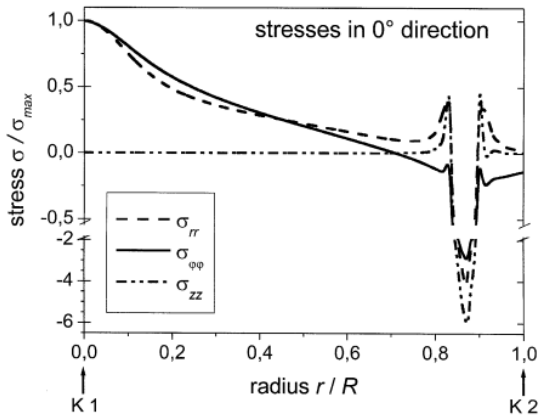

(a) Radial, tangential, axial normalized stress component along a path in the 0° direction (K1-K2).

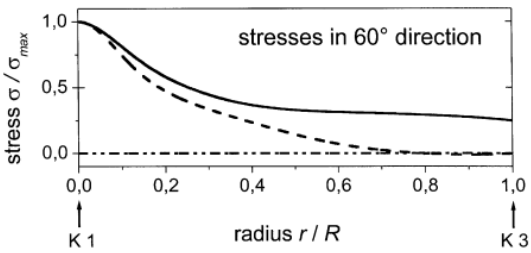

(b) Radial, tangential, axial normalized stress component along a path in the 60° direction (K1-K3).

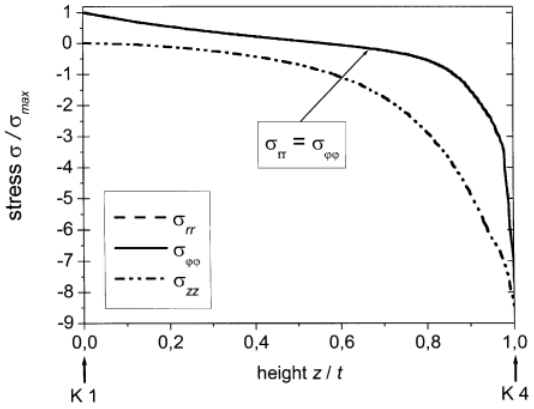

(c) Radial, tangential, axial normalized stress component along the axis (K1-K4).

Figure 3.17: Biaxial stress field of a disc subjected to the ball on three balls test (with reference to fig. 3.16b).

3.5 Final remarks

In this chapter, the main procedures employed to synthesize, print and test the powder have been reported. The synthesis route chosen (3.1) consists of mixing H_3PO_4 and $CaCO_3$ to obtain the precursor $Ca_8H_2(PO_4)_6 \cdot 5\,H_2O$ (OCP). After a 3 step-treatment, this precursor turns into β-TCP that transforms into α at temperatures higher than 1150 °C. After milling and sieving, the powder is ready to be printed. All the main parameters of the 3D printing have been discussed in section 3.2: particle size, layer thickness, Hausner ratio, powder packing rate, powder bed density, spread speed, feed to layer thickness ratio and the binder properties. Moreover, the powder bed can be stabilized through a gas flow: this allows to make the powder more compact and stable. As a result, supports structure may be avoided and even finer powder can be printed despite the low flowability. This method greatly affects the porosity, density and mechanical properties of the printed part and its outcomes will be introduced in the next chapter.
The files used to print are introduced in section 3.2.2. To conclude, in section 3.3 and 3.4 the main concepts of the sintering process and the ball on three balls test have been outlined to better understand the following results.

Chapter 4

Results and discussion

In this chapter, all the experimental results are reported. Five sections can be distinguished: the first section (4.1) deals with the characterization of the powder; then sections 4.2 and 4.3 illustrate all the features about the 3D printing and the sintering program. The core of this thesis is included in sections 4.4 and 4.5 where all the results and achievements of the printed tablets and scaffolds are covered.

4.1 α-TCP powder

In this section, all the analyses to evaluate the properties of the α-TCP powder are presented. The thermal behaviour is explained in section 4.1.1 with DTA, hot stage microscopy and dilatometry. XRD analyses and infrared spectroscopy are covered in setions 4.1.2 and 4.1.3 respectively. Lastly, elemental analyses are outlined in section 4.1.4.

4.1.1 Thermal analyses: hot stage microscopy, dilatometry and DTA

In order to evaluate the thermal behaviour of the synthetized α-TCP powder, hot stage microscopy, dilatometry and differential thermal analysis have been used. The aim of these investigations is to understand at which temperature the phase transition β to α-TCP occurs, the sintering onset, the different behaviour between the fine and coarse particles and therefore the sintering process.

Fig. 4.1 shows a preliminary analysis of the powder obtained after the first treatment (see fig. 3.1). The heating rate is 50 °C/min and two cooling rates are used: 30 and 5 °C/min to check if the reverse transformation α to β occurs especially with low cooling rates: this would indicate the presence of impurities that stabilize the low temperature phase. The

sample is held at 1513 °C (max temperature of the device) for 2 h in order to stabilize the phase and have a closer result to the sintering process. Over heating, thermal expansion occurs until the phase transformation β to α-TCP at around 1150 °C (green vertical line) with an sudden area expansion. The sintering onset starts at about at 1300 °C (blue vertical line). During the dwelling, denoted by the vertical drop, the samples show an area reduction of ∼20 % and with the faster cooling rate the final shrinkage is ∼ 4% greater. Over cooling, there is none transformation indicating that at the end α-TCP is stable at room temperature with an area reduction of 18% and 22% for the slow and fast cooling rate respectively.

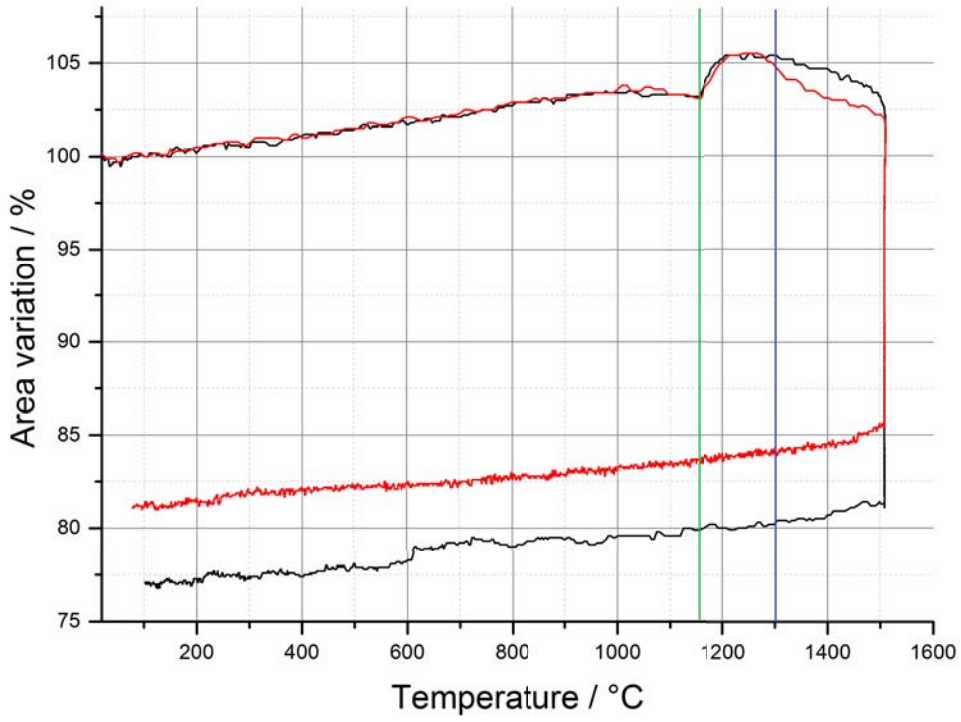

Figure 4.1: HSM of almost-one-phase β-TCP after the first treatment. Heating rate of 50 °C/min, dwelling time of 2 h at 1513 °C, cooling rate of 30 °C/min (black line) and 5 °C/min (red line). The green and blue vertical lines correspond to the β-to-α transformation and the sintering onset.

To further investigate the cooling behaviour, a slower cooling rate has been chosen (1 °C/min): such a slow rate is used only to check the reverse transformation since this would never be a practical choice for economical reasons. The heating rate is 20 °C/min to have a more feasible ramp compared to the previous graph. The measurement is depicted in fig. 4.2a. Over heating, it is interesting to note that in this case the sintering onset (at around 985 °C, blue vertical line) happens before the transformation phase (at 1176 °C, green vertical line). Therefore, while the sintering onset occurs at around 1300 °C for 50 °C/min and at 985 °C for 20 °C/min, the phase transformation changes

only of $\sim 26\,^{\circ}\mathrm{C}$. This can be explained by the fact the sintering process is strongly time dependent: since it involves diffusion mechanism, matter has to gain a certain energy to be able to move forming the necks first and then starts to shrink.
Moreover, during cooling none reverse transformation occurs meaning that α-TCP is very stable and more energy (and time) is required to turn into β-TCP. Overall, the area reduction is 30%, 10% more than the measurement done with $50\,^{\circ}\mathrm{C}/\mathrm{min}$. To check the results achieved with the hot stage microscopy, the same heating conditions of fig. 4.2a have been used (see fig. 4.2b). Moreover, to confirm the previous outcomes cooling rates of 5 and $10\,^{\circ}\mathrm{C}/\mathrm{min}$ have been adopted. The test proved that the sintering onset (at around $954\,^{\circ}\mathrm{C}$) occurs before the transformation phase (at around $1164\,^{\circ}\mathrm{C}$) with a heating rate of $20\,^{\circ}\mathrm{C}/\mathrm{min}$. Again, during cooling the reverse transformation does not occur.

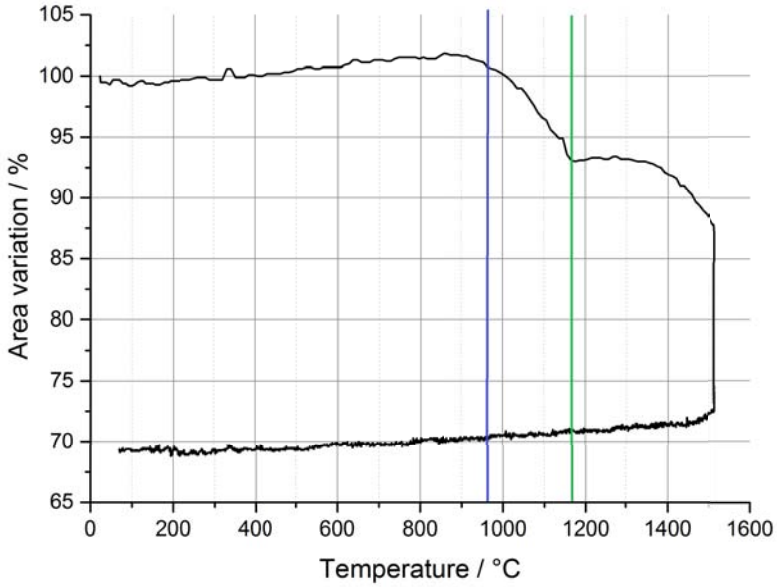

(a) HSM of almost-one-phase β-TCP after the first treatment. Heating rate of 20 °C/min, dwelling time of 2 h at 1513 °C, cooling rate of 1 °C/min.

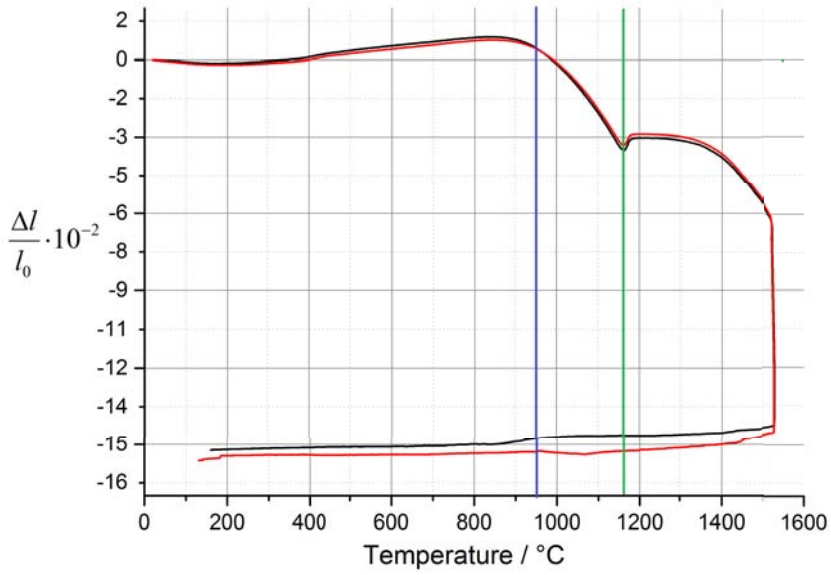

(b) Dilatometry of almost-one-phase β-TCP after the first treatment. Heating rate of 20 °C/min, dwelling time of 2 h at 1550 °C, cooling rate of 5 and 10 °C/min (red and black line). Load: 2.5 kPa.

Figure 4.2: HSM and dilatometry of almost-one-phase β-TCP after the first treatment. The blue and green vertical lines correspond to the sintering onset and the β-to-α transformation.

Lastly, to have a preliminary idea of the sintering behaviour of the two particles sizes of

α-TCP (after the second treatment) another measurement with the HSM has been carried out. From fig. 4.3 it is clear that the fine powder has a promoted sintering behaviour: the rate of densification is faster for small particles. Indeed, the sintering onset is around 1050 and 1300 °C for the fine and coarse powder respectively (orange and brown vertical lines) and at the end of the test the area decrease in the fine powder is 30% compared to only 10% of the coarse powder.

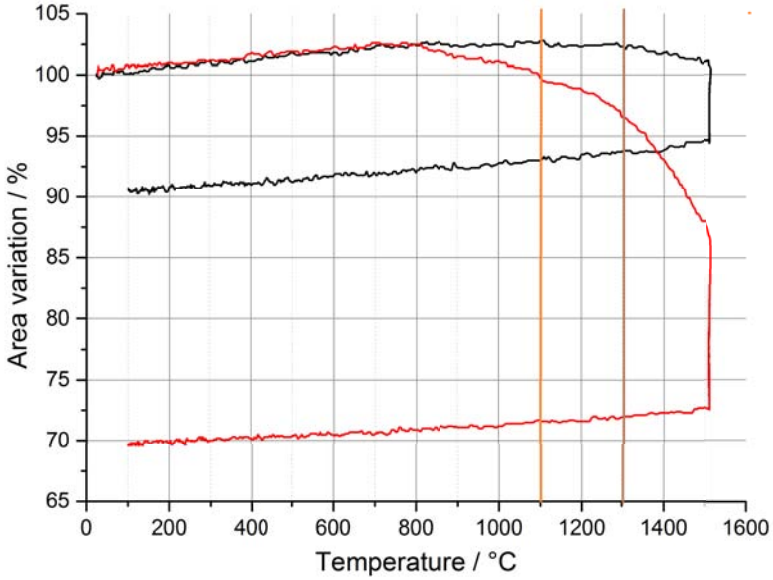

Figure 4.3: HSM of the fine and coarse powder of α-TCP (after the second treatment). The red and black lines are the fine and coarse powder respectively. Heating rate of 50 °C/min, dwelling time of 2 h at 1513 °C, cooling rate of 35 °C/min. The orange and brown vertical lines correspond to the sintering onsets.

Additionally, DTA measurements have been carried out to better understand the thermal behaviour of the two particles sizes of α-TCP. In all the following DTA graphs the large 'hump' of the heating curve is only an artifact of the machine that it has been used for many years. In fig. 4.4 the analysis of the coarse powder is showed. The only parameter changed in the two plots is the cooling rate: 5 °C/min in 4.4a and 10 °C/min 4.4b. The main transformation is from α to α' TCP at around 1464 °C visible from the endothermic peak during heating. There is not significant difference between the coolings: with the faster rate the reverse transformation is slightly retarded by some degrees and the peak is a bit higher. No other transformation occurs. Regarding the mass variation, there is nothing important to note since the phase transformation occurs without mass change. Anyway, the mass decrease is lower than 1%.

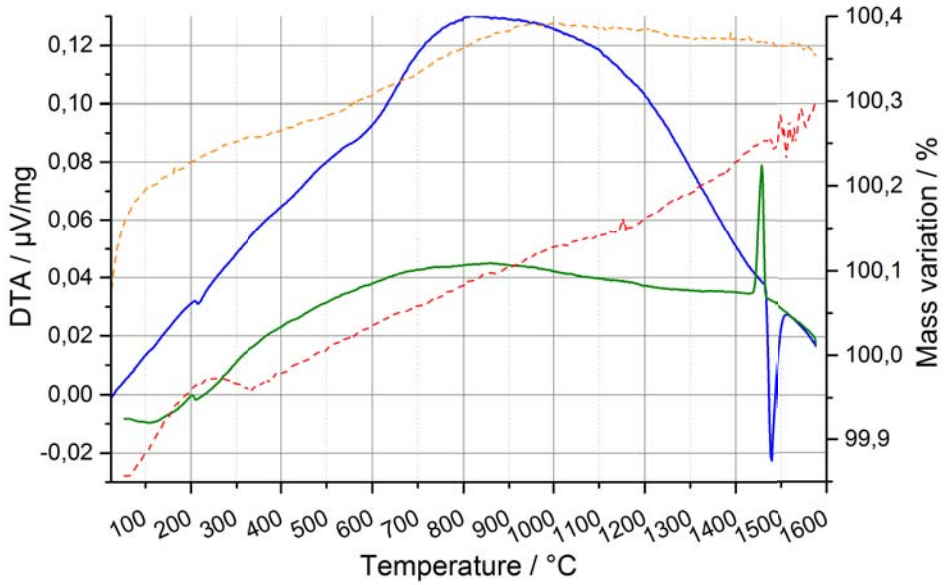

(a) DTA and TG of the coarse powder with a cooling rate of 5 °C/min.

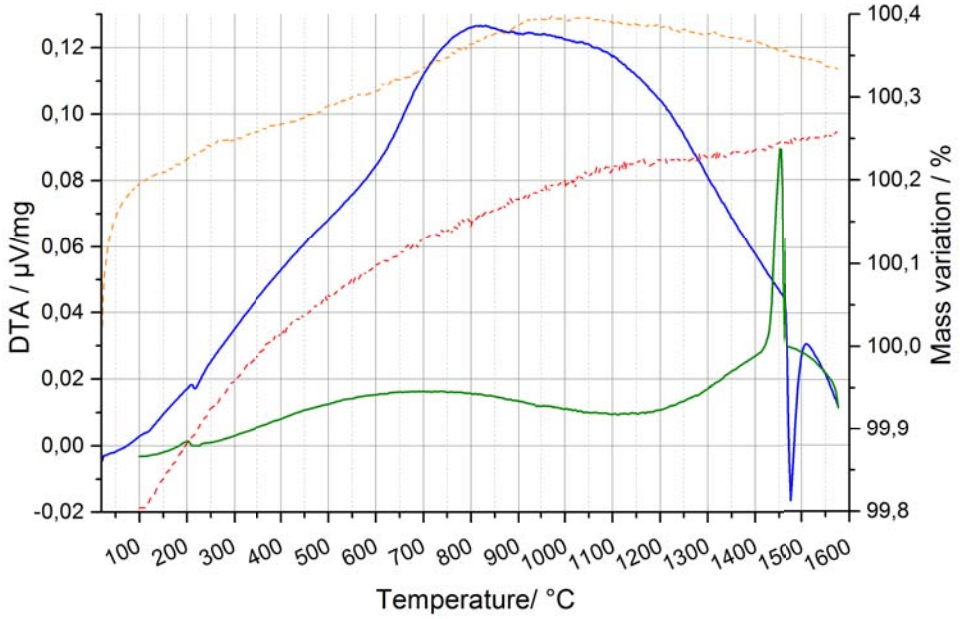

(b) DTA and TG of the coarse powder with a cooling rate of 10 °C/min.

Figure 4.4: DTA-TG of the coarse α-TCP powder. Heating rate of 10 °C/min, dwelling time of 20 minutes at 1570 °C and cooling rate of 5 °C/min (a) and 10 °C/min (b). Blue line: DTA heating, green line: DTA cooling, orange line: TG heating, red line: TG cooling. Upward peaks are exothermic, downward peaks are endothermic.

Same measurements have been carried out for the fine powder (see fig. 4.5). The graphs show no particular difference and the transformation from α to α' TCP occurs at the same temperature.

Lastly, to double check the previous results of the hot stage microscopy at 1 °C /min as

a cooling rate, the same DTA test has been done: it confirms that both particles sizes of α-TCP do not show the reverse transformation to β when cooled at 1 °C /min.

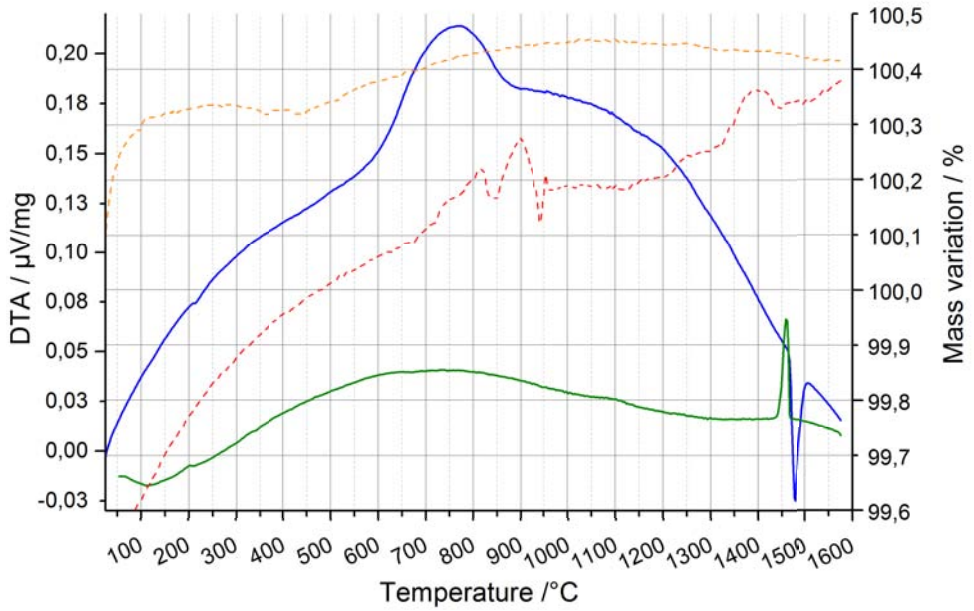

(a) DTA and TG of the fine powder with a cooling rate of 5 °C/min.

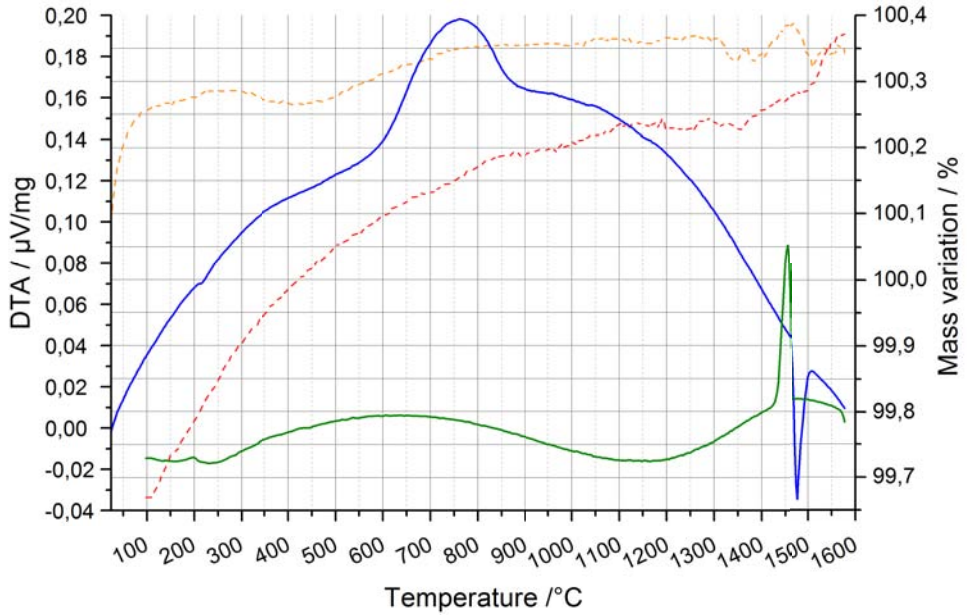

(b) DTA and TG of the fine powder with a cooling rate of 10 °C/min.

Figure 4.5: DTA-TG of the fine α-TCP powder. Heating rate of 10 °C/min, dwelling time of 20 minutes at 1570 °C and cooling rate of 5 °C/min (a) and 10 °C/min (b). Blue line: DTA heating, green line: DTA cooling, orange line: TG heating, red line: TG cooling. Upward peaks are exothermic, downward peaks are endothermic.

4.1.2 Phase analysis: X-ray diffraction

The XRD results of the powder after the first treatment (3.1), indicate a deviation from pure β-TCP indeed there are HA (2±2%) and β-$Ca_2P_2O_7$ (9±2%) (all the XRD results are in wt. %). HA may form during the reaction of $Ca_8H_2(PO_4)_6$ besides γ-$Ca_2P_2O_7$ as follows:

$$2\,Ca_8H_2(PO_4)_6 \xrightarrow{400} 3\,\gamma\text{-}Ca_2P_2O_7 + Ca_{10}(PO_4)_6(OH)_2 \qquad 9$$

HA may form also from CaO and TCP as follows:

$$CaO + 3\,Ca_3(PO_4)_2 + H_2O \xrightarrow{1000} Ca_{10}(PO_4)_6(OH)_2 \qquad 10$$

Moreover, due to a little excess of H_3PO_4 (by experimental mistake), the reaction between CaO and β-$Ca_2P_2O_7$ is not completed and some β-$Ca_2P_2O_7$ remains unreacted. As it can be seen, it is extremely difficult to predict the mechanisms of formation of β-TCP and for a clear and definitive conclusion more kinetic investigations must be carried out.
After the second treatment at 1600 °C the qualitative and quantitative X-ray analyses of the seven batches produced indicate that the major phase is α-TCP with a low percentage of HA (see fig. 4.6 for the qualitative analysis of the seven batches). By the Rietveld method, most of the batches reveals contents of HA lower than 4±2% while two have around 20±2% due to a little excess of H_3PO_4 poured into the bowl containing $CaCO_3$. This means that the amount of the two compounds should be extremely precise in order to obtain a Ca/P ratio of 1.5 (that is, pure TCP). Overall, after mixing, the total powder is 93±2% α-TCP and 7±2% HA. However, the procedure chosen is a valid route to get only one phase as fig. 4.7 depicts: the qualitative analysis proves 100% α-TCP for the batch number 7.
The importance of the purity of the material is connected to the biological applications of the future implant. For β-TCP, the ASTM F1088 claims that the minimum content of β must be 95% but there is no such a standard for the biomedical grade α-TCP. Nevertheless, the same value used for β can be adopted. Having said that, the synthesis route used is a promising method to achieve one single phase (apart from human errors). Besides, by slightly modifying the initial composition, different degree of purity can be achieved.
In the end, the α-TCP produced has around 3±2% more of HA according to the standard, but during sintering the requirement can be easily reached.

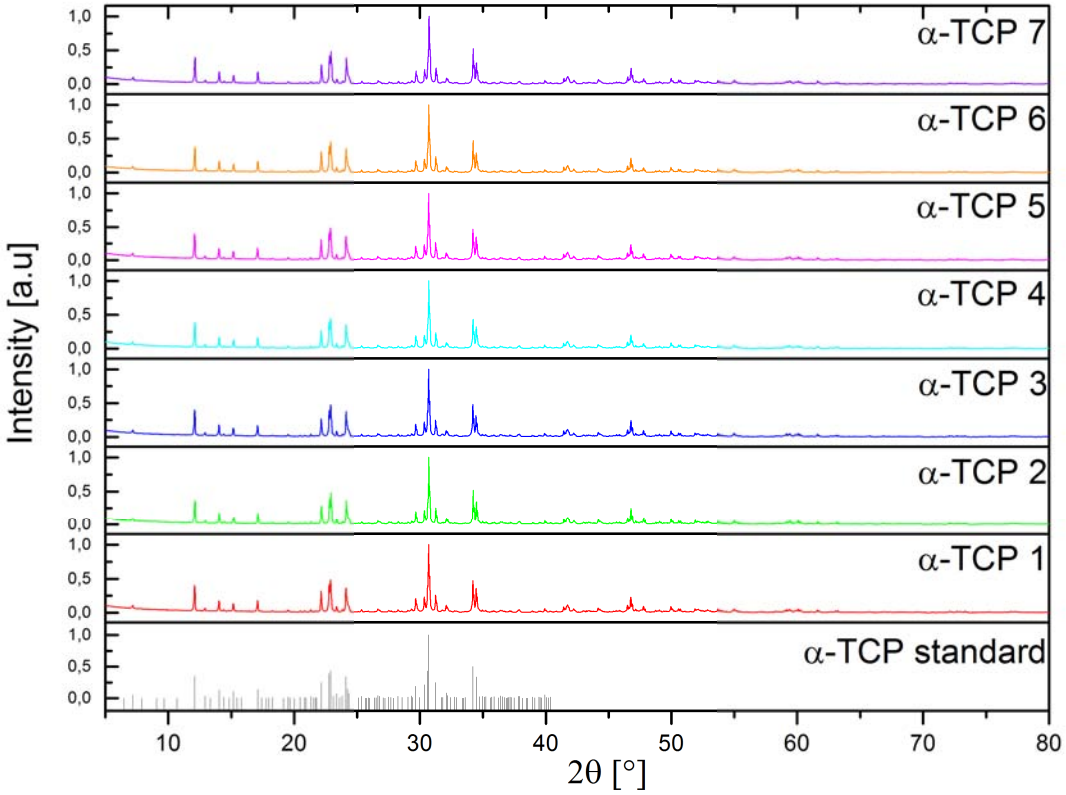

Figure 4.6: Normalized XRD patterns of the seven batches of the synthetized α-TCP powder (with the standard reference).

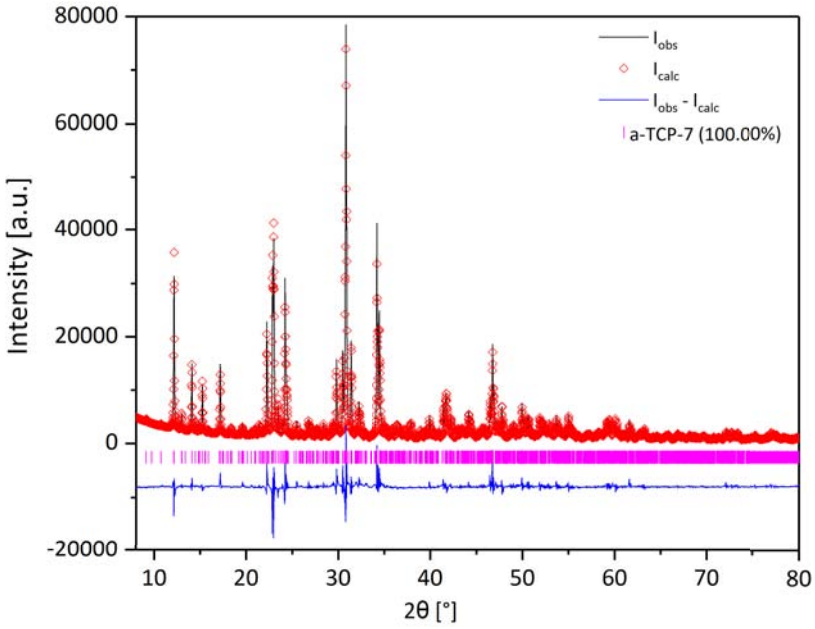

Figure 4.7: XRD quantitative analysis of the best batch of the synthetized α-TCP powder. The amount of α-TCP calculated by the Rietveld method is 100%.

4.1.3 ATR spectroscopy

To have a further confirmation of the structure of the α-TCP produced, an attenuated total reflection spectroscopy (ATR) has been carried out. The spectrum of the powder analysed is shown in fig. 4.8a; most of the peaks match the bands of α-TCP and HA. Peaks around 2900 cm^{-1}, 2300 cm^{-1} and 1600 cm^{-1} represent the vibrational modes of organic compounds (C-H), CO_2 and H_2O in air respectively. These peaks may be avoided if the sample chamber is under controlled conditions such as in vacuum or with N_2 atmosphere. Besides, the peaks on the far right are caused by the detection limit of the machine due to the low intensity energy of the beam. On the other hand, with regard to the α-TCP bands, a deeper investigation is outlined below.

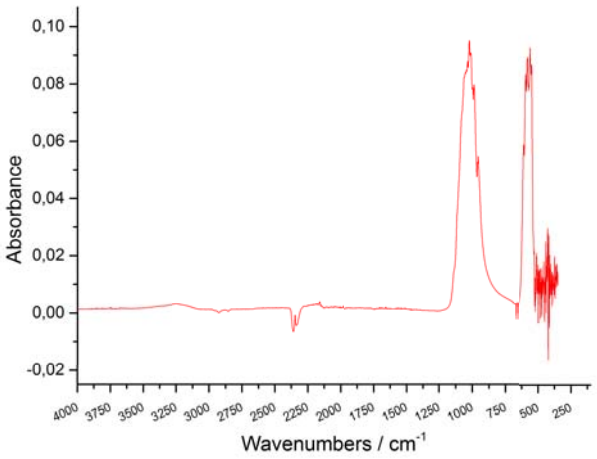

(a) Overall ATR spectrum of the synthesized α-TCP powder.

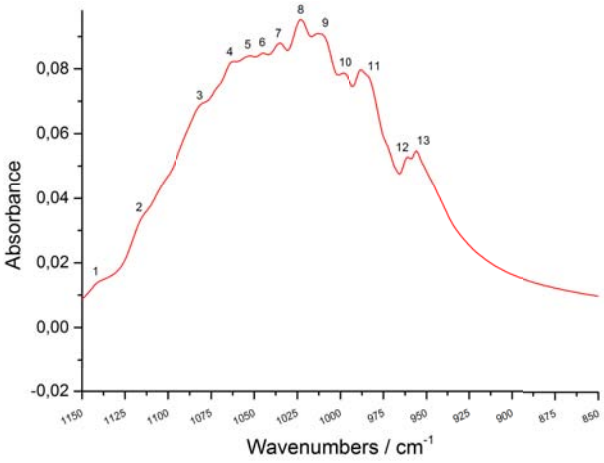

(b) Zoom of the first peak.

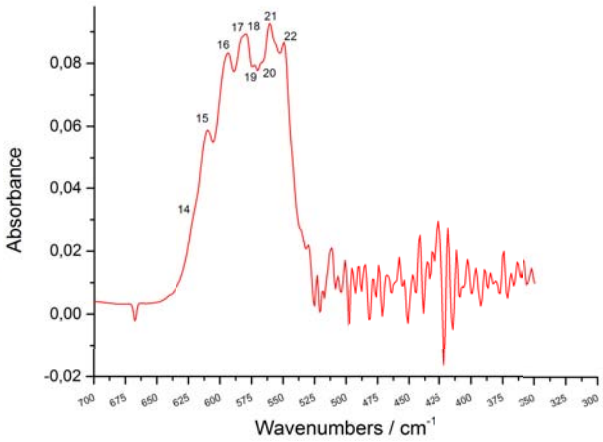

(c) Zoom of the second peak.

Figure 4.8: ATR spectra of the synthesized α-TCP powder. The ATR crystal used is diamond.

Fig. 4.8b and 4.8c are enlargements of the high and low energy peak respectively. The

numbers in the spectra represent the molecular vibrations of the phosphate group (mainly stretching and bending) and the individual bands are reported in table 4.1.
This technique, along with the results of the XRD, proves the presence of α-TCP and HA as thought. However, qualitative measurements are extremely difficult due to the variability of the atmospheric conditions (humidity in the air and in the sample, CO_2, organic compounds) and sample preparation. Moreover, some peaks have not been found: bands at 987 cm^{-1}, 667 cm^{-1} and 535 cm^{-1} need a more advanced research.

Table 4.1: ATR absorption bands of α-TCP powder.

Number	Material reference	Wavenumber (cm^{-1})	Source
1	HA	1140	[58]
2	α-TCP	1115	[59]
3	α-TCP	1080	[59]
4	α-TCP	1062	[59]
5	α-TCP	1052	[59]
6	HA	1044	[58, 60, 61, 62, 63]
7	α-TCP	1034	[59]
8	α-TCP	1023	[59]
9	α-TCP	1012	[59]
10	α-TCP	997	[59]
11	α-TCP	983	[59]
12	HA	960	[58, 62, 64]
13	α-TCP	955	[59]
14	α-TCP	620	[59]
15	α-TCP	609	[59]
16	α-TCP	593	[59]
17	α-TCP	582	[59]
18	HA	578	[63]
19	HA	571	[61, 63, 64]
20	HA	567	[58, 63]
21	α-TCP	560	[59]
22	α-TCP	549	[59]

4.1.4 Elemental analysis: ICP-OES and X-ray fluorescence

The ICP-OES (inductively coupled plasma atomic emission spectroscopy) elemental analysis of α-TCP for the fine and coarse powder is shown in table 4.2. As already mentioned, unlike β-TCP, there is not a standard for the medical grade of α-TCP, therefore it seemed reasonable to use the same ions concentration limits reported in the ASTM international F1088 for β-TCP:

- maximum concentration of As: 3 mg/L

- maximum concentration of Cd: 5 mg/L
- maximum concentration of Hg: 5 mg/L
- maximum concentration of Pb: 30 mg/L

The measurements reveal that no traces of Hg, Pb, As and Cd are found in the powder or that their concentration is lower than the detection limit therefore in any case the α-TCP powder synthetized fulfills the requirements according to the medical grade standard of β-TCP.
From this analysis the Ca/P ratio can be easily obtained to better understand the phase purity of the powder. The Ca/P ratio is 1.53 and 1.55 for the fine and coarse powder respectively: this confirmed that the powder is almost pure TCP and in the phase diagram (fig. 2.5) it corresponds to a composition slightly shifted on the right from the vertical line of TCP (around 55 wt% of CaO).
The Ca/P ratio strictly affects the sintering process: it has been shown that a Ca-rich TCP (Ca/P>1.5) has a lower shrinkage rate compared to a Ca-deficient [65]. This can be partially explained due to the fact that the latter forms a liquid phase at 1288 °C while the Ca-rich at a higher temperature (1578 °C). This means that Ca-deficient TCP densifies assisted by a liquid phase at relatively low temperature (1300 °C) while the Ca-rich TCP can be sintered only in a solid state since the viscosity of the liquid phase that may form at around 1600 °C is much lower and it may threatens the shape-retention capacity of the sintered part. Moreover, due to the presence of the liquid phase, grain growth is more evident in Ca-deficient.

Table 4.2: ICP-OES analysis of the fine and coarse α-TCP powder. The values are the average of six measurements for both particle sizes. The percentages represent the comparison with the theoretical content of Ca and PO_4 in TCP, that is, 193.55 and 306.45 mg/L respectively.

Ion	Detection limit	α-TCP (<25 μm)	α-TCP (45<X<100 μm)
As (mg/L)	0.20	0.00	0.00
Cd (mg/L)	0.01	0.00	0.00
Hg (mg/L)	0.03	0.00	0.00
Pb (mg/L)	0.04	0.00	0.00
Ca (mg/L)		193.37 (99.9%)	195.35 (100.9%)
PO_4 (mg/L)		298.25 (97.3%)	294.50 (96.1%)

Further confirmations of the composition of the powder have been obtain from XRF (X-rays fluorescence) analyses whose results are shown in 4.3. Overall, the test revealed that the concentration of impurities is very low. The presence of ions such as Mg, Sr and Zr is almost negligible therefore these ions do not influence the stability of the two phases

(these ions stabilize β-TCP). Also the amount of Si is very low thus neither this affects the thermal stability of TCP (Si stabilizes α-TCP).

Table 4.3: XRF analysis of α-TCP powder. The powder was compacted into tablets and the measurement was carried out in vacuum.

Element	Amount (wt.%)
C	0.94
N	0.14
O	40.58
Mg	0.06
Al	0.00
Si	0.23
P	16.69
S	0.00
Cl	0.01
Ca	41.21
Cu	0.00
Sr	0.01
Zr	0.12

4.2 3D printing

In this section, practical considerations and evaluations about the printing are reported. Printing parameters to obtain a uniform powder deposition are discussed in section 4.2.1 while in 4.2.2 the parts printed are shown.
Two particles sizes have been used: fine (lower than 25 μm) and coarse (between 45 and 100 μm) powder. Moreover, the printing process through the stabilization of the powder bed through a gas flow will be covered.

4.2.1 Powder deposition

Before printing, it is essential to find the optimal parameters to achieve a uniform, smooth and regular powder layer after the spread. To do that, layer thickness (LT), build and feed speed and feed to layer thickness (FLT) ratio have been varied for the four typologies: coarse powder printed with and without gas flow and fine powder printed with and without gas flow. The maximum values of the printer are 50 mm/s for the spread speed and 3 for the FLT ratio.
Here some general considerations are reported:

- A higher speed of the bed and LT result in a reduction in the process time. However, an high spread speed may affect the stability of the part (like lateral shift) during

the printing and an increase in LT may reduce the mechanical properties;

- A higher FLT ratio requires an greater amount of powder to be collocated in the feed bed and therefore more powder is 'wasted' during the printing (even though it can be reused after being sieved). On the other hand, a low FLT ratio may cause a non uniform spread since there is not enough powder to cover all the build bed;

- Especially with the fine powder, on the roller, a sponge brush has been used in order to keep the roller clean from particles. As already mentioned, fine particles have a higher surface energy therefore they tend to get stuck in the roller. This may cause a ripple effect so more particles join the other particles already 'glued' to the roller. Consequently, these agglomerations on the roller results in marks on the powder bed. Depending on the speed, particles are not attached to the roller, but following its rotation they are 'thrown' on the side of the bed just flattened (see fig. 4.9). Thus, the powder bed is not homogeneous. With the brush, all these problems are avoided.

- It is important to note that not only the build bed has to be uniform, but also the feed bed. The reason is that if there are some agglomerations anywhere in the bed, while the print-head is jetting the binder, it may collect these agglomerations more and more and the bed is ruined after some layers.

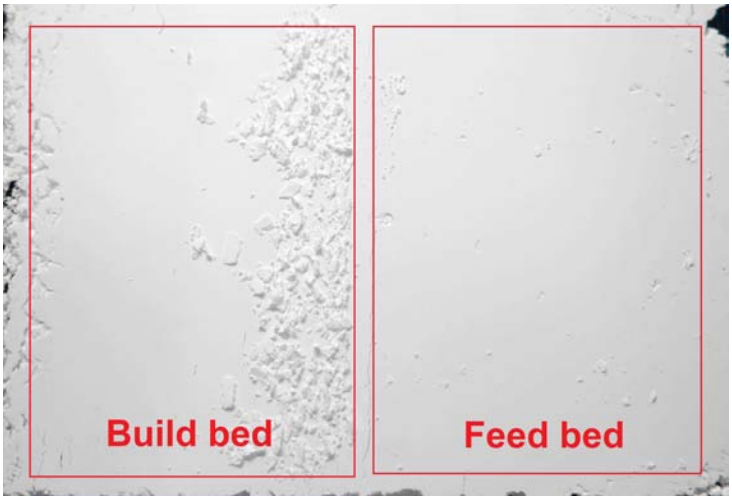

Figure 4.9: Powder bed deposition of the fine α-TCP powder without brush. The left side of the powder bed is the build bed while the right side is the feed bed.

For simplicity, in the following paragraphs and images the next abbreviation is used for the printing parameters: *a-b-c-d* where *a* is the build speed, *b* the feed speed, *c* is the FLT and *d* is the LT. For instance, 10-20-3-100 means a build speed (in the build bed) of 10 mm/s, a feed speed (in the feed bed) of 20 mm/s, 3 is the feed to layer thickness

ratio and the layer thickness is 100 μm.

Starting from the coarse powder without gas, the deposition is uniform and smooth with a wide range of parameters: the LT chosen is 105 μm that is slightly more than d_{90}; with a FLT ratio of 2 all the build bed is well covered and speeds from 5 to 50 mm/s result in little differences. As long as the feed bed is homogeneous, the feed speed can be much higher than the build speed to save time. Four different speeds have been tested as shown in fig. 4.10: from the images it is difficult to notice any dissimilarity indeed the variation is almost negligible. In conclusion the final parameters used are: LT=105 μm, FLT ratio=2, build speed=10mm/s, feed speed 40mm/s.

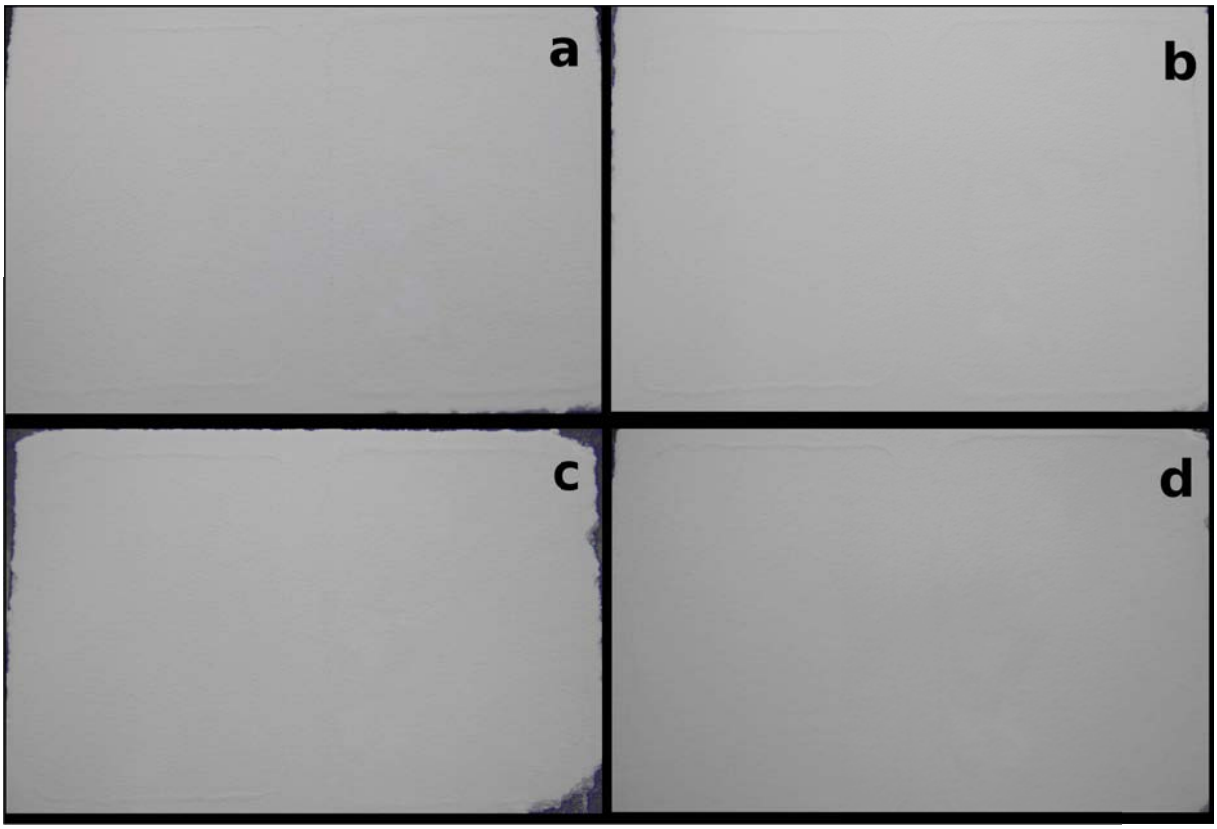

Figure 4.10: Powder bed deposition of the coarse α-TCP powder after 15 layers without gas flow. a) 5-40-2-105, b) 10-40-2-105, c) 20-50-2-105, d) 40-40-2-105. The left side of the powder bed is the build bed while the right side is the feed bed.

With regard to the coarse powder with gas flow, the LT is kept the same and the feed speed chosen is 50 mm/s. The FLT ratio used is 2.5 since with a lower value the powder is not uniformly deposited in the two corners of the bed. This is due to the pressure of the gas that hold a greater amount of powder in the bed compared to the deposition without gas flow. Build speeds from 2 to 50 do not show strong differences and result in a good deposition: with 50 mm/s the bed seems a bit more homogeneous so this speed is chosen

(see fig. 4.11). Since the tablet is only 3 mm high the effect on the stability of the part due to such a high build speed are negligible.
Regarding the surface finish, the effect of the metal filter results in a slight texture on the surface. This may due to preferential air channels in the powder bed caused by the filter and its porosity.
It can been seen that with the coarse powder more parameters can be selected successfully since the wide particle size distribution enhances the flowability of the particles [48].

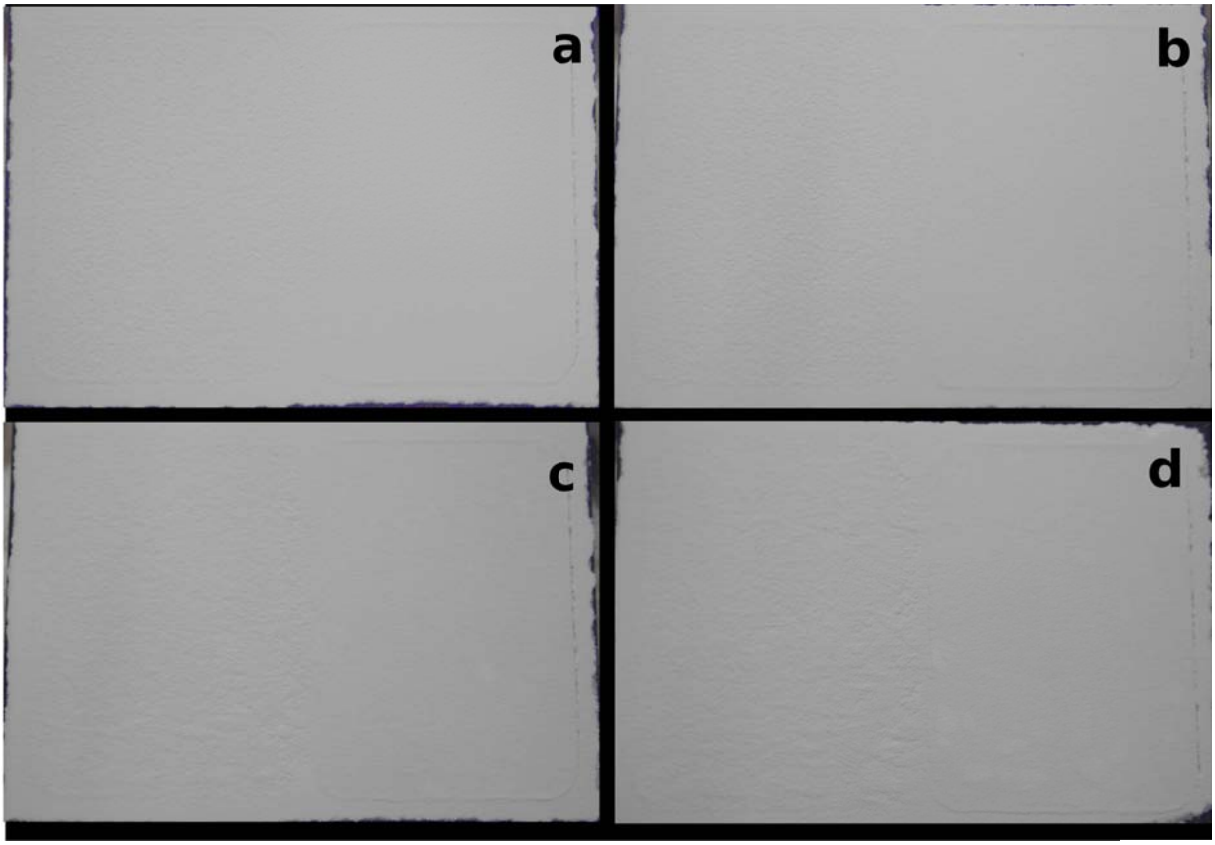

Figure 4.11: Powder bed deposition of the coarse α-TCP powder after 15 layers with gas flow. a) 5-50-2.5-105, b) 10-50-2.5-105, c) 50-50-2.5-105, d) 70-50-2.5-105. The left side of the powder bed is the build bed while the right side is the feed bed.

The deposition of the fine powder is more complex. The main outcome is that it is unfeasible to spread the fine powder without the stabilization of the powder bed by the gas flow due to the difficulty to obtain a uniform deposition (as shown in fig. 4.12). The variation of the FLT ratio does not help particularly: for a low value (2) the powder does not cover uniformly the last part of bed while with 3 the powder starts to agglomerate in front of the roller without being deposited. Similar effect happens with a low speed (lower than 10 mm/s): the particles have more time to aggregate in front of the roller and so they are not spread but only push forward. Indeed, a stable "cylinder of powder" forms in front of the roller towards the spread direction. With a higher build speed

(higher than 50 mm/s), the result is better since the roller acts more like a blade. Even so, the powder bed is not homogeneous enough to be printed. Also the variation of the LT does not affect significantly the outcomes: from 30 to 120 μm the powder is not spread properly. In conclusion, from this work, particles with d_{50} lower than 9 μm are impossible to be printed without the stabilization of the bed by a vacuum pump.

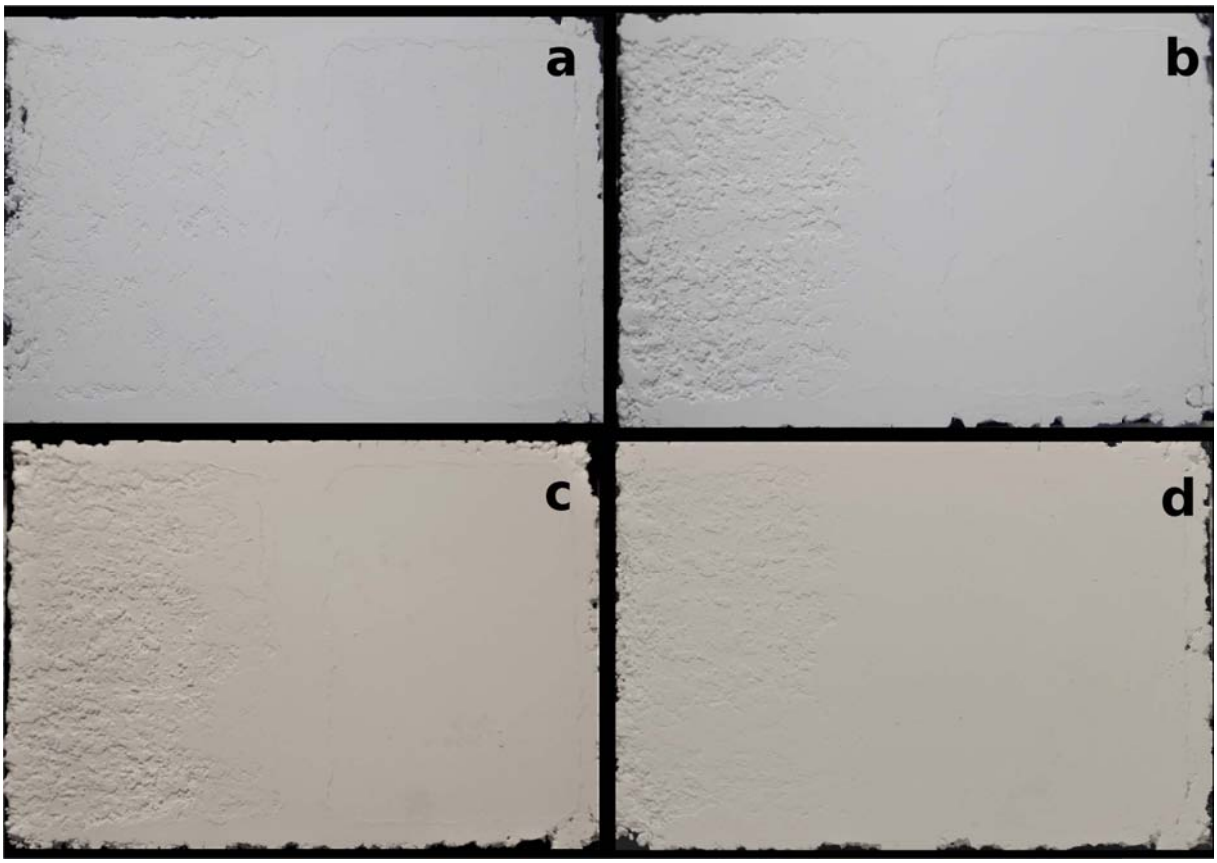

Figure 4.12: Powder bed deposition of the fine α-TCP powder after 15 layers without gas flow. a) 20-10-2-80, b) 5-10-2-50, c) 40-10-2-50, d) 20-10-3-25. The left side of the powder bed is the build bed while the right side is the feed bed.

On the other hand, fine powder printed with gas flow has a better surface finish than the coarse one (see fig. 4.13). The best parameters found have been: LT of 105 μm, FLT ratio of 3, feed and build speed of 10 and 5 mm/s respectively. LTs from 30 to 120 μm have been checked with no big differences. However, with low LT during the deposition of a new layer the just printed part may be shift along the direction of the spread. For comparison with the coarse powder, the same LT has been chosen. The optimal FLT is 3 since it allows a uniform deposition throughout the bed. Homogeneous layers have been achieved with 10mm/s for the feed speed and the build speed enables good spread with values from 10 to 80 mm/s. However, to ensure a stable part the lowest limit has been used.

Lastly, the fine powder is also more sensitive to the humidity of the working place. Before printing, the powder has been dried in an oven (100 °C) in order to inhibit the tendency to aggregate.

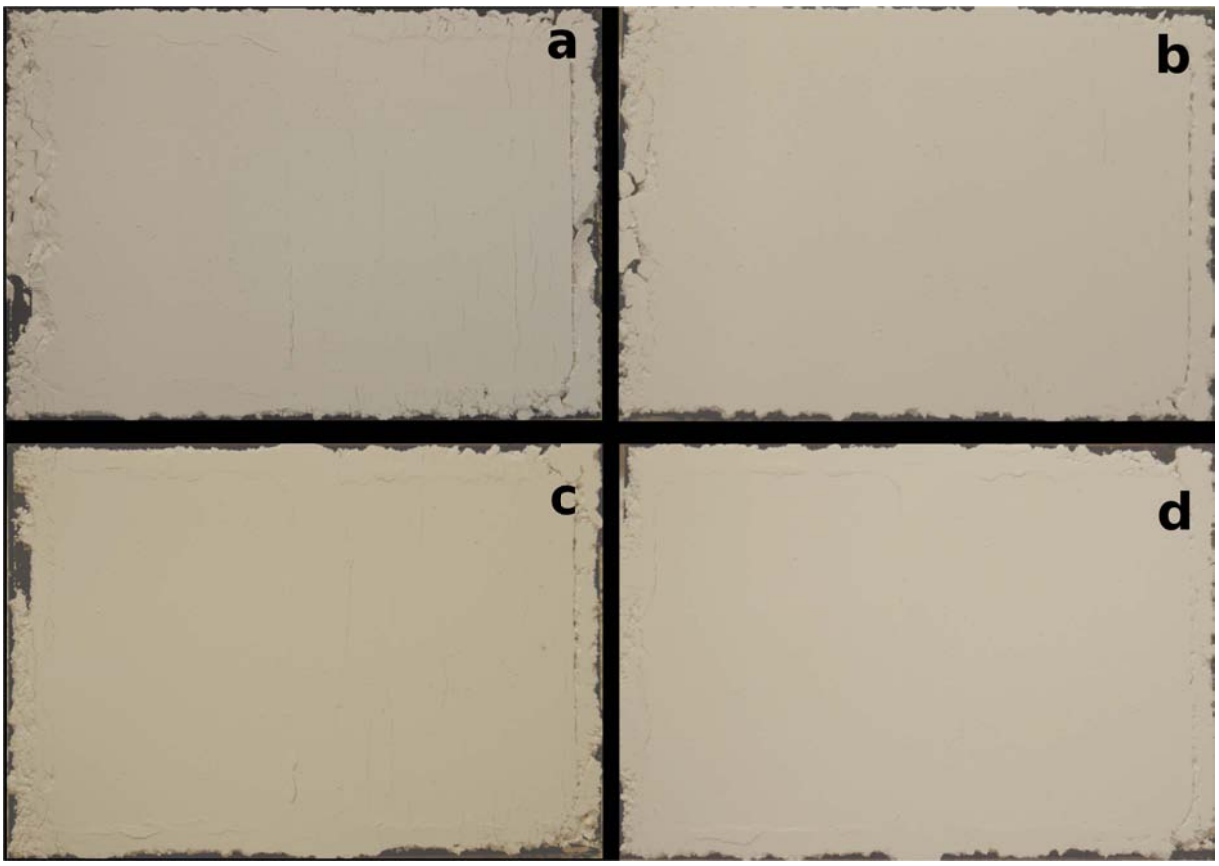

Figure 4.13: Powder bed deposition of the fine α-TCP powder after 15 layers with gas flow. a) 10-10-3-120, b) 10-10-3-80, c) 20-10-3-50, d) 40-10-3-30. The left side of the powder bed is the build bed while the right side is the feed bed.

In conclusion, the effects of the powder deposition assisted by gas flow are:

- increase of the powder bed density;
- deposition and printing of fine particles are possible;
- support structures may be avoided;
- reduction of powder contamination on the print head since the powder is more attached to the platform.

Once the parameters of the deposition are found, to check the flowability and density of the powder bed, the Hausner ratio, packing rate, and powder bed density have been calculated (see section 3.2 for the definitions). The values are reported in table 4.4.

The packing rate of the fine particles is lower than the big ones, thus the Hausner ratio is higher (1.55 compared to 1.35). Indeed, fine particles have a low flowability and compaction rate than coarse ones due to the higher surface area that causes an higher interparticle attraction force. This is one of the main challenge of printing powder smaller than 50 μm.
To appreciate the effect of the gas flow the powder bed density is a relevant parameter. The coarse powder with gas reaches the highest powder bed density followed by the fine particles with gas and the coarse particles without gas. The effect of the stabilization through the gas flow is particular evident in the coarse powder which shows a powder bed density $\sim$ 20% higher due to the gas flow. Again, the reason why the fine particles show a lower bed density compared to the coarse ones with gas may be linked to the poor flowability of the fine particles. Indeed, even with gas flow they are not significantly packed. Anyway, it is important to remind that without gas flow a uniform deposition is not feasible for such a small powder. Lastly, the powder bed density is a useful tool that can be associated to the green density of the printed part indeed the green body density will follow the same trend. Therefore, this is connected to the sintering capability of the three typologies of tablets. During sintering, a higher green density allows to get a greater density of the part at lower sintering temperature or for shorter dwelling times [66].

Table 4.4: Hausner ratio, packing rate and powder bed density of α-TCP powder. The percentages refer to the theoretical density of α-TCP.

Type	Printing method	Hausner ratio	Packing rate (%)	Powder bed density (%)
Fine powder	with gas-flow	1.55	24.8	39.3
Coarse powder	with gas-flow	1.35	38.5	43.9
Coarse powder	without gas-flow	1.35	38.5	36.0

4.2.2 3D printing

Apart from layer thickness, powder bed speed and feed to layer thickness ratio, the other printing parameters used are:

- to print tablets with the coarse powder: saturation of 140% and drying time of 60 s;
- to print tablets with the fine powder: saturation of 115% and drying time of 80 s;
- to print cubes with the coarse powder: saturation of 100% and drying time of 70 s;
- to print cubes with the fine powder: saturation of 115% and drying time of 80 s.

In fig. 4.14 the end of the printing of the tablets are shown. Six tablets can be printed at the same time and the surface finish of the fine powder *(b)* is smoother than the coarse one *(a)*. Furthermore, the effect of the gas flow can be appreciated from pictures *c,d*: after printing the build bed has been lifted and the powder still maintains the shape of the build volume due to the higher compaction of the powder bed.

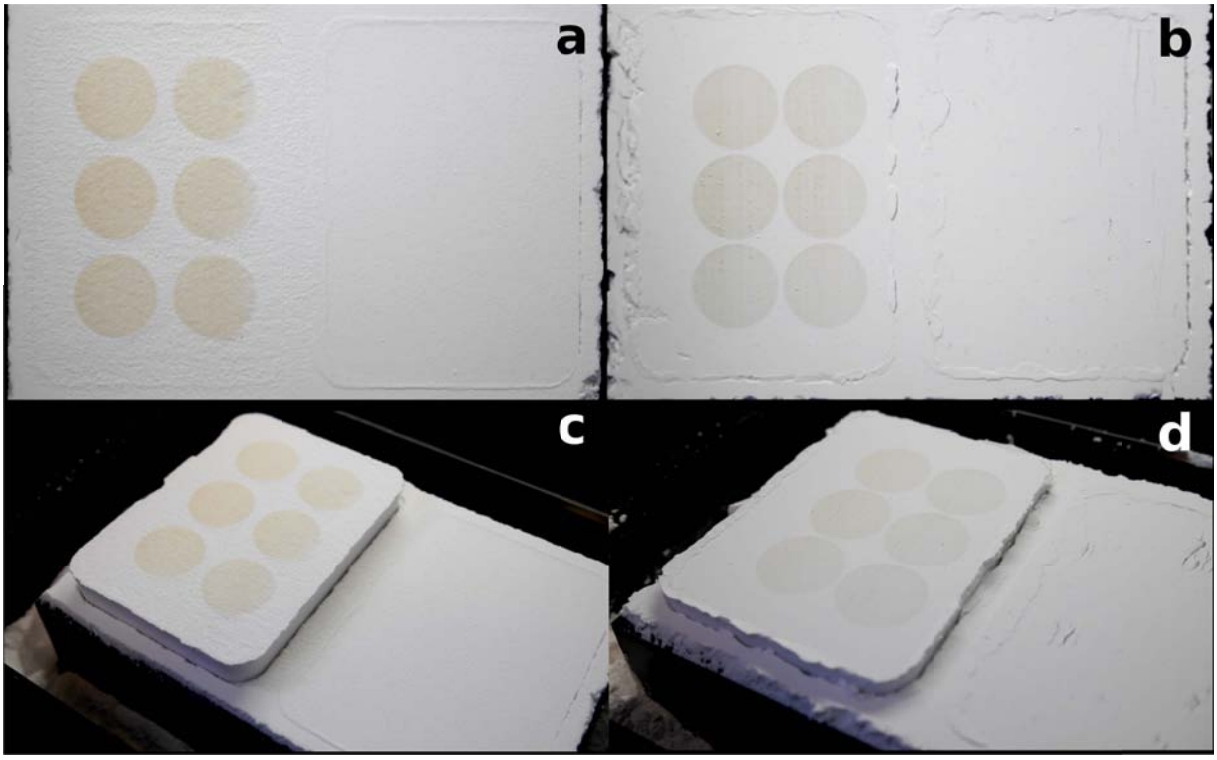

Figure 4.14: Post printing of the α-TCP tablets. Final layer of the coarse (a) and fine (b) powder, effect of the stabilization through a gas flow: compacted powder bed of the coarse (c) and fine (d) powder.

4.3 Sintering process

This section briefly illustrates the tablets and the scaffolds after sintering.
The initial sintering program used has been previously reported in fig. 3.12. Fig. 4.15 and 4.16 show all the three tablets and cubes before and after sintering. The sintering process results in a volume reduction and the sintered parts become white due to the loss of the binder. Moreover, parts printed with fine powder seem to have a more glassy appearance. The XRD analyses of the parts after sintering confirm that no other phases apart from α-TCP are visible.

(a) Coarse powder tablets after support removal (printed without gas flow).

(b) Coarse powder tablets (printed with gas flow).

(c) Fine powder tablets (printed with gas flow).

Figure 4.15: α-TCP tablets after printing (*left*) and sintering (*right*).

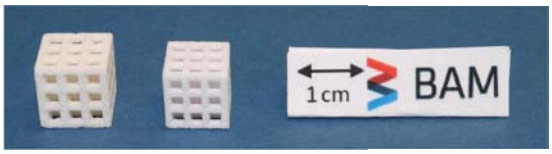

(a) Coarse powder cubes after support removal (printed without gas flow).

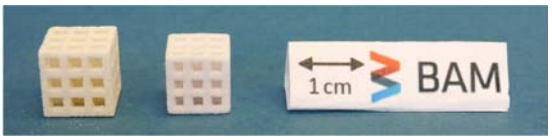

(b) Coarse powder cubes (printed with gas flow).

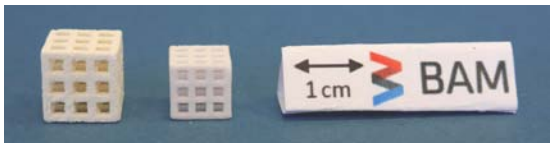

(c) Fine powder cubes (printed with gas flow).

Figure 4.16: α-TCP cubes after printing (*left*) and sintering (*right*).

4.4 α-TCP tablets

In this section, all the analyses carried out on the α-TCP tablets are reported. First, to understand the effects of the stabilization of the powder bed through the gas flow, density measurements and B3B results are delineated in section 4.4.1 and 4.4.2 respectively. Afterwards, shape, morphology, distortions and defects are investigated: macroscopic geometrical variations are covered in section 4.4.3, OM and SEM images are described in section 4.4.4 and μCT analyses in section 4.4.5. Then, section 4.4.6 deals with an attempt to evaluate the grains size by acid and thermal etching to figure out whether or not there is a correlation with the mechanical properties of the tablets. Last, further sintering programs have been performed to improve the B3B strength (section 4.4.7).

4.4.1 Density measurements

The density of the powder has been measured with a He pycnometer and the values are reported below:

- 2,85722 g/cm^3 for the coarse powder;
- 2,86491 g/cm^3 for the fine powder.

These results are almost equal to the theoretical density of α-TCP (2.866 g/cm^3) but it must be considered that the powder contains 7% of HA that alters the result for a direct comparison. Indeed, the density of HA (3.156 g/cm^3) is slightly higher than that one of α-TCP [67, 68, 69]. Having said that, the fine powder has a bit higher density maybe due to a lower number of closed pores since both materials come from the same batch so the two types are chemically equal. The fine powder had a greater grinding that might have caused a higher reduction of the closed porosity. Indeed, during the measurement the gas used (in this case He) can better penetrate in all the holes of the particles.
Additionally, the density of the tablets has been measured by the Archimedes' method according to the ISO 18754 with vacuum to remove all the air from the pores before resin impregnation. With this method three features are calculated: bulk density (ρ_b), apparent solid density (ρ_a) and apparent porosity (π_a) by measuring three masses (expressed in kilograms):

- m_1: is the mass of the dry sample;
- m_2: is the apparent mass of the immersed sample;
- m_3: is the mass of the soaked sample;

Moreover, the density of the immersion liquid (ρ_1) at the temperature of the test is necessary. In this case, water has been used.
It is important to clarify some terms used:

- The bulk density is defined as the ratio of the dry sample to its bulk volume (that is, the volume of the solid material, the open and closed pores). It is calculated as follows;

$$\rho_{\mathrm{b}} = \frac{m_1}{m_3 - m_2}\rho_1 \tag{4.1}$$

- The apparent solid density is the ratio of the mass of the dry material to its apparent solid volume (the respective volume of the solid material and the closed pores). It is calculated as follows:

$$\rho_{\mathrm{a}} = \frac{m_1}{m_1 - m_2}\rho_1 \tag{4.2}$$

- The apparent porosity is the ratio of the volume of the open porosity to its bulk volume and it is calculated as follows:

$$\pi_{\mathrm{a}} = \frac{m_3 - m_1}{m_3 - m_2}100 \tag{4.3}$$

Pressed tablets have also been sintered to have a sort of high density reference. These tablets (16 mm in diameter and 3 in height) have been pressed in a steel mould with a preload of 5 kN and a final load of 10 kN for 30 seconds.
The findings are shown in fig. 4.17. The results are in agreement with the predictions: the fine powder is denser than the coarse one and during printing the gas flow makes the part denser. Furthermore, pressed tablets are denser than the equivalent printed tablets. Focusing on the apparent solid density, all the three types of coarse powder have a value higher than 99% meaning that the amount of closed pores is extremely low and this has a particular relevance for the mobility of the biological nutrients (see table 4.5 for all the relative values). No significant effects can be noticed for the printing with gas flow. Practically, the closed porosity of the part is similar to that one of the powder itself. On the other hand, the printed and pressed tablets with fine powder show percentages of 96.73 and 94.96% respectively. The denser the part, the more difficult to eliminate the closed pores during sintering, especially without viscous flow. This may be linked to the fact that using the same sintering process, in the fine powder the effect of coarsening is higher than the densification and this promotes pores structures [66]. Fig. 4.18 shows the amount in percentage of the closed pores in the tablets. These values have been obtained

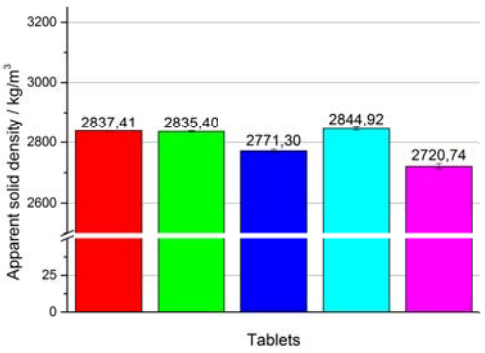

(a) Apparent density in kg/m^3.

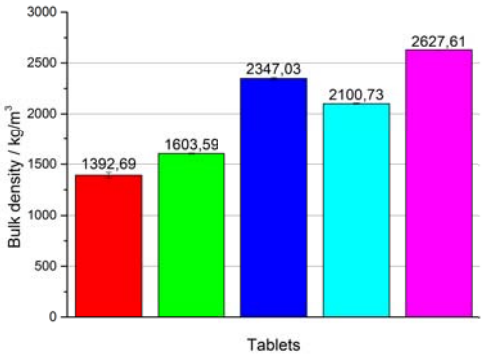

(b) Bulk density in kg/m^3.

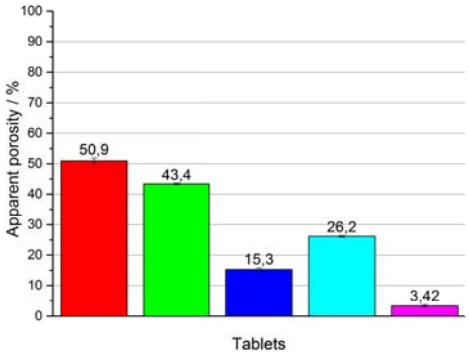

(c) Apparent porosity.

Figure 4.17: Density and porosity measurements of the α-TCP tablets according to the ASTM standard. The values reported are in the form *mean value* $\pm$ *standard error*. Legend:

- Coarse powder (printed without gas flow)
- Coarse powder (printed with gas flow)
- Fine powder (printed with gas flow)
- Coarse powder (pressed)
- Fine powder (pressed)

subtracting the apparent porosity from the total porosity as follows:

$$\begin{aligned} \text{Closed porosity} &= \text{total porosity} - \text{apparent porosity} \\ &= \left(1 - \frac{\rho_\text{b}}{\rho_\text{powder}}\right) 100 - \pi_\text{a} \end{aligned} \tag{4.4}$$

It is important to keep in mind that these values do not truly represent the exact amount

Table 4.5: Relative apparent solid and bulk density of the tablets. Values in % compared to the density (by pycnometer) of the α-TCP powder synthesized.

Type	Apparent solid density	Bulk density
Coarse powder printed without gas	99.30	48.01
Coarse powder printed with gas	99.23	56.12
Fine powder printed with gas	96.73	81.92
Pressed coarse powder	99.56	73.52
Pressed fine powder	94.96	91.71

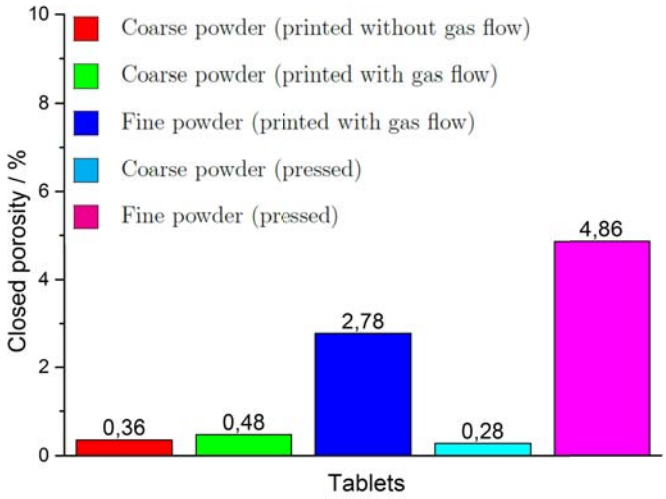

Figure 4.18: Closed porosity of the α-TCP printed and pressed tablets.

of closed porosity since the method is not entirely reliable for such a low quantity, therefore the results can only give a comparative idea between the samples.

When looking at the bulk density, the tablets made with the fine powder have the highest density, in particular the pressed ones. In other words, the open porosity is very low: 15.3 and 3.42% for the printed and pressed tablets due to the small particle size and thus, the promoted sintering behaviour. Regarding the coarse powder, since the apparent solid density is almost similar, the different open porosity results in a variation of the bulk density: the tablets printed with gas flow show a higher density, and the pressed one have the greatest value. Here, the effect of the gas flow can be appreciated as it reduces the porosity in agreement with the results from the powder bed density. Nevertheless, it is interesting to note that the powder bed density of the fine powder has a value between the coarse tablets printed with and without gas flow. At the end instead, the fine tablets are the densest due to the higher densification rate over sintering.

4.4.2 Ball on three balls test (B3B)

To investigate the mechanical properties of the α-TCP tablets the ball on three balls test has been carried out and the results are reported in fig. 4.19.
The radius of the supporting balls (R_a) is 5.5 mm and the Poisson ratio used is 0.25. Considering the printed tablets, those printed with the coarse particles without gas and

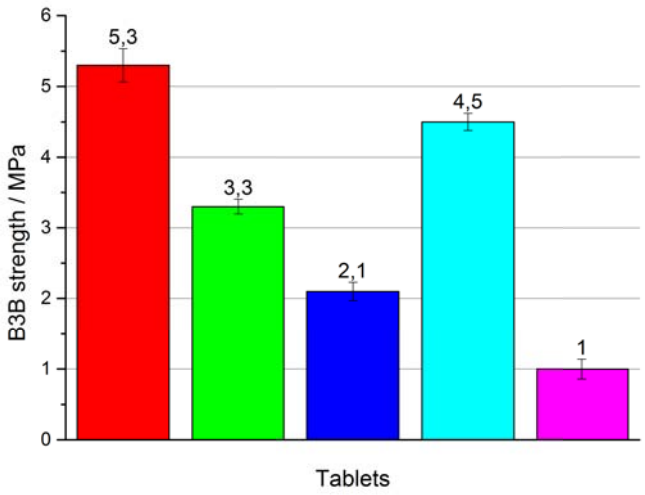

Figure 4.19: Ball on three balls test of the α-TCP printed and pressed tablets. The values reported are in the form *mean value* $\pm$ *standard error*. Legend:

- Coarse powder (printed without gas flow)
- Coarse powder (printed with gas flow)
- Fine powder (printed with gas flow)
- Coarse powder (pressed)
- Fine powder (pressed)

then with gas have the highest values followed by the tablets made of the fine particles. When comparing these findings with the porosity (fig. 4.17c), the trend expected is the opposite: theoretically, denser parts should have higher mechanical properties. However, this is not the case. There may be different reasons for that: probably, the sintering process may have cause an excessive grain growth in the fine tablets therefore the tablets with the lowest green density has a moderate grain growth compared to the others. Assuming all the tablets reached the final stage of the sintering process characterized by an extensive grains growth, according to the powder bed density values, the coarse tablets printed with gas and the fine tablets (which have higher green density) have spent more time in the coarsening stage. Therefore, the higher the green density, the lower the mechanical strength. Besides, fine powder has a faster densification rate and therefore in addition to have the second highest value of powder bed density, the effect of the

small particles further promotes the grains growth. Thus, the fine tablets have the lowest strength. Nevertheless, as it can be read in section 4.4.6, no information has been found about the grain size. Despite that, this may not be a determinant issue since from the work of Miranda *et al.* [65] the grain size of the α-TCP samples does not increase from 2 to 6 hours at 1550 °C (particles size 1.8 ± 0.8 μm) .

The most likely reasons for the mechanical trend rises from an investigation with the microscope (see section 4.4.4): more cracks are visible in the tablets printed with the fine powder. Therefore, especially due to the tensile stress, these cracks promote an easy break of the tablets. Furthermore, the tablets with an higher density may be more affected by the cooling rate that may cause a sort of thermal shock. The reason of the formation of cracks may due to the phase transformation between α and α' where the crystal structure turns from monoclinic to hexagonal with stress formation.

With regard to the pressed tablets, the fine ones match the previous consideration: the denser the green part, the more time spent in the grains growth stage and therefore lower mechanical properties. However, the pressed coarse tablets have a behaviour intermediate the coarse tablets printed without and with gas. Instead, they should have a strength lower than the coarse tablets printed with gas to be in accordance with the same thought. It means that the coarsening has been delayed somehow.

With regard to the mechanism of fracture, generally, during the test the tablets have broken in two or three parts as shown in fig. 4.20. In agreement with the threefold symmetry of the stress state, the theoretical number of broken parts should be three but due to micro cracks, flaws and imperfections already present in the sample, this number may vary. Moreover, the correlation between the amount of pieces and strength has not been found and the relationship according to which the strongest tablets should break in three parts is not verified [54, 70, 71].

(a) Coarse powder tablets printed without gas flow.

(b) Coarse powder tablets printed with gas flow.

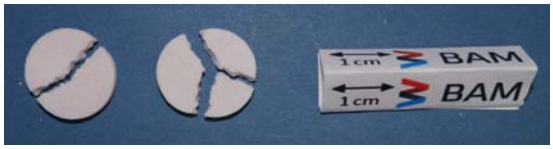

(c) Fine powder tablets printed with gas flow.

Figure 4.20: Broken α-TCP tablets after the ball on three balls test.

4.4.3 Geometrical variations

To evaluate the geometrical deviations of the printed and sintered tablets, height and diameter have been measured with a caliber (three times) and compared to the nominal size (the STL file) (see fig. 4.21). The comparison *printed-sintered* is the shrinkage after sintering, the *STL-printed* measurement refers to the accuracy during printing while the comparison *STL-sintered* is the overall variation that must be taken into account to print objects with a specific dimension. Therefore, knowing the scale factor *STL-sintered* the part can be printed according to the requirements.
First, with regard to the height variation (see fig. 4.21a), the shrinkage after sintering is similar for the coarse tablets without gas flow and the fine tablets with gas flow ($\sim$16%) while surprisingly the coarse tablets printed with gas flow show less than 5%. More interesting, the comparison *STL-printed* points out the effect of support removal. The tablets printed with the coarse powder without gas flow have been printed with the support structure. After printing and drying the tablets, the support has been removed with an abrasive paper. Apparently, still some layers remained and this explains the increase in height. On the other hand, the height variation is minimum for the powder printed with gas.
At the end, compared to the STL file, the sintered parts with fine particles has the biggest height variation. Anyway, a little increase may be caused by the swelling of the binder after the tablets have been dried in the oven at 100 °C.
Second, focusing on the diameter (see fig. 4.21b), the variation is similar for the coarse powder, while for the fine tablets it reaches $\sim$16%. It is noteworthy the fact that the height and diameter variation for the tablets printed with fine powder have almost an isotropic shrinkage. The diameter variation between STL file and printed part has the opposite trend of the height. Finer tablets and with gas have a higher change even though it is almost negligible. This may also be connected to the sucking force of the gas flow. The binder is subjected to the pressure of the gas and therefore it can penetrate downward between particles or bypass the particles along the plane normal to the pressure gradient. The overall effect is that the binder glues more particles along the plane increasing the diameter of the printed part. The trend of the height variation can also be connected since the powder is compressed in the z-axis and therefore it slightly expands along the diameter. At the end, the *STL-sintered* comparison is almost three times higher in the fine tablets compared with the coarse ones which are nearly equal.
Lastly, the overall volume variation is depicted in fig. 4.21c. It can be noticed the advantage of printing with fine powder and with gas flow. The printed parts with gas flow and with fine particles better match the STL file: the geometrical variations are much smaller compared to the coarse powder. At the end, since both height and diameter decrease, the fine tablets have the highest volume variation.

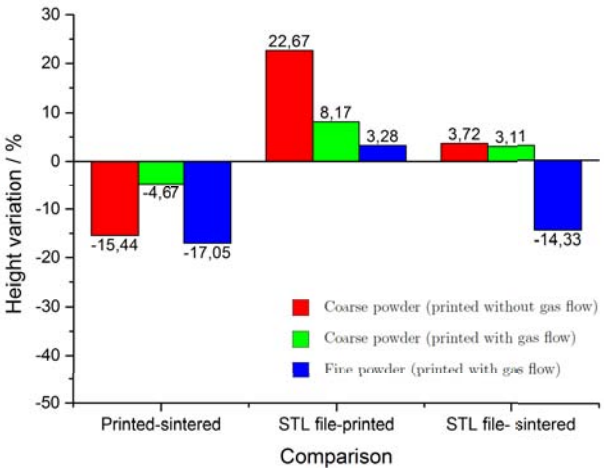

(a) Height variation of the printed α-TCP tablets.

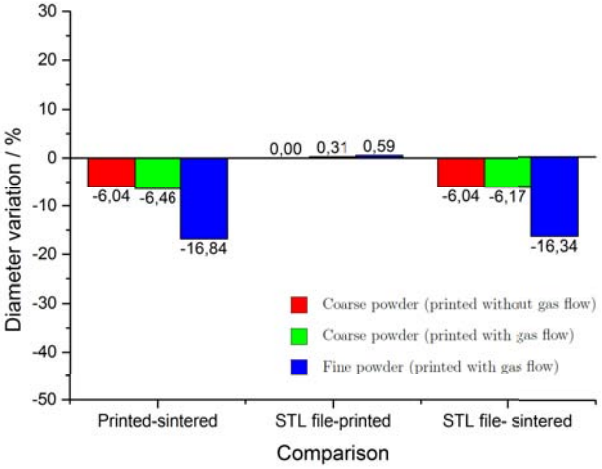

(b) Diameter variation of the printed α-TCP tablets.

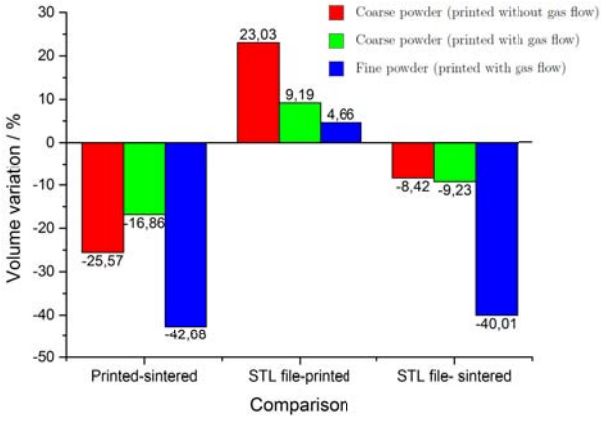

(c) Volume variation of the printed α-TCP tablets.

Figure 4.21: Height, diameter and volume variations of the α-TCP tablets in %. Comparison between the printed-sintered, STL file-printed and STL file-sintered tablets.

4.4.4 OM and SEM microscopy

OM (optical microscope) and SEM (scanning electron microscope) images have been taken in order to study the morphology and the presence of defects on the printed samples.

Fig. 4.22 shows the coarse (a) and the fine (b) powder. The shape of the particles is irregular due to the grinding process (with a ball miller). The particle size distribution is rather wide and for both typologies present a trimodal distribution as visible from the particle size analysis (fig. 3.2) and partially from the SEM images: for the fine powder the major size distribution is around 10 μm and the minor peaks are around 1 and 300 μm. For the coarse powder the major peak is at 70 μm and the minor distribution are around 8 and 1 μm.

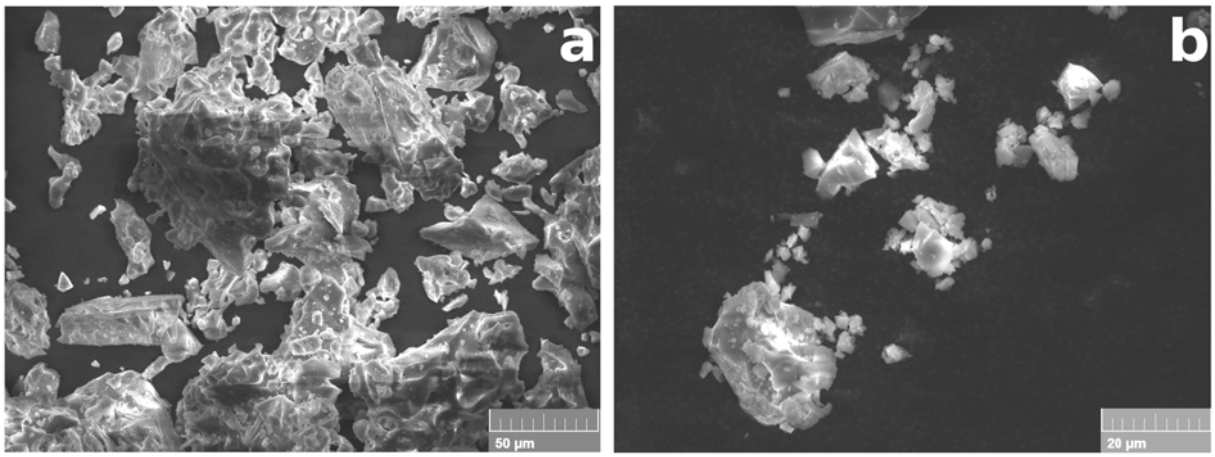

Figure 4.22: SEM images of the α-TCP powder: coarse (a) and fine powder (b).

With regards to the tablets that have been embedded in epoxy resin and then polished, fig. 4.23 and 4.24 well illustrate their morphology. Before being embedded, the tablets have been put under low vacuum in a sealed chamber to remove all the air from the pores. Then, the resin has been poured in the samples still in the vacuum chamber (in other words, the resin has been sucked in due to the difference pressure). Fig. 4.23 and 4.24 point out the same features of the tablets so they will be discussed together.
Firstly, when looking at the images at low magnification, the different density is clearly

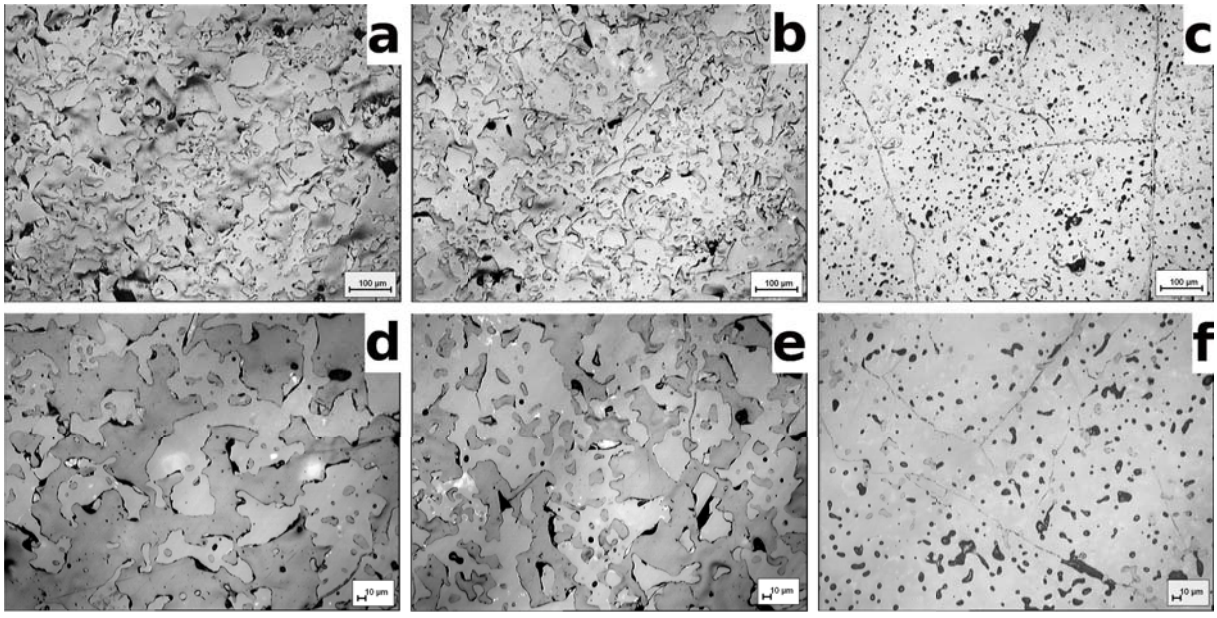

Figure 4.23: OM images of the α-TCP tablets after being embedded in epoxy resin (dark grey colour) and polished: coarse powder tablets printed without gas flow (a, d), coarse powder tablets printed with gas flow (b, e), fine powder tablets printed with gas flow (c, f).

visible especially between the coarse and fine tablets. Images a, b reveal a high porosity of the tablets with a random distribution of the material in the tablet. It is a bit ambitious

to note the higher porosity (around 7%) of the coarse tablet printed without gas flow (*a*) as it can strongly vary depending on the spot analysed. The fine tablet instead, has a higher density since most of the surface is covered by the material (the apparent porosity is roughly one third compared to the coarse tablets).
One of the most interesting facts that can be pointed out is the increasing amount of cracks from the coarse tablet printed without gas to the fine tablet (that is, proportional to the density). While from the images *a* cracks are rarely found, in the fine tablets (*c*) cracks are spread throughout the surface. An intermediate situation occurs in the coarse powder printed with gas flow. To further appreciate this phenomenon, the images at higher magnifications (*d, e, f*), show some cracks that completely cut parts of the material. Cracks develop from void to void and closed porosity seems to be more detrimental for the strength of the tablet. Having said that, some cracks may be introduced during the polishing procedure but for these images this situation is excluded since cracks formed from the polishing and from the sintering process appear differently under the microscope. Indeed, in those formed during polishing there is not resin inside therefore during the analysis these cracks are visible as grooves. Similar consideration can be made for the porosity: closed and open porosity can be distinguished from the images. Basically, the open porosity corresponds to the resin: the latter could penetrate in all the pores due to the interconnectivity of the channels. On the other hand, in the OM images, the closed porosity (*c, f*) coincides with the black spots since despite the ultrasonic cleaning, the abrasive solution used during the polishing remained in the pores. In the SEM images (*c, f*), the closed porosity is related to those empty void with a white profile due to the electrical charge accumulation. A last comment is worthy to be made: the distinction between open and closed porosity is reliable if the resin could penetrate in all the open pores otherwise these open pores not filled with resin may be meant as closed porosity.
The already discussed B3B trend of the tablets can be attributed to presence of cracks that increase with the density. The worst scenario is that one in the fine tablets where cracks are well spread making the force to break the part extremely low. Due to the biaxial stress of the B3B test, cracks easily grow connecting the closer pores until the final failure.
The reason for the formation of the cracks is not completely understood. DTA analyses confirm that α-TCP is stable enough to not show the transformation to β so this lattice change does not happen causing none distortion. The main explanation is the phase transformation between α and α' both during heating and cooling at around 1460 °C. As reported in table 2.1, α and α'-TCP have a density of 2.866 and 2.702 g/cm^3 that may cause a slight expansion during cooling with the formation of cracks. More specifically, even though the density difference is not so big, the lattice crystal is completely different: α-TCP is monoclinic whereas α'-TCP is hexagonal. As a result, the lattice constants (*a,*

b, c) vary significantly since the lattice structure is subjected to an extensive modification.

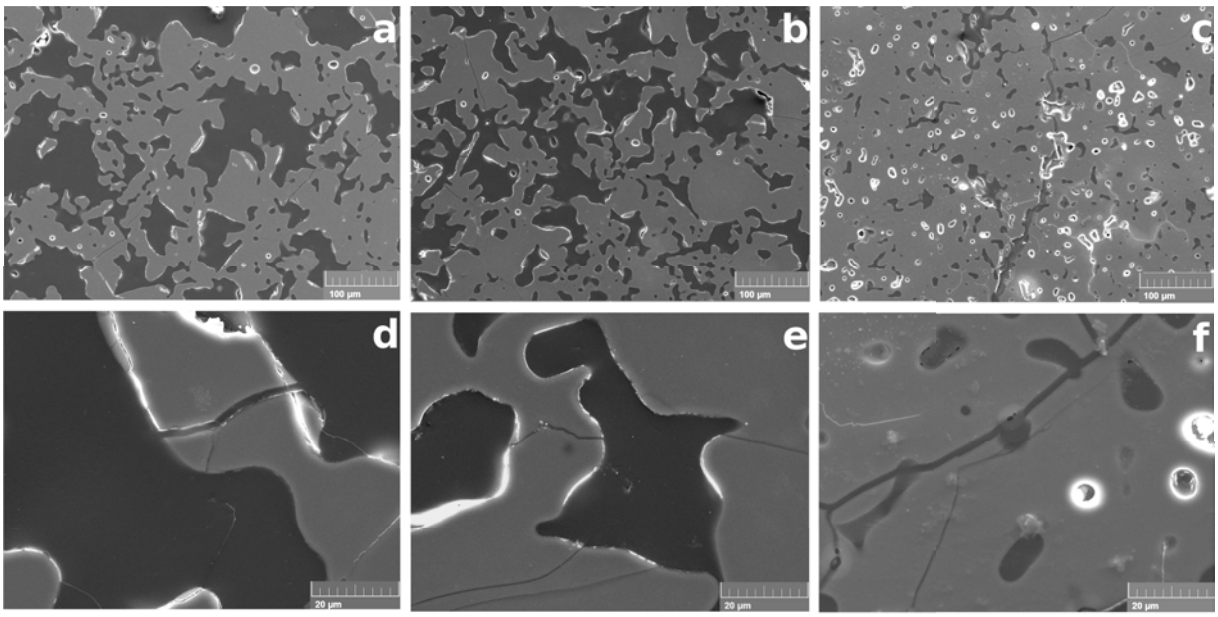

Figure 4.24: SEM images of the α-TCP tablets after being embedeed in epoxy resin (black colour) and polished: coarse powder tablets printed without gas flow (*a, d*), coarse powder tablets printed with gas flow (*b, e*), fine powder tablets printed with gas flow (*c, f*).

4.4.5 μCT analysis

To evaluate geometrical variations and macroscopic defects, μCTs and data analyses (with VG studio) have been carried out on the printed and sintered tablets.
First of all, it is important to remind that a surface determination of the scanned part must be performed to analyse the image from the CT. This corresponds to decide the boundaries of the scanned part avoiding that the software considers unwanted scanned area part of the object of interest. This procedure is rather simple for dense objects since the border between 'matter' and 'nothing' is evident but for very porous parts the distinction may be more difficult and consequently the results strongly depend on this first choice. In conclusion, the same scanned part may show small different results depending on the person who elaborates the data from the CT and the comparison between scanned parts is not quantitatively reliable.
Having said that, fig. 4.25 illustrates the transversal and longitudinal internal area of the three typologies of tablets. Some considerations can be outlined:

- Geometrical variations: about the size of the tablets, the fine one is clearly smaller in diameter and height due to a more marked densification during sintering. Moreover,

from the transversal section of the coarse powder printed without gas flow a slight lateral shift is visible. This is due to a too high build speed that causes a repeated lateral movement of the just-printed layer. On the other hand, the coarse tablet printed with gas flow does not show such a distortion thanks to the stabilization of the powder bed. It is worthy to note that the build speed for the latter is 5 times higher than the printing without gas flow. This points out the great positive effects of the gas flow on the geometrical accuracy of the printed parts. About the fine tablet (printed with gas flow), the transversal section reveals a bending phenomenon caused by stresses during sintering.

- Porosity: a general idea of the porosity can be appreciated from the images (white spots). A more evident porosity can be noticed in the coarse powder printed without gas flow throughout the area whereas the amount of pores increases from the edge to the center in the coarse tablet printed with gas flow. On the other hand, the fine tablet shows the smallest amount of porosity that is mainly localized in the center of the tablet. No gradients along the z-axis can be seen in the coarse tablets indicating that the pressure of the gas flow is constant along the height. Instead, in the fine tablet, the porosity seems to increase towards the upper surface.

- Defects: delamination of some layers can be observed in the fine tablet especially close to the edges because of the higher stresses formed. Fig. 4.26 better depicts this printing imperfection: on the left, a transversal slice close to the edge is illustrated and the arrows indicate the layers delaminated. On the right, the overall tablet with the delamination is shown at lower magnification. To avoid these delaminations, a possible solution is to vary saturation and drying time. A higher saturation can better glue the particles together or a lower drying time between the deposition of each layer can make the layers more joined. Another solution may be to decrease the layer thickness if the deposition is still homogeneous.

A further analysis to evaluate the geometrical deviations between the stl file (see fig. 3.9a) and the printed parts is reported. The stl file and the scanned part have been registered together with the best matching possible and then, a comparison between nominal-actual size has been carried out. Thanks to the colour legend the deviations are easily visible: green represents an area that matches the original file while a colour tending towards red or blues means a positive or negative deviation. Concentric circles on the surfaces are only artefacts of the data elaboration. All the variations are included in a range between ± 1.5 mm.

The results confirm the previous considerations: with regard to the coarse tablets (see fig. 4.27 and fig. 4.28) all the area on the edge is blue coloured meaning that the tablets have shrunk a little during the sintering. Moreover, that one printed without gas shows

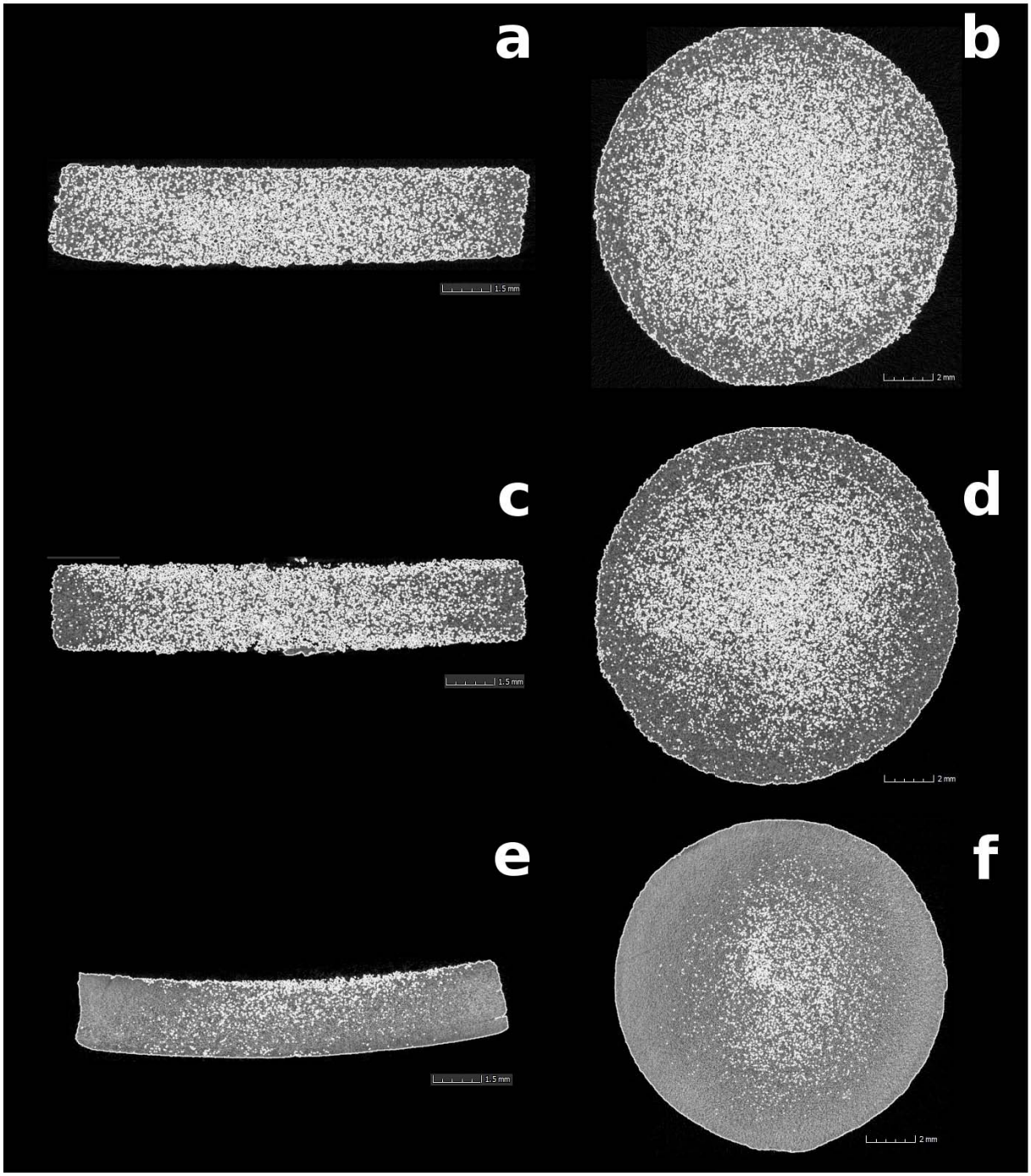

Figure 4.25: Transversal and longitudinal sections of the α-TCP tablets from μCT analysis: coarse powder cube printed without gas flow (*a, b*), coarse powder cube printed with gas flow (*c, d*), fine powder cube printed with gas flow (*e, f*).

two hues of blues due to the lateral shift. About the lower-upper surfaces there are not deviations to point out.

When looking at the fine tablet (fig. 4.29), the bending is clear from the more intense green on the upper surface and the presence of blue on the lower surface close to the edge. In the center of the tablet instead, a hue of blue appears on the upper surface

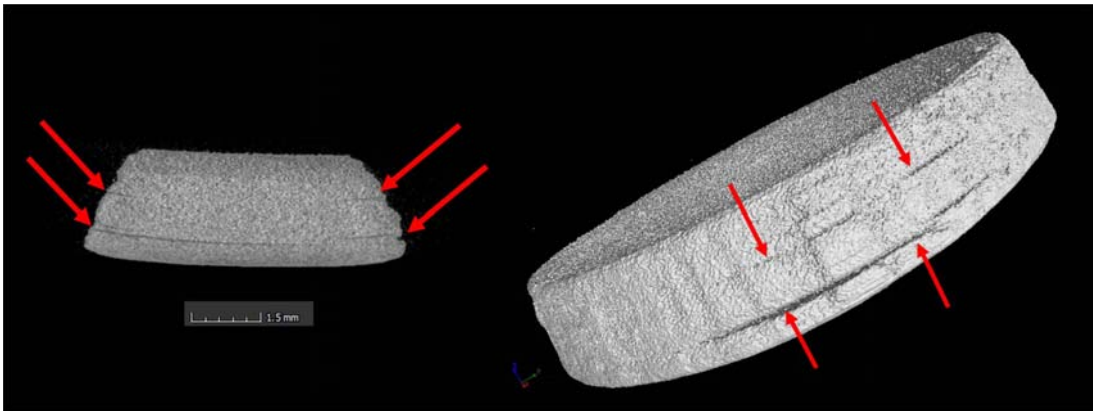

Figure 4.26: Transversal sections (*left*) and overall image (*right*) of the fine α-TCP tablet from μCT analysis: delaminations (red arrows) visible especially close to the edges of the tablet. Images not in scale.

while an intense green on the lower surface.

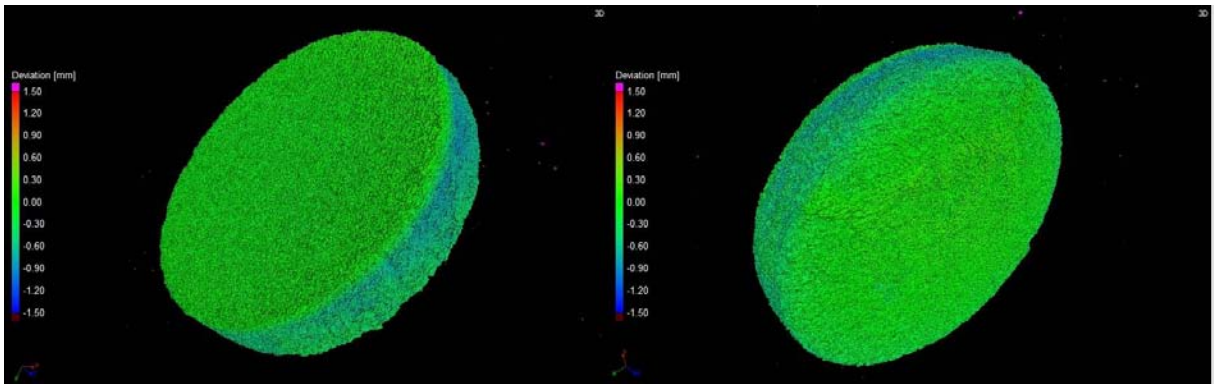

Figure 4.27: μCT of the coarse α-TCP tablets printed without gas flow: deviations from the original stl file.

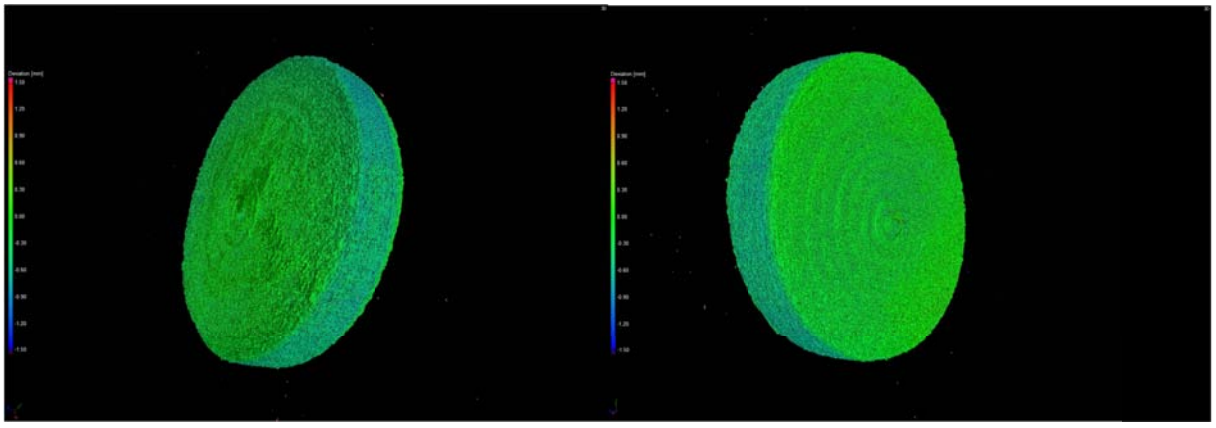

Figure 4.28: μCT of the coarse α-TCP tablets printed with gas flow: deviations from the original stl file.

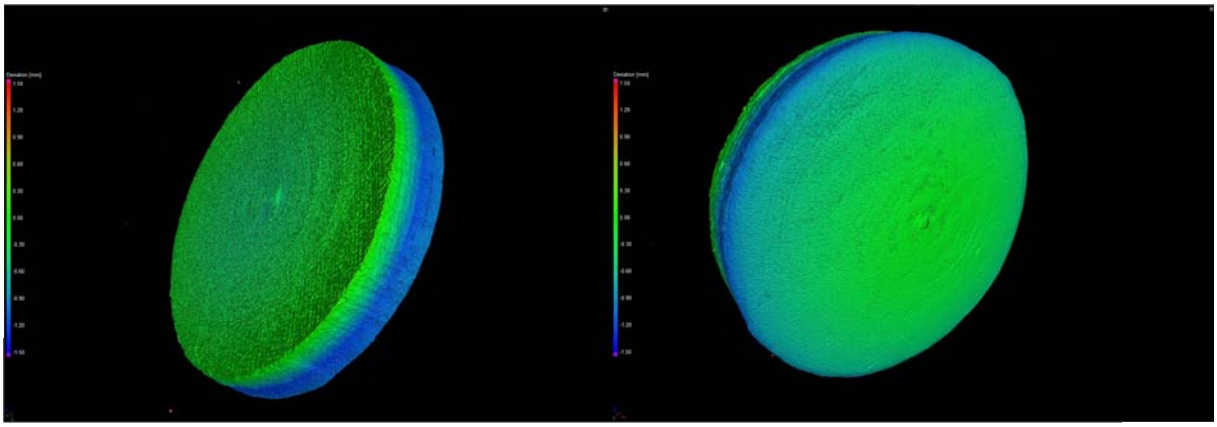

Figure 4.29: μCT of the fine α-TCP tablets printed with gas flow: deviations from the original stl file.

4.4.6 Acid and thermal etching

In order to have information about the grain size of the tablets, acid and thermal etching has been carried out. However, the evaluation through the optical and electron microscope has not revealed any interesting feature. Information about the grain size may have helped to understand whether or not there is a relationship with the mechanical properties.
With regard to the acid etching, after being polished, the tablets have been etched with hydrofluoric acid (10% HF) for 30 and 60 seconds and with citric acid (10% $C_6H_8O_7$) for 30 seconds.
On the other hand, the thermal etching has been more difficult to carry out due to the high porosity of the tablets. This method is usually employed for ceramics due to the high chemical resistance to acids. Basically, by polishing the sample, the thermodynamic shape of the grains is altered. This new formed surface has a higher surface energy than the original. By thermal activation, grains tend to crystallize to achieve a lower surface energy. If the right parameters are chosen, some different levels between boundaries and grains can be noticed. In this case, the main problem deals with the removal of the epoxy resin: first, the resin is necessary to polish the sample but before the thermal treatment it must be removed otherwise gaseous products of the decomposition can contaminate the laboratory. Therefore, after being polished, the tablets have been removed from the epoxy sample with a heat gun that simply softens the resin. This procedure is extremely delicate since the tablet, completely embedded in the resin, easily breaks. Then, the tablets have been heated up to 800 °C to take off entirely the resin in a debinding oven. Most of the tablets totally degraded due to the high porosity after the loss of the resin. Afterwards, thermal etching has been performed on the few survived tablets at 1450 °C for 30 minutes with a rate of 20 °C/min. However, the analyses at the microscope have not displayed anything in particular: besides, the samples analysed were not flat enough to be focused.

To sum up, trials to understand the grains size of the tablets have been done with HF, citric acid and thermal etching. Nonetheless, due to the geometry, the high porosity and the need to embed the tablets in the resin, this investigation is extremely tricky.

4.4.7 B3B results of different sintering programs

To further understand the reason of the lower strength of the tablets printed with gas-flow, other sintering programs have been carried out. The aim was to change only one parameter in order to understand whether or not the strength increases. However, both tablets printed with gas flow show lower B3B strength than the coarse tablets printed without gas flow (that has been used as a reference). To sum up, different sintering treatments have been chosen to better comprehend the causes of this behavior and the results of the B3B tests are reported in fig. 4.30 and the alphabetic legend is described below:

(a) 10 °C/min: RT, 450 °C (2h), 1600 °C (6h), RT; 7 samples tested

(b) 10 °C/min: RT, 450 °C (2h), 1600 °C (6h), RT; 14 samples tested

(c) 10 °C/min: RT, 450 °C (2h), 1600 °C (5h), RT; 5 samples tested

(d) 10 °C/min: RT, 450 °C (2h), 1600 °C (3h), RT; 6 samples tested

(e) 10 °C/min: RT, 450 °C (2h), 1600 °C (5h), 5 °C/min: 1300 °C, 10 °C/min: RT; 6 samples tested

(f) 5 °C/min: RT, 450 °C (2h), 10 °C/min: 1600 °C (5h), RT; 6 samples tested

(g) 10 °C/min: RT, 450 °C (2h), 1415 °C, 5 °C/min: 1515 °C, 10 °C/min: 1600 °C (5h), 1515 °C, 5 °C/min: 1415 °C, 10 °C/min: RT; 5 samples tested

(h) 10 °C/min: RT, 450 °C (2h), 1600 °C (6h), RT; 11 samples tested

(i) 10 °C/min: RT, 450 °C (2h), 1600 °C (4h), RT; 10 samples tested

(j) 10 °C/min: RT, 450 °C (2h), 1600 °C (2h), RT; 7 samples tested

(k) 10 °C/min: RT, 450 °C (2h), 1600 °C (2h), 5 °C/min: 1300 °C, 10 °C/min: RT; 6 samples tested

(l) 5 °C/min: RT, 450 °C (2h), 10 °C/min: 1600 °C (2h), RT; 6 samples tested

(m) 10 °C/min: RT, 450 °C (2h), 1415 °C, 5 °C/min: 1515 °C, 10 °C/min: 1600 °C (2h), 1515 °C, 5 °C/min: 1415 °C, 10 °C/min: RT; 5 samples tested

The reasons of the chosen programs are explained as follows:

- Treatments *c, d* and *i, j* consist of a reduction in the dwelling time at 1600 °C: letters *c* and *i* result in a higher strength and especially *c* results in the best value for the coarse tablets printed with gas flow (3.4 MPa) The idea behind it was that a dwelling time of 6 hours may have be too long causing an excessive grains growth that may have caused a reduction in mechanical properties. Reducing the dwelling time, a compromise of sintering activity and excessive grain growth may be achieved. However, no information about grains have been obtained.

- Another explanation could have been the formation of cracks during cooling due to the transformation α' to α: treatments *e* and *k* have a halved cooling rate (5 °C/min) so the stresses may be prevented. Nonetheless, the results do not improve.

- Another idea was the formation of cracks during the de-binding since denser parts have fewer ways for the gases to go out the tablets: treatments *f* and *l* have a cooling rate of 5 °C/min until the burnout of the binder. For the coarse tablets, this does not change significantly the results while for the fine tablets, the strength is the highest achieved (3.1 MPa)

- Treatments *g* and *m* are similar to *e* and *k* but both heating and cooling, around the phase transformation between α' to α the rate is 5 °C/min. No significant improvements are visible.

In conclusion, an attempt to improve the mechanical properties of the tablets has been performed by changing the sintering program without any significant result. The most likely reason might be the phase transformation between α' and α-TCP and viceversa and secondly, the de-binding stage. If so, for further studies, slower rates may be preferred to reduce the formation of stresses. Anyway, from a industrial point of view, this may significantly affect the cost of the production. Another suggestion may be to sinter the tablets at temperature lower than this transformation (around 1460 °C) for longer times but probably the sintering activity is too low to allow the particles to join together.

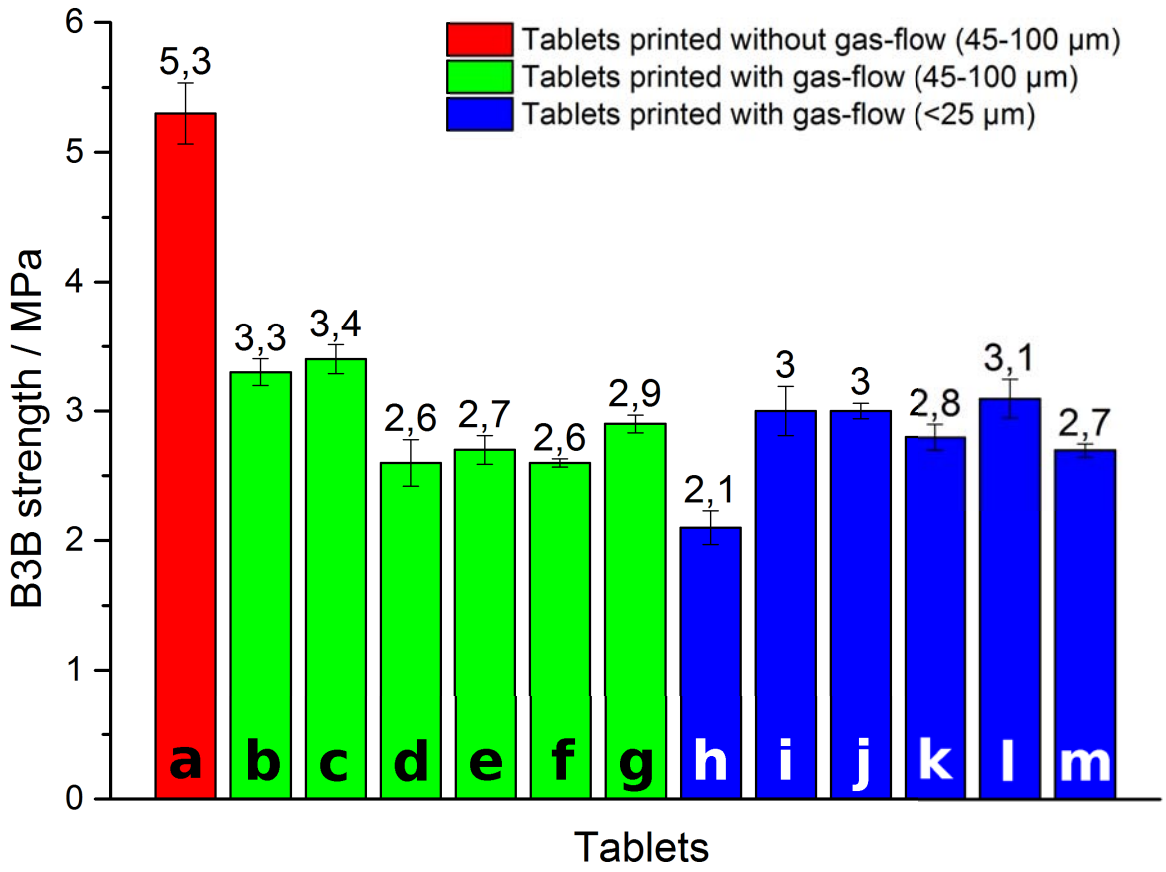

Figure 4.30: Results of the B3B tests of the α-TCP tablets after various sintering programs. Alphabetic legend in the text.

4.5 α-TCP scaffolds

In this section of the thesis, similar considerations made for the tablets will be outlined for the scaffolds. Density measurements and compressive tests are reported in sections 4.5.1 and 4.5.2 respectively. Afterwards, to analyse the morphology, microstructure and geometrical variations, sections 4.5.3 and 4.5.4 deals with the OM and SEM microscopy and the μCT analyses.

4.5.1 Density and porosity

The bulk density of the cubes has been calculated from the ratio between the weight of the cubes and the bulk volume measured with the caliber. The results are depicted in fig. 4.31.

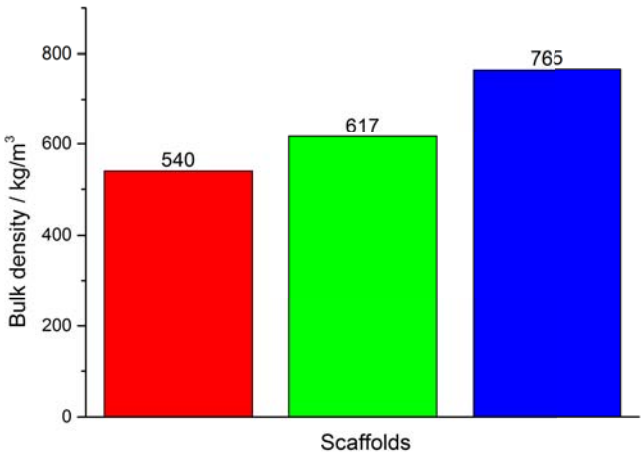

Figure 4.31: Bulk density of the α-TCP printed cubes. Legend:

- Coarse powder (printed without gas flow)
- Coarse powder (printed with gas flow)
- Fine powder (printed with gas flow)

The cubes that have been printed with fine powder (and therefore with gas flow) have the highest density due to the more marked shrinkage while those printed with the coarse powder without gas flow have the lowest value. As it can be seen in the following section, this affects the mechanical strength of the cubes since the latter increases with the density. Two types of porosity can be distinguished also in the scaffolds: the random and the designed porosity. The first derives from the process itself since dense parts are extremely difficult to achieve without post processing (such as infiltration). The latter refers to the porosity that has been designed: in this case, the cells among the struts. While the

random porosity is hard to measured directly for these geometries, an estimation of the designed porosity can be obtained from an analysis of the scanned cubes by CT. It is essential to remind that all the following considerations are approximations that provide only an idea of the behaviour of the cubes and not exact values.
Firstly, the apparent porosity (π_a) has been calculated in the same way of the tablets:

$$\pi_a = \frac{V_{designed}}{V_{tot}} \tag{4.5}$$

where $V_{designed}$ is the volume of the designed porosity (the cells) and V_{tot} is the total volume (volume of the material, the designed and the random porosity) that has been measured with VG studio software. $V_{designed}$ has been calculated by averaging the area of the cells and the sides of the cubes, thus it does not represent an exact value. The initial designed porosity (from the stl file) is 57.6%.
The total and closed porosity have been determined with the same formula of equation 4.4 and the overall porosity is reported in fig. 4.32.

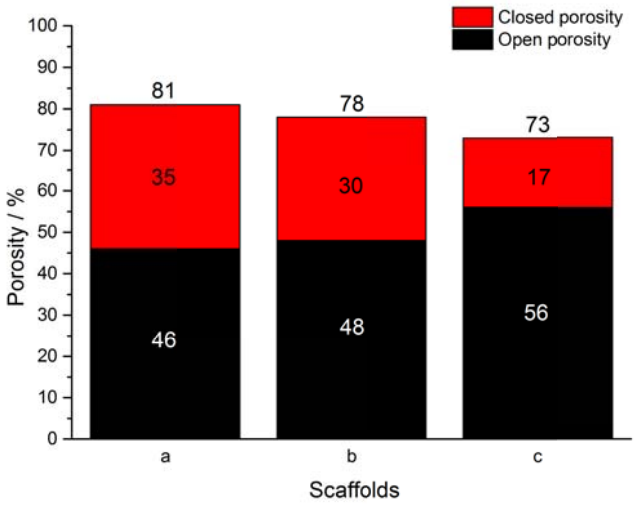

Figure 4.32: Total porosity of the α-TCP cubes: coarse powder cube printed without gas flow (*a*), coarse powder cube printed with gas flow (*b*), fine powder cube printed with gas flow (*c*).

First of all, it is interesting to see that the total porosity decreases with small particles size and with the use of the gas-flow even though this difference is not so significant. On the other hand, when looking at the closed and open porosity (extremely important from a biological point of view) the cube printed with the fine powder shows the highest amount of open pores and thus the lowest quantity of closed pores. While the coarse cubes have a similar open porosity and lower than the nominal one, the fine cube has a value almost equal to the original: fine powder can be printed with a better resolution that well

matches the stl file. Moreover, a isotropic shrinkage of the fine cubes (similarly to the fine tablets) reduces potential distortions. The struts of the coarse cubes have a thickness around 1 and 1.16 mm hence, on average, the cells are smaller than the original and since the volume decreases after sintering due to the densification, the apparent porosity reduces. By contrast, the struts of the fine cube has a dimension around 0.9 mm, thus the final designed porosity is near the nominal.
In conclusion, the fine cube has an higher apparent porosity and almost half of the closed porosity of the coarse cubes. This can have positive effects when implanted in vivo due to a promoted osseointegration and tissue ingrowth. With the method used to verify the porosity, the cubes printed with the coarse powder do not show substantial variations so with these results the gas flow seems to not strongly contribute.

4.5.2 Compressive test

The compressive test of the scaffolds shows an opposite trend compared to the B3B test of the tablets as depicted in fig. 4.33. The scaffolds printed with gas flow have higher strength than those printed without gas flow and in particular, the fine scaffolds have the highest value (3.4 MPa). These results can be explained by considering the density of the struts and the scaffold itself: the denser the scaffolds, the higher the compressive strength. As explained in the next sections, the microstructure of fine scaffolds is similar to that one of the fine tablets: indeed, cracks are visible especially near the connection between struts. However, differently to the B3B test, in the compressive test, there are no tensile stresses that promote the elongation of the cracks.

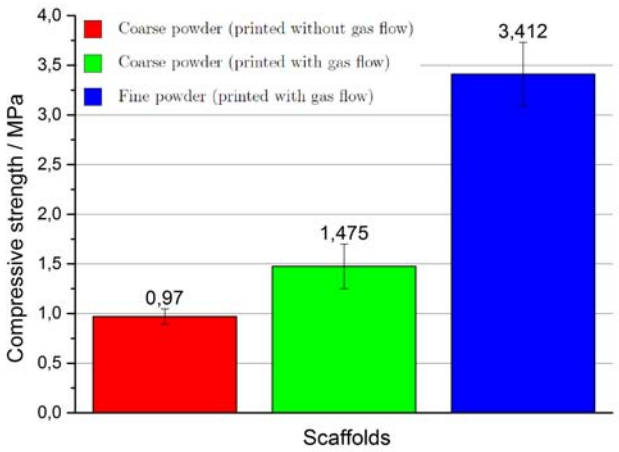

Figure 4.33: Compressive test of the α-TCP printed cubes. The values reported are in the form *mean value* $\pm$ *standard error*.

As already mentioned, the main drawback of α-TCP parts is the low mechanical strength mainly due to a poor sinter activity (loss of viscous flow) and for instance, its lower density than β-TCP and HA.
In the literature, 3D printed parts of CaPs can be found with a compressive strength around 15-20 MPa [42]. Since a scaffold should retain sufficient mechanical properties to fulfil the requirements of structural integrity once implanted in the host tissue, for bone repair applications, the scaffold should have similar mechanical features to the bone. It is well known that the density and therefore the strength of the bone varies locally. In the cortical bone the Young's modulus is between 1 and 20 GPa with a strength range between 1-100 MPa whereas in the cancellous part the modulus is 0.1-1.0 GPa and strength between 1 and 10 MPa [72].
Fig. 4.34 reports the data of the scaffolds of HA and β-TCP found in literature [73]. The graph plots the compressive strength versus the total porosity of the scaffolds and their bulk density and the apparent dry density of the bone. Moreover, the trend of the strength of the bone is outlined (estimated using a powder-law empirical model due to Keller [74]). In the graph, different manufacturing methods and geometries have been adopted to produce the scaffolds.
To have an idea about the results achieved with the printed α-TCP cubes, the three coloured circles have been added in the graph. Firstly, it is interesting to note a positive trend of the three typologies: printing with gas flow improves the properties of the scaffolds and the cubes printed with fine particles show features more similar to the cortical bone. The fine scaffolds have characteristics included in the 'cloud' of results that can be found in the literature. However, it is important to note that the axes are logarithmic: indeed the strength values belong to a range from 1 to 100 MPa, thus these scaffolds have completely different mechanical behaviour.
Considering the lower density of α-TCP compared to β and HA, the results of this work are positive: articles of pure α-TCP scaffolds are rare since grand part of the works deal with HA and HA/β-TCP as it can be seen from the greater number of white circles in the graph. Moreover, these considerations do not take into account the bioactivity of the material: in this case, α-TCP would have a better biological response than HA that is almost not degradable. However, to start talking about promising application for bone repair, the strength should be higher and this may be achieved reducing the porosity (and in this way, the porosity will better match that one of the cortical bone) and optimizing the printing and sintering parameters.
As it can be understood so far, the right combination of mechanical properties and biological response is extremely difficult to achieve and it still requires a lot of effort from the scientific community to have significant improvements for realistic applications.

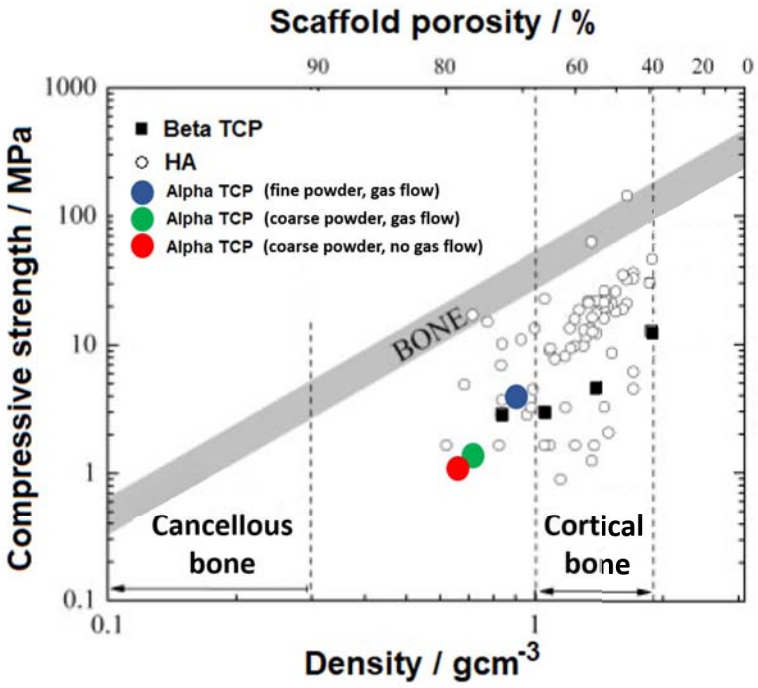

Figure 4.34: Comparative plot of the strength of HA (*black squares*) and β-TCP (*white circles*) scaffolds (from the literature) and the α-TCP scaffolds of this work *(coloured circles)*. Material density on the bottom x axis, scaffolds total porosity on the top x axis and compressive strength on the y axis.

4.5.3 OM and SEM microscopy

The images of the morphology the scaffolds (fig. 4.35) show similar characteristics to the tablets. The material is randomly distributed and the printing with gas flow makes the part denser and with fine powder the effect is higher. In other words, the overall porosity decreases while the closed pores seem to be greater in the fine scaffolds.

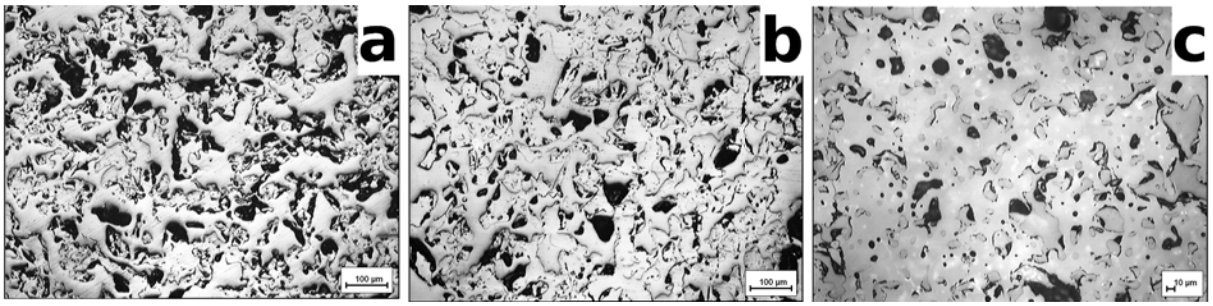

Figure 4.35: OM images of the α-TCP cubes: coarse powder cube printed without gas flow (a), coarse powder cube printed with gas flow (b), fine powder cube printed with gas flow (c).

The outcomes of the gas flow can be better appreciated in fig. 4.36 where the images reveal the areas close to the intersection of the struts. Generally, it is important to

note that the gas flow allows to have a more accurate definition of the printed part: images *a* and *b* confirmed this fact. The strut in the image *a* has a lower and irregular thickness that can be responsible for a lower mechanical strength if these defects occurs frequently. On the other hand, the strut in the image *b* has a well-defined shape ensuring a uniform load distribution. Alike the fine tablets, the fine scaffolds have several cracks. As image *c* illustrates, the cracks cut completely the cross section of the strut close to the intersection. This may due to the formation of stresses during the sintering. Therefore, the integrity of these scaffolds is already compromised just after the sintering but nonetheless their compressive strength is the highest probably due to the greater density. Indeed, most of the cracks (those normal to the application of the compressive force) close during the test thus they are not as dangerous as in the B3B test.

Figure 4.36: OM images of the α-TCP cubes (area near the inter-connection of the struts): coarse powder cube printed without gas flow (*a*), coarse powder cube printed with gas flow (*b*), fine powder cube printed with gas flow (*c*).

The SEM images clearly represent the morphology of the scaffolds. Fig. 4.37 show the cells of the three typologies of cubes. For the coarse cubes, the vertical axis of the image matches the printing orientation (z axis). Also from these pictures, the better definition of the fine powder can be noted: the square of the cell is well defined and the excessive powder along the sides is very low. Instead, in the cubes printed with coarse powder the sides are more irregular due to the presence of some powder attached. The presence of this excessive powder may due to the accuracy of the printing method but also to an inaccurate depowdering. Moreover, the cubes that have been printed with gas flow look more compacted and the fine cube has a regular texture on the surface because of the printing parameters. Fig. 4.38 well depicts this feature. With regards to the coarse powder, the cube printed with gas flow seems denser since the particles are more joint together. The gas flow results in a higher green density and therefore it promotes a higher sinter activity indeed the particles in the images *b* and *e* seem to have a more pronounced necking. The saturation of the coarse powder is the same (140%): however, the effect is greater in the sample with gas flow due to the higher density (*c* and *f*). No marks from the printing orientation are visible thus the printing parameter can be

considered suitable even though a higher saturation in the sample printed without gas flow may have ensured a better compaction.
On the other hand, when looking at the image c and f a regular texture is evident: this may due to a too low saturation or a too long drying time. Indeed, the layers are not perfectly bonded together. The printing orientation seems to be along the horizontal axis of the image since the vertical layers that can be noted on the surface better match the layer thickness (105 μm). Furthermore, the vertical sides of the cells are much more defined than the horizontal ones: this is the result of the roller deposition. Indeed, the vertical profiles in the picture (x axis) are determined by the roller that ensures a constant and precise layer thickness while in the horizontal sides the *staircase effect* is visible. This has been discussed in section 2.3: since a printed part is made layer upon layer, its profile is not completely smooth but the pile-up of the cross sections can be noted. Moreover, the horizontal lines are too far to each other (around 200 μm) to be considered the layers thickness. This may due to the formation of preferential air channels in the powder bed but it does not explain the constant appearance.

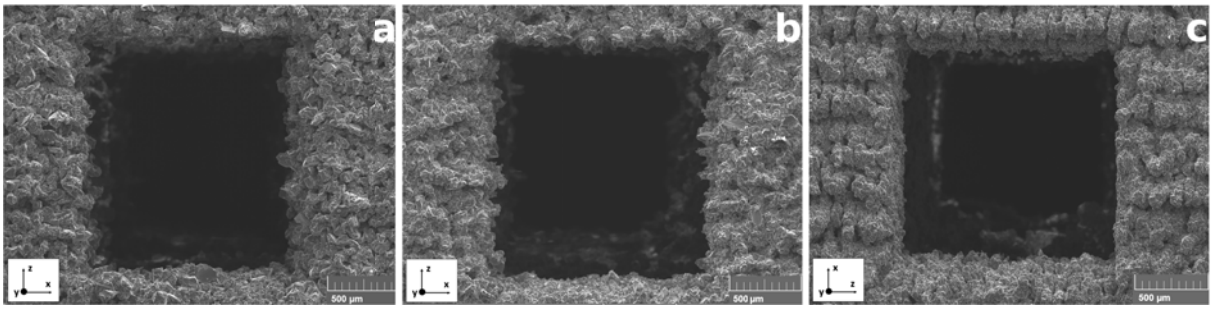

Figure 4.37: SEM images of the cells of the α-TCP cubes: coarse powder cube printed without gas flow (a), coarse powder cube printed with gas flow (b), fine powder cube printed with gas flow (c).

A deeper consideration deals with the printing parameters: generally, this process is meant to print powder bigger than $\sim$50 μm. In this case, the powder size starts to be comparable to the maximum resolution of the process. The pixel resolution is around 20-25 μm in the x and y axis therefore the voxel size is around 50 mm^3 (22 x 22 x 105 μm). From fig. 4.38c the distance between each 'ridge' of the horizontal line is $\sim$500 μm. This corresponds to the distance between the nozzles of the print-head (see fig. 4.39). For each layer, several passes of the print-head are necessary to jet the binder throughout the cross-section homogeneously. However, due to the small particle size, the first passes affect the join of the particles more strongly: when the binder is jetted, the powder that has been wetted by the droplets starts to move by diffusion (the dark arrows show this movement). The powder around the lines of binder just jetted (distant 500 μm) is more attracted and therefore the particles move towards these lines. As a result, the texture

of the SEM image can be explained (dashed red line). During the following passes, for instance when the print-head is jetting binder in between the first lines, the powder has already diffused and maybe partially dried so the effect is less marked. For the coarse powder instead, diffusion phenomena are less likely due to the bigger particle size.

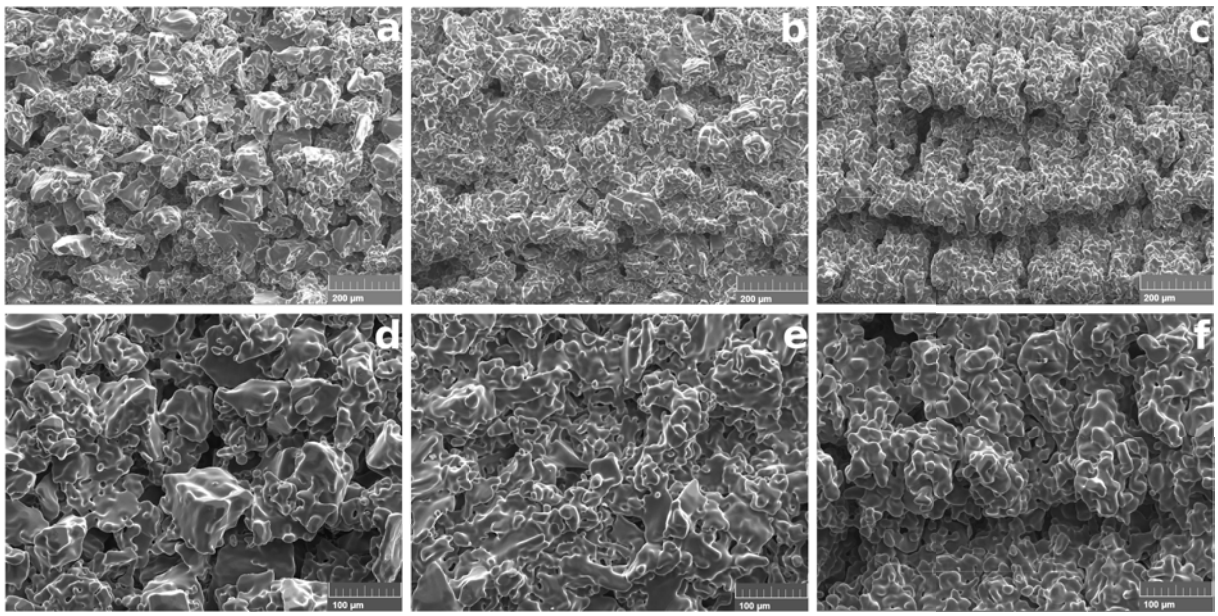

Figure 4.38: Higher magnification of the SEM images in fig. 4.37: coarse powder cube printed without gas flow (*a, d*), coarse powder cube printed with gas flow (*b, e*), fine powder cube printed with gas flow (*c, f*).

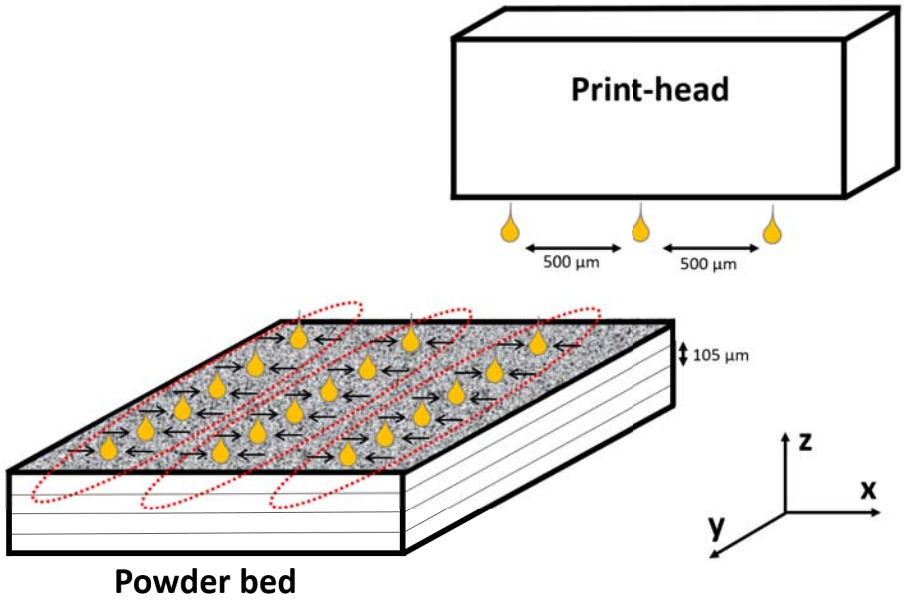

Figure 4.39: Possible explanation of the texture of the fine α-TCP cube. The drawing shows the first pass of the print-head: droplets are jetted in line (along the y axis). The black arrows represent the diffusion of the powder and the red dashed lines represent the final texture visible in the SEM images.

4.5.4 μCT analysis

μCT analyses have been carried out also on the cubes (after the first sintering program, *a*). Fig. 4.40 shows the cross sections of the three typologies of scaffolds: *a, b, c* refer to the cube printed with the coarse particles and without gas flow, *d, e, f* to the coarse powder cube printed with gas flow and *g, h, i* to the fine powder cube printed with gas flow.
Firstly, comparing the coarse cubes, no big differences can be noted; however, the cube printed with gas flow has smaller and more squared cells. Nevertheless, the cube printed without gas flow seem to have more squared struts (image *c*) than that one with gas (image *f*) that are more rounded. Lastly, the cube printed with the fine powder better preserves the original porosity and all its profiles appear rather linear and straight. The cross section *i* shows dense and fairly regular struts. Overall, the greater shrinkage of the fine cubes can be appreciated also in these images.
In fig. 4.41, the comparisons STL file-printed cubes are depicted. It is important to point out that in order to evaluate the accuracy of the printing process without considering the shrinkage of the cubes the STL files have been scaled down by a factor depending of the intensity of the volume reduction. Indeed, for each cube, three sides of the scanned scaffolds have been measured by VG studio to get each scale factors (l_i) . The values are reported as follows:

- coarse powder cube printed without gas flow: $l_1 = 0.82$, $l_2 = 0.79$, $l_3 = 0.80$;
- coarse powder cube printed with gas flow: $l_1 = 0.91$, $l_2 = 0.93$, $l_3 = 0.94$;
- fine powder cube printed with gas flow: $l_1 = 0.92$, $l_2 = 0.92$, $l_3 = 0.92$;

It is interesting to notice that the fine cube shows a isotropic shrinkage like the fine tablets. Overall, most of the area of the cubes are green indicating no geometrical variation. Yellow and red shades are more visible in the coarse cubes, especially in that one printed with gas flow. This may be caused by a non-accurate depowdering. A partial idea of the morphology of the cubes can also be outlined: image *a* has a rougher surface while in *c* the texture that has been discussed in the previous section can be observed. As already mentioned, the fine cube has a better definition of the struts, cells and sides.

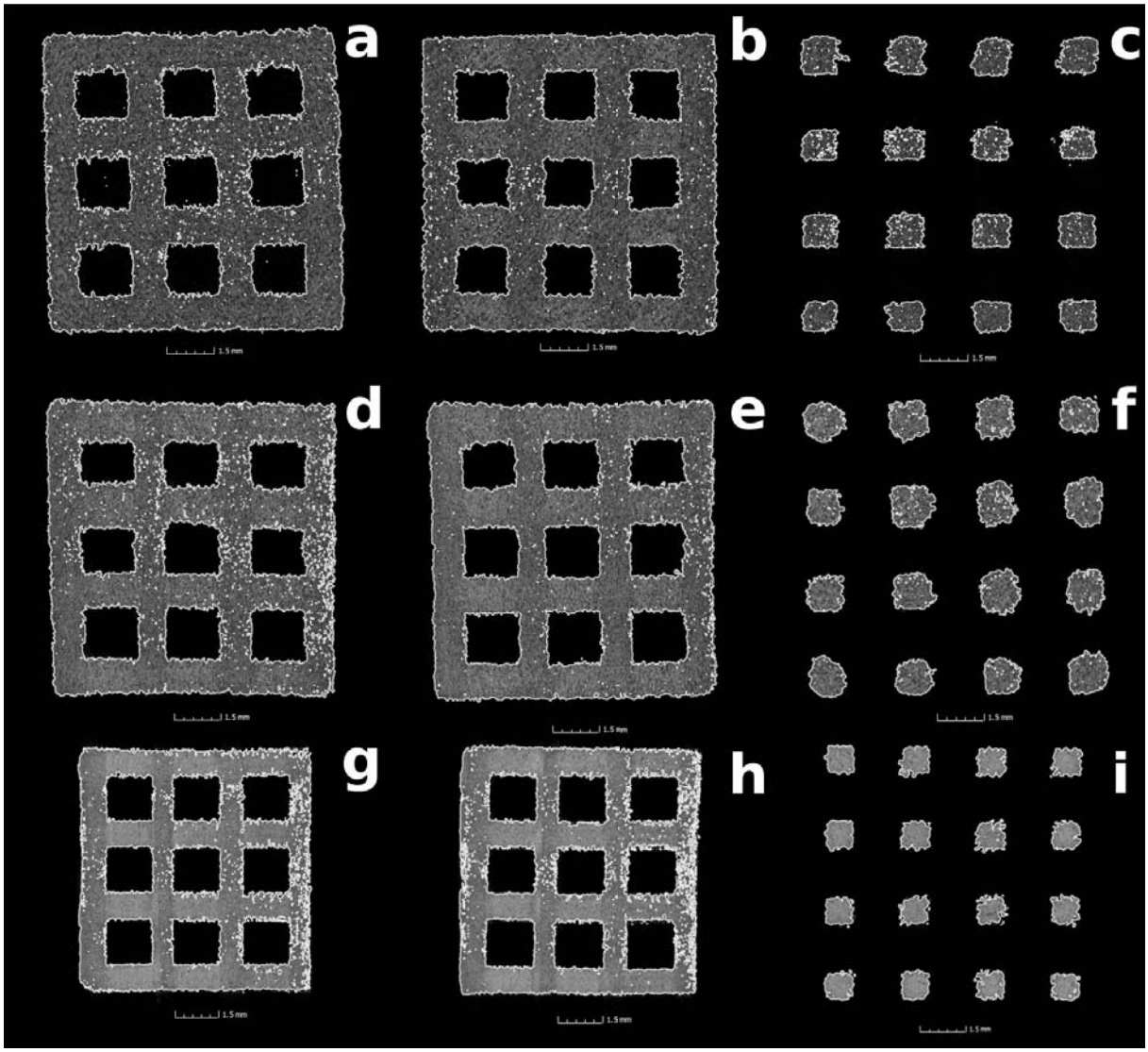

Figure 4.40: μCT of the α-TCP scaffolds. Sections of the coarse powder printed without (*a, b, c*) and with (*d ,e , f*) gas flow, fine powder printed with gas flow (*g, h, i*).

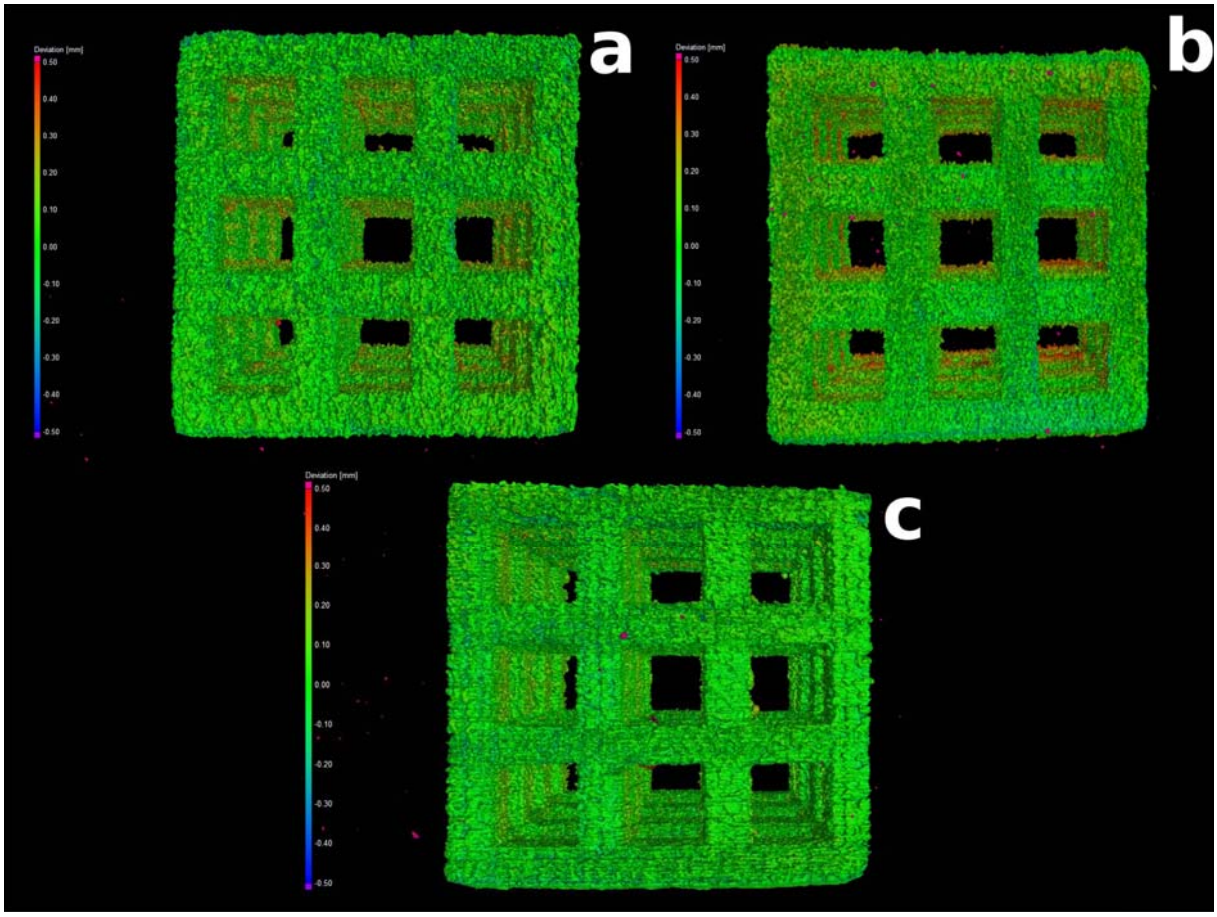

Figure 4.41: μCT of the α-TCP scaffolds: nominal/actual comparison after scaling of the STL file. Coarse powder printed without (a) and with (b) gas flow, fine powder printed with gas flow (c). Not in scale

Chapter 5

Conclusions

In this section, all the main conclusions are included.
The topic of this thesis is to study the synthesis of α-TCP, $Ca_3(PO_4)_2$, the 3D printing of tablets and scaffolds and their sintering behaviour.
Among calcium phosphates, tricalcium phosphate has promising applications in the biomedical field especially in orthopedics, dentistry and maxillofacial surgery thanks to its bioactivity and osteoconductive features. However, due to its poor mechanical properties, it has not been used for major load-bearing practices. Currently, α-TCP is used as powder for bone replacement and substitute for augmentation of bony defects since it has shown non-toxic, antigenically inactive and non-carcinogenic response. Its positive biological activity lies in several facts: chemical composition, structure and superficial charge. Firstly, since TCP belongs to the wider class of calcium phosphates (CaPs), it has a chemical composition similar to the human bone, indeed around 70% of it consists of CaPs. More specifically, TCP has a chemical formula close to hydroxyapatite ($Ca_{10}(PO_4)_6OH_2$) that is the major component of the bone. Moreover, TCP is employed to repair bone defects due to its bioresorbability that matches the growth of the new bone. α-TCP is considered to be more degradable than β-TCP and HA which is almost non resorbable. The reason seems to be the lower density of α-TCP compared to β-TCP since a weaker lattice structure promotes a faster degradation. Lastly, α-TCP contributes to a greater cells adhesion that may be caused by a more negative charged surface.
The α-TCP powder has been obtained from H_3PO_4 and $CaCO_3$ by solid state reaction. On average, the 7 batches produced contain 93$\pm$2% of α-TCP and 7$\pm$2% of HA. High purity of the powder is extremely important from a biological point of view since other compounds may cause an inflammatory response or have a slower degradation rate. Considering the standard of the biomedical grade of β-TCP as a reference (since there is no the equivalent for α-TCP), the purity required is 95%. This value is close to that one achieved, but considering the final part (printed and sintered) the XRD results confirm pure α-TCP; thus, perfectly suitable for biomedical applications. Anyway, this synthesis

route is appropriate to produce pure tricalcium phosphate as the batch number 7 shows (by avoiding any experimental mistake). Moreover, as different steps are involved in the treatment, the degree of purity of the end-product can be easily tailored according to the specific needs.
Furthermore, elemental analyses prove the low level of impurities. This is also justified by the DTA measurements: the α to β-TCP transformation does not occur both over heating and cooling neither at 1 °C/min. In literature, for rates lower than 10 °C/min, this phase transformation may happen.

To 3D print tablets and scaffolds, two particle sizes have been chosen: *fine* (lower than 25 μm) and *coarse* (between 45 and 100 μm). Binder jetting (commonly called 3D printing) is a proper method to achieve porous ceramic parts especially for biomedical applications. Generally, powder bigger than around 50 μm can be printed with this method. The reason is that the powder must be flowable in order to be uniformly deposited on the bed. The bigger the particles, the more homogeneous the spread. On the other hand, to have a higher definition and density of the printed part (and therefore greater mechanical properties, that are the main drawback for α-TCP), smaller particles are preferred. Indeed, the main outcome is that fine particles cannot be deposited uniformly and therefore 3D printed. An interesting method to solve this problem is by stabilizing the powder bed through a gas-flow (patented by BAM, Berlin, 2017). A vacuum pump is used to suck air from the bottom of the build bed: in this way the powder bed is more compacted and the effects of the interparticles forces decrease. Thus, even fine particles can be printed and the surface finish is even better than the coarse powder. In conclusion, three typologies have been adopted to print tablets and scaffolds: coarse powder with and without gas flow and fine powder with gas flow. Moreover, another advantage of the use of the gas flow during printing is that support structures may be avoided reducing the processing time and material wasted.

The effects of the stabilization through the gas flow can be appreciated from the density measurements of the tablets by the Archimedes' method. Fine tablets have the highest density: their bulk density is 2347 kg/m^3 while for the coarse tablets is 1603 kg/m^3 and 1392 kg/m^3 printed with and without gas respectively. In other words, the apparent porosity is around 15, 43 and 50% for the fine tablets, coarse tablets printed with and without gas flow respectively.
A careful reader may point out that for biomedical application a higher porosity is favored: the advantage of this method and the use of fine powder is that the random porosity can be minimized and the designed porosity can be tailored with a higher degree of freedom since the main challenge is to achieve dense parts and not vice versa.
To evaluate the mechanical properties, the ball on three balls test has been carried out: unexpectedly, the denser the tablets, the lower the strength. Coarse tablets printed

without gas flow have a value of 5.3 MPa while without gas flow 3.3 MPa. Fine tablets reach only 2.1 MPa. The more likely reason comes from the micrographs: the denser the tablets, the higher the amount of cracks in the sample. This may due to the phase transformation between α and α' (and vice versa) at around 1460 °C as the DTA measurements show. α-TCP is monoclinic (D_{th}: 2.866 g/cm^3) while α'-TCP is hexagonal (D_{th}: 2.702 g/cm^3). This structure modification results in the formation of stresses that are hardly relaxed in dense tablets.
Other sintering programs have been tried to reduce the formation of cracks in the tablets printed with gas-flow. The strength slightly increases but it is still lower than the coarse tablets that have been printed without gas flow. The coarse tablets reach a value of 3.4 MPa while the best result of the fine ones is 3.1 MPa. These two values are closer to each other than the first test but it must be considered than thanks to the smaller particles size, the densification rate during sintering is faster. Indeed, the fine tablets have been sintered for 2 hours at 1600 °C compared to 5 hours for the coarse ones.

The density and the microstructure of the scaffolds follow the same trend of the tablets. Those printed with gas flow and with fine particles have the highest bulk density (and therefore the lowest porosity). The coarse scaffolds have a density of 540 kg/m^3 (printed without gas flow) and 617 kg/m^3 (printed with gas flow). Instead, the fine scaffolds have a value of 765 kg/m^3. Moreover, it is interesting to note that the fine scaffolds have a porosity similar to the original file (57.6% from the STL file): the open porosity is around 56% while the close one is about 17%, almost half value than the coarse scaffolds. This may have significant effects on the nutrients transport during the integration of the scaffolds in the host tissue.
When looking at the behaviour under compression, the fine scaffolds show the best performance: their strength is 3.4 MPa compared to 1.4 and 0.9 MPa for the coarse cubes printed with and without gas flow respectively. This trend can be explained considering the density of the scaffolds: the denser, the stronger. However, from the OM and SEM images, cracks are visible with the same relationship of the tablets. In the fine scaffolds the amount is higher and the cracks are located especially close to the connection between the struts due to a higher concentration of stresses during the sintering. Nonetheless, this seems to not affect remarkably the mechanical properties. Indeed, differently to the B3B test, part of the cracks are closed during the compression thus the main parameter is the density of the part. In the B3B test, the tensile component of the stress state causes the elongation of the cracks and as a result, the tablet breaks easily.
From the μCT analysis, the fine scaffolds have a better definition of the struts, cells and sides. Moreover, their isotropic shrinkage allows to better maintain the original shape and porosity. Lastly, the surface of the fine scaffolds is smoother but with a regular texture due to the printing parameters: this is a combinate effect between print-head resolution,

small particles size and saturation.

In conclusion, the stabilization of the powder bed through a gas-flow is essential for powder smaller than 50 μm. Moreover, the density of the printed parts strongly rises. However, with the material used in this thesis, the higher density seems to cause a greater formation of cracks in the samples that, in some cases, strongly affect the mechanical properties. This may due to the phase transformation between α and α' therefore a deeper study of the sintering behaviour is necessary to avoid this problem. Due to the low sinter activity of pure TCP, high temperatures are mandatory and the phase transformation appear hard to avoid. The addition of other elements in the powder could retard the transformation as long as the bioactivity is preserved.

A last comment deals with the vacuum pressure of the powder bed: a further development may involve the measurement and control of the gas flow. How the pressure influences the density of the bed and how much the pressure changes along the z-axis may be interesting points to solve. Depending on the size, more parts can be printed at the same time one upon each other. In this case, the pressure must be equal along the z-axis to ensure that all the parts printed in one batch have the same properties.

Bibliography

[1] C. L. Ventola, "Medical applications for 3D printing: current and projected uses," *Pharmacy and Therapeutics*, vol. 39, no. 10, pp. 704–711, 2014.

[2] B. Berman, "3-D printing: The new industrial revolution," *Business horizons*, vol. 55, no. 2, pp. 155–162, 2012.

[3] K. Leuven *et al.*, "Additive manufacturing of ceramics: a review," *Journal of Ceramic Science and Technology*, vol. 5, no. 4, pp. 245–260, 2014.

[4] R. Trombetta, J. A. Inzana, E. M. Schwarz, S. L. Kates, and H. A. Awad, "3D printing of calcium phosphate ceramics for bone tissue engineering and drug delivery," *Annals of biomedical engineering*, vol. 45, no. 1, pp. 23–44, 2017.

[5] The Economist, "How a new manufacturing technology will change the world," no. 10, p. 7, 2011.

[6] J. A. Slotwinski, "Additive manufacturing: Overview and NDE challenges," vol. 1581, no. 1, pp. 1173–1177, 2014.

[7] C. Schubert, M. C. Van Langeveld, and L. A. Donoso, "Innovations in 3D printing: a 3D overview from optics to organs," *British Journal of Ophthalmology*, vol. 98, no. 2, pp. 159–161, 2014.

[8] I. Gibson and A. Srinath, "Simplifying medical additive manufacturing: Making the surgeon the designer," *Procedia Technology*, vol. 20, pp. 237–242, 2015.

[9] B. C. Gross, J. L. Erkal, S. Y. Lockwood, C. Chen, and D. M. Spence, "Evaluation of 3D printing and its potential impact on biotechnology and the chemical sciences," *Analytical Chemistry*, vol. 86, pp. 3240–3253, 2014.

[10] X. Cui, T. Boland, D. D'Lima, and M. K. Lotz, "Thermal inkjet printing in tissue engineering and regenerative medicine," *Recent patents on drug delivery & formulation*, vol. 6, no. 2, pp. 149–155, 2012.

[11] M. B. Hoy, "3D printing: making things at the library," *Medical reference services quarterly*, vol. 32, no. 1, pp. 93–99, 2013.

[12] "3D printing in pharmaceutics: A new tool for designing customized drug delivery systems," *International Journal of Pharmaceutics*, vol. 499, no. 1, pp. 376 – 394, 2016.

[13] G. T. Klein, Y. Lu, and M. Y. Wang, "3D printing and neurosurgery, ready for prime time?," *World neurosurgery*, vol. 80, no. 3, pp. 233–235, 2013.

[14] J. Banks, "Adding value in additive manufacturing: researchers in the United Kingdom and Europe look to 3D printing for customization," *IEEE pulse*, vol. 4, no. 6, pp. 22–26, 2013.

[15] I. T. Ozbolat and Y. Yu, "Bioprinting toward organ fabrication: Challenges and future trends," *IEEE Transactions on Biomedical Engineering*, vol. 60, no. 3, pp. 691–699, 2013.

[16] B. D. Ratner, A. S. Hoffman, F. J. Schoen, and J. E. Lemons, "Biomaterials science: an introduction to materials in medicine," pp. 1–7, 2004.

[17] L. L. Hench, "Bioceramics: from concept to clinic," *Journal of the american ceramic society*, vol. 74, no. 7, pp. 1487–1510, 1991.

[18] L. L. Hench, R. J. Splinter, W. Allen, and T. Greenlee, "Bonding mechanisms at the interface of ceramic prosthetic materials," *Journal of Biomedical Materials Research Part A*, vol. 5, no. 6, pp. 117–141, 1971.

[19] R. Langer and J. Vacanti, "Tissue engineering," *Tissue engineering: the union of biology and engineering*, vol. 98, pp. 920–926, 1993.

[20] B. Stevens, Y. Yang, A. Mohandas, B. Stucker, and K. T. Nguyen, "A review of materials, fabrication methods, and strategies used to enhance bone regeneration in engineered bone tissues," *Journal of biomedical materials research Part B: applied biomaterials*, vol. 85, no. 2, pp. 573–582, 2008.

[21] R. Z. Le Geros, "Properties of osteoconductive biomaterials: calcium phosphates," *Clinical orthopaedics and related research*, vol. 395, pp. 81–98, 2002.

[22] M. I. Mohammed, P. S. Badwal, and I. Gibson, "Design and fabrication considerations for three dimensional scaffold structures," *KnE Engineering*, vol. 2, no. 2, pp. 120–126, 2017.

[23] L. C. Gerhardt, K. L. Widdows, M. M. Erol, C. W. Burch, J. A. Sanz-Herrera, I. Ochoa, R. Stämpfli, I. S. Roqan, S. Gabe, and T. Ansari, "The pro-angiogenic properties of multi-functional bioactive glass composite scaffolds," *Biomaterials*, vol. 32, no. 17, pp. 4096–4108, 2011.

[24] F. Baino, G. Novajra, and C. Vitale-Brovarone, "Bioceramics and scaffolds: a winning combination for tissue engineering," *Frontiers in bioengineering and biotechnology*, vol. 3, 2015.

[25] P. De Aza, M. Rodríguez, S. Gehrke, J. Maté-Sánchez de Val, and J. Calvo-Guirado, "A Si-α-TCP scaffold for biomedical applications: an experimental study using the rabbit tibia model," *Applied Sciences*, vol. 7, no. 7, p. 706, 2017.

[26] W. Habraken, P. Habibovic, M. Epple, and M. Bohner, "Calcium phosphates in biomedical applications: materials for the future?," *Materials Today*, vol. 19, no. 2, pp. 69–87, 2016.

[27] K. Groot, "Effect of porosity and physicochemical properties on the stability, resorption, and strength of calcium phosphate ceramics," *Annals of the New York Academy of Sciences*, vol. 523, no. 1, pp. 227–233, 1988.

[28] J. C. Elliot, "Structure and chemistry of the apatites and other calcium orthophosphates," *Studies in Inorganic Chemistry*, vol. 18, pp. 1–50, 1994.

[29] R. Carrodeguas, A. Carrodeguas, S. X. De Aza, and P. P. Turillax, "New approach to the $\beta\rightarrow$ α polymorphic transformation in magnesium-substituted tricalcium phosphate and its practical implications," *Journal of the American Ceramic Society*, vol. 91, no. 4, pp. 1281–1286, 2008.

[30] A. R. West, "Solid state chemistry and its applications," vol. 2, 1984.

[31] J. D. Pasteris, "A mineralogical view of apatitic biomaterials," *American Mineralogist*, vol. 101, no. 12, pp. 2594–2610, 2016.

[32] R. Carrodeguas and S. D. Aza, "α-Tricalcium phosphate: synthesis, properties and biomedical applications," *Acta biomaterialia*, vol. 7, no. 10, pp. 3536–3546, 2011.

[33] F. Barrère, C. A. van Blitterswijk, and K. De Groot, "Bone regeneration: molecular and cellular interactions with calcium phosphate ceramics," *International journal of nanomedicine*, vol. 1, no. 3, p. 317, 2006.

[34] M. Yamada, M. Shiota, Y. Yamashita, and S. Kasugai, "Histological and histomorphometrical comparative study of the degradation and osteoconductive

characteristics of α- and β-tricalcium phosphate in block grafts," *Journal of Biomedical Materials Research Part B: Applied Biomaterials*, vol. 82B, no. 1, 2007.

[35] J. Liu, L. Zhao, L. Ni, C. Qiao, D. Li, H. Sun, and Z. Zhang, "The effect of synthetic α-tricalcium phosphate on osteogenic differentiation of rat bone mesenchymal stem cells," *American journal of translational research*, vol. 7, no. 9, p. 1588, 2015.

[36] I. Martinez, P. Velásquez, L. Meseguer-Olmo, A. Bernabeu-Esclapez, and P. De Aza, "Preparation and characterization of novel bioactive α-tricalcium phosphate doped with dicalcium silicate ceramics," *Materials Science and Engineering: C*, vol. 32, no. 4, pp. 878–886, 2012.

[37] C. Seebach, J. Schultheiss, K. Wilhelm, J. Frank, and D. Henrich, "Comparison of six bone-graft substitutes regarding to cell seeding efficiency, metabolism and growth behaviour of human mesenchymal stem cells (MSC) in vitro," *Injury*, vol. 41, no. 7, pp. 731–738, 2010.

[38] A. Ehara, K. Ogata, S. Imazato, S. Ebisu, T. Nakano, and Y. Umakoshi, "Effects of α-TCP and TetCP on MC3T3-E1 proliferation, differentiation and mineralization," *Biomaterials*, vol. 24, no. 5, pp. 831 – 836, 2003.

[39] U. Mayr-Wohlfart, J. Fiedler, K.-P. Günther, W. Puhl, and S. Kessler, "Proliferation and differentiation rates of a human osteoblast-like cell line (SaOS-2) in contact with different bone substitute materials," *Journal of Biomedical Materials Research*, vol. 57, no. 1, 2001.

[40] K. Igawa, M. Mochizuki, O. Sugimori, K. Shimizu, K. Yamazawa, H. Kawaguchi, K. Nakamura, T. Takato, R. Nishimura, S. Suzuki, *et al.*, "Tailor-made tricalcium phosphate bone implant directly fabricated by a three-dimensional ink-jet printer," *Journal of Artificial Organs*, vol. 9, no. 4, pp. 234–240, 2006.

[41] J. Wiltfang, H. Merten, K. Schlegel, S. Schultze-Mosgau, F. Kloss, S. Rupprecht, and P. Kessler, "Degradation characteristics of α and β tri-calcium-phosphate (TCP) in minipigs," *Journal of Biomedical Materials Research Part A*, vol. 63, no. 2, pp. 115–121, 2002.

[42] A. Zocca, P. Colombo, C. M. Gomes, and J. Günster, "Additive manufacturing of ceramics: issues, potentialities, and opportunities," *Journal of the American Ceramic Society*, vol. 98, no. 7, pp. 1983–2001, 2015.

[43] N. Travitzky, A. Bonet, B. Dermeik, T. Fey, I. Filbert-Demut, L. Schlier, T. Schlordt, and P. Greil, "Additive manufacturing of ceramic-based materials," *Advanced Engineering Materials*, vol. 16, no. 6, pp. 729–754, 2014.

[44] L. Ferrage, G. Bertrand, P. Lenormand, D. Grossin, and B. Ben-Nissan, "A review of the additive manufacturing (3DP) of bioceramics: alumina, zirconia (PSZ) and hydroxyapatite," *Journal of the Australian Ceramic Society*, vol. 53, no. 1, pp. 11–20, 2017.

[45] M. J. S. A. M. Pietak, J. W. Reid and M. Sayer, "Silicon substitution in the calcium phosphate bioceramics," *Biomaterials*, vol. 28, no. 28, pp. 4023 – 4032, 2007.

[46] Y. Zhang, G. Yin, S. Zhu, D. Zhou, Y. Wang, Y. Li, and L. Luo, "Preparation of β-$Ca_3(PO_4)_2$ bioceramic powder from calcium carbonate and phosphoric acid," *Current Applied Physics*, vol. 5, no. 5, pp. 531–534, 2005.

[47] S. R. Kasim, Y. M. How, H. Seli, H. Md Akil, and A. Ahmad, "The effect of calcium carbonate particle size on the formations β-tricalcium phosphate," *Ceramic processing research*, vol. 10, no. 5, pp. 664–668, 2009.

[48] A. Zocca, C. M. Gomes, E. Bernardo, R. Müller, J. Günster, and P. Colombo, "LAS glass–ceramic scaffolds by three-dimensional printing," *Journal of the European Ceramic Society*, vol. 33, no. 9, pp. 1525–1533, 2013.

[49] M. Vaezi and C. K. Chua, "Effects of layer thickness and binder saturation level parameters on 3D printing process," *The International Journal of Advanced Manufacturing Technology*, vol. 53, no. 1, pp. 275–284, 2011.

[50] A. Zocca, C. M. Gomes, T. Mühler, and J. Günster, "Powder-bed stabilization for powder-based additive manufacturing," *Advances in Mechanical Engineering*, vol. 6, p. 491581, 2014.

[51] J. Günster, A. Zocca, C. Morais, and G. Thomas Mühler, "Method for stabilizing a powder bed by means of vacuum for additive manufacturing. US 9533452 B2," *Bundesanstalt für Materialforschung und -prüfung, BAM*, 2017.

[52] C. Carter and M. Norton, "Sintering and grain growth," *Ceramic Materials: Science and Engineering*, pp. 427–443, 2007.

[53] E. Champion, "Sintering of calcium phosphate bioceramics," *Acta Biomaterialia*, vol. 9, no. 4, pp. 5855 – 5875, 2013.

[54] A. Börger, P. Supancic, and R. Danzer, "The ball on three balls test for strength testing of brittle discs: stress distribution in the disc," *Journal of the European Ceramic Society*, vol. 22, no. 9, pp. 1425 – 1436, 2002.

[55] A. Börger, P. Supancic, and R. Danzer, "The ball on three balls test for strength testing of brittle discs: Part 2: analysis of possible errors in the strength determination," *Journal of the European Ceramic Society*, vol. 24, no. 10, pp. 2917 – 2928, 2004.

[56] W. Harrer, R. Danzer, P. Supancic, and T. Lube, "The ball on three balls test: Strength testing of specimens of different sizes and geometries," *10th International Conference of the European Ceramic Society*, pp. 1271–1275, 2008.

[57] H. Zielke, M. Abendroth, and M. Kuna, "Determining fracture mechanical properties for brittle materials using the ball on three balls test combined with numerical simulations," *Theoretical and Applied Fracture Mechanics*, vol. 86, pp. 19 – 24, 2016.

[58] I. Rehman and W. Bonfield, "Characterization of hydroxyapatite and carbonated apatite by photo acoustic FTIR spectroscopy," *Journal of Materials Science: Materials in Medicine*, vol. 8, no. 1, pp. 1–4, 1997.

[59] J. Kolmas, A. Kaflak, A. Zima, and A. Ślósarczyk, "Alpha-tricalcium phosphate synthesized by two different routes: Structural and spectroscopic characterization," *Ceramics International*, vol. 41, no. 4, pp. 5727 – 5733, 2015.

[60] M.-G. Ma, "Hierarchically nanostructured hydroxyapatite: hydrothermal synthesis, morphology control, growth mechanism, and biological activity," *International journal of nanomedicine*, vol. 7, p. 1781, 2012.

[61] C. L. Popa, M. Albu, C. Bartha, A. Costescu, C. Luculescu, R. Trusca, and S. Antohe, "Structural characterization and optical properties of hydroxyapatite/collagen matrix," *Romanian Reports in Physics*, vol. 68, 2016.

[62] S. Raynaud, E. Champion, D. Bernache-Assollant, and P. Thomas, "Calcium phosphate apatites with variable Ca/P atomic ratio 1. Synthesis, characterisation and thermal stability of powders," *Biomaterials*, vol. 23, no. 4, pp. 1065 – 1072, 2002.

[63] L. Berzina-Cimdina and N. Borodajenko, "Research of calcium phosphates using fourier transform infrared spectroscopy," *Infrared Spectroscopy - Materials Science, Engineering and Technology*, 04 2012.

[64] B. Mirhadi, B. Mehdikhani, and N. Askari, "Synthesis of nano-sized β-tricalcium phosphate via wet precipitation," *Processing and Application of Ceramics*, vol. 5, no. 4, pp. 193–198, 2011.

[65] P. Miranda, E. Saiz, K. Gryn, and A. P. Tomsia, "Sintering and robocasting of β-tricalcium phosphate scaffolds for orthopaedic applications," *Acta biomaterialia*, vol. 2, no. 4, pp. 457–466, 2006.

[66] L. C. De Jonghe and M. N. Rahaman, "Sintering of ceramics," *Handbook of Advanced Ceramics: Materials, Applications, Processing and Properties*, vol. 2, p. 187, 2003.

[67] K. Hing, S. Best, and W. Bonfield, "Characterization of porous hydroxyapatite," *Journal of Materials Science: Materials in Medicine*, vol. 10, no. 3, pp. 135–145, 1999.

[68] G. Muralithran and S. Ramesh, "The effects of sintering temperature on the properties of hydroxyapatite," *Ceramics International*, vol. 26, no. 2, pp. 221–230, 2000.

[69] Z. Li and K. A. Khor, "Transparent hydroxyapatite obtained through spark plasma sintering: optical and mechanical properties," vol. 631, pp. 51–56, 2015.

[70] Y. Yanaba and K. Hayashi, "Relation between fracture surface area of a flexural strength specimen and fracture toughness for WC-10 mass% Co cemented carbide and Si_3N_4 ceramics," *Materials Science and Engineering: A*, vol. 209, no. 1, pp. 169 – 174, 1996.

[71] J. Da S. Ramos, S. Fraga, G. Vogel, and L. May, "Influence of the geometry of ceramic specimens on biaxial flexural strength: experimental testing and finite element analysis," vol. 64, pp. 120–125, 2018.

[72] I. Sabree, J. Gough, and B. Derby, "Mechanical properties of porous ceramic scaffolds: influence of internal dimensions," *Ceramics International*, vol. 41, no. 7, pp. 8425–8432, 2015.

[73] P. Miranda, A. Pajares, E. Saiz, A. P. Tomsia, and F. Guiberteau, "Mechanical properties of calcium phosphate scaffolds fabricated by robocasting," *Journal of Biomedical Materials Research Part A*, vol. 85, no. 1, pp. 218–227, 2008.

[74] T. S. Keller, "Predicting the compressive mechanical behavior of bone," *Journal of biomechanics*, vol. 27, no. 9, pp. 1159–1168, 1994.